

GROWTH KINETICS AND PROCESSINGS
OF COPPER INDIUM DISELENIDE-BASED THIN FILMS

By

SUKU KIM

A DISSERTATION PRESENTED TO THE GRADUATE SCHOOL
OF THE UNIVERSITY OF FLORIDA IN PARTIAL FULFILLMENT
OF THE REQUIREMENTS FOR THE DEGREE OF
DOCTOR OF PHILOSOPHY

UNIVERSITY OF FLORIDA

2003

Copyright 2003

by

Suku Kim

To my Lord, my wife, and my family
for their unconditional love.

ACKNOWLEDGMENTS

I am very grateful that I had such a precious time during my Ph.D. study here in Gainesville. Along with the productive research experiences, I have been blessed with so many things that God has planned for me. When I look back upon my last years, I realize that everything eventually became better than the best that I could have wished for.

First and foremost, I would like to thank my family. My wife, Aggie, has always shown the most sincere love and support. She has been the source of my strength especially during my times of frustration. I am the luckiest man to have her next to me in my life.

I thank my parents Tae Hwa Kim and Young Soon Lee, for their devotion and tender love. They have always believed in me. I thank my grandma for her unconditional love towards me. My sweet sister and brother, I thank both for their love and support.

I extend my most sincere thanks to my adviser, Dr. Anderson, for his guidance and care. He always emphasized on being an independent researcher, and he leaded me in that way. I would like to express my appreciation to every member in my supervisory committee. They helped me in every possible way to find a right direction of my research. I send my special thank to Dr. Crisalle for his time and sincere help. He and I worked together on many projects, and he always tried to be there for me. Dr. Li and Dr. Holloway, their knowledge and sincere help were often the inspirations for my research. I had an opportunity to work for Dr. Ren, and it was one of the most productive and pleasant experiences.

I must acknowledge my colleagues for their kind help and valuable contributions. Seokhyun Yoon, Woo Kyoung Kim, Ryan Kaczynski, Ryan Acher, Lei Li, and Jiyon Song, they are wonderful people to work with. Especially, I thank Seokhyun and Woo Kyoung for their contribution to many of my works. I also thank former students, Dr. Serkan Kincal and Dr. Billy Stanberry for their tremendous help.

I acknowledge the National Renewable Energy Laboratory and the Oak Ridge National Laboratory for providing excellent research opportunities. I extend my special thanks to Dr. Andrew Payzant for his sincere help on high-temperature XRD study.

I would like to thank all the staffs of Microfabritech for their wonderful jobs on creating the best research environment.

I have been blessed with many friends that I met during my study. The people from Korean Baptist Church of Gainesville are not just friends but brothers and sisters to me. I express my special thanks to pastor Sohn and Mrs. Sohn for their love. I know that they never stopped praying for me and my wife.

And finally, all my thanks go to my Lord.

TABLE OF CONTENTS

	<u>page</u>
ACKNOWLEDGMENTS	iv
LIST OF TABLES.....	ix
LIST OF FIGURES.....	x
ABSTRACT.....	xv
1 INTRODUCTION	1
1.1 System Description	4
1.2 Statement of Problems.....	9
2 BACKGROUND AND LITERATURE REVIEW OF SOLAR CELL AND CuInSe ₂ -BASED MATERIALS	10
2.1 Solar Cell Fundamentals	10
2.2 Cu(In,Ga)Se ₂ -based Thin Film Solar Cells.....	14
2.3 Fundamentals of CuInSe ₂ -based Materials.....	17
2.3.1 Crystalline Structure and Solid State Electronics of CIS-based Materials..	17
2.3.2 Structure, Chemistry, and Processing of CIS-based Thin Films.....	20
2.3.2.1 Structure and chemistry of CIS-based thin films.....	20
2.3.2.2 Processing of CIS-based solar cells	22
2.4 Characterization Techniques for CIS-based Films	25
3 REACTION KINETICS AND PATHWAYS OF CuInSe ₂ GROWTH FROM BILAYER PRECURSOR FILMS: TIME-RESOLVED HIGH TEMPERATURE X-RAY DIFFRACTION STUDY.....	28
3.1 Introduction.....	28
3.2 Experiments	29
3.2.1 Preparation of Precursor Films.....	29
3.2.2 Time-resolved High Temperature X-ray Diffraction.....	30
3.2.3 Calibration for Absolute Temperature of Samples	32
3.3 Results and Discussion	33
3.3.1 Reaction Kinetics of CuInSe ₂ Growth from InSe/CuSe Bilayer.....	33
3.3.2 Engineering of Reaction Pathways	39
3.4 Conclusions.....	40

4	SECONDARY GRAIN GROWTH OF CuInSe ₂ IN THE PRESENCE OF Cu _x Se DRIVEN BY INTERFACIAL FORCES.....	54
4.1	Introduction.....	54
4.2	Kinetic Aspect of Growth Mechanism of CuInSe ₂ -based Thin Films.....	55
4.2.1	Vapor-Liquid-Solid Growth Model for CIS-based Thin Films	55
4.2.2	Experimental Evidence of the Liquid Phase during Growth Process	59
4.3	Experiments	62
4.4	Results and Discussion	63
4.5	Conclusions.....	68
5	EPITAXIAL GROWTH OF CuInSe ₂ AND CuGaSe ₂ FILMS ON SINGLE CRYSTALLINE GaAs SUBSTRATE USING A MIGRATION ENHANCED EPITAXY REACTOR	84
5.1	Introduction.....	84
5.2	Experiments	85
5.3	Results and Discussion	87
5.4	Conclusions.....	91
6	THERMAL MODELING OF A ROTATING PLATEN AND SUBSTRATE IN A MIGRATION ENHANCED EPITAXY REACTOR	106
6.1	Introduction.....	106
6.2	Experiments	107
6.3	Modeling Equations and Strategy.....	109
6.4	Results and Discussion	112
6.5	Conclusions.....	114
7	FUTURE WORK.....	124
7.1	High Temperature X-ray Diffraction.....	124
7.1.1	Study of Reaction Kinetics of Binary Phases Formation.....	124
7.1.2	Reaction kinetics of Cu(In,Ga)Se ₂ Formation From Precursor Films	125
7.1.3	<i>In-situ</i> Investigation of Grain Growth and Epitaxy.....	126
7.2	Study of the Relationship between Electrical Properties and Surface Phase of CuIn(S, Se) ₂ Thin Films: Engineering of Bandgap and Surface Phase.....	128
7.2.1	Background	128
7.2.2	Electronic and Structural Properties of CuInS ₂ Thin Films	129
7.2.3	Bi-layer Structure for CuInS ₂ -based Absorber Layer.....	134
7.3	Continuous Deposition of Cd-free Buffer Layers without Breaking Vacuum....	136
7.3.1	Background	136
7.3.2	Alternative Buffer Layers	136
7.3.3	Growth Process and Properties of Indium Sulfide and Indium selenide ...	137
	LIST OF REFERENCES.....	140

BIOGRAPHICAL SKETCH	147
---------------------------	-----

LIST OF TABLES

<u>Table</u>	<u>page</u>
3.1 Thermocouple reading and corrected temperature of the specimen measured by the thermal expansion method.....	42
3.2 Estimated rate constants and Avrami exponents for CuInSe ₂ formation from bilayer precursor films.....	42
3.3 Estimated rate constants and the exponents based on the parabolic rate law for CuInSe ₂ formation from bilayer precursor films.....	42
4.1 Summary annealing conditions.....	69
4.2 Composition (ICP) and X-ray diffraction analysis results.....	70
5.1 Process conditions for CIS and CGS film growth.....	92
5.2 Compositional variation of samples CIS 350 and CGS 353	93

LIST OF FIGURES

<u>Figure</u>	<u>page</u>
1.1 Schematic top view of the plasma-assisted migration enhanced epitaxy (PMEE) system	6
1.2 Schematic structure of the platen and the control thermocouple. (a) Top view of the platen showing two of the 9 substrate-holders and the position of the heater, (b) Cross-sectional view showing the mounting of the heater above the platen, the position of a control thermocouple in the open gap, and the position of a glass substrate fitted in a holder that lies in an incision made in the platen.	7
2.1 Spectral distribution of sunlight. (Figure taken from Möller 1993).....	11
2.2 Band diagrams of an unbiased p-n junction solar cell: (a) in the dark and (b) under illumination.....	12
2.3 Schematic diagram of a p-n junction solar cell.....	12
2.4 Current-voltage characteristics of a p-n junction diode in the dark and when illuminated, defining the basic parameters.	14
2.5 Equivalent electrical circuit of a p-n junction for the two-diode model with diffusion I_S and recombination current I_{SR} , series R_S and shunt R_{Sh} resistance, and light-generated current I_L	14
2.6 Absorption coefficient as a function of the photon energy for selected semiconductor materials (Figure taken from Möller 1993).	15
2.7 Schematic structure for a CuInSe_2 thin film solar cell.....	16
2.8 Tetragonal unit cell of an ABX_2 chalcopyrite lattice: A = Cu, B = In, and X = Se for CuInSe_2 (Figure taken from Bube 1998)	18
2.9 Carrier concentration of p- and n-type CuInSe_2 single crystals as a function of the composition ratio, $[\text{Cu}]/[\text{In}]$. Black symbols are n-type and white symbols are p-type. (Figure taken from Möller 1993)	20
3.1 Structure of the precursor film, InSe/CuSe : (a) schematic drawing of the precursor film structures, (b) cross-sectional SEM image of the precursor film ($\times 40,000$)..	43

3.2	Time-resolved <i>in-situ</i> X-ray Diffraction for isothermal heating at 218 °C. The last 20 data were collected while heating at 340 °C for 30 minutes.	44
3.3	Fractional reaction of CuInSe ₂ formation during the isothermal runs as a function of time and temperature.....	45
3.4	Fractional reaction of CuSe transformation during the isothermal runs as a function of time and temperature.	46
3.5	Sum of the mole fractions of the reactant (CuSe) and the product (CuInSe ₂) through isothermal heating.	47
3.6	Avrami plots for the isothermal reactions at different temperatures.	48
3.7	Arrhenius plot for the isothermal reactions based on the Avrami analysis: apparent activation energy for CuInSe ₂ growth reaction, $E_a = 66.0$ kJ/mol.....	49
3.8	Plots based on the parabolic rate law for the isothermal reactions at different temperatures.....	50
3.9	Arrhenius plot for the isothermal reactions based on the parabolic rate law: apparent activation energy for CuInSe ₂ growth reaction, $E_a = 65.2$ kJ/mol.....	51
3.10	Time-resolved <i>in-situ</i> X-ray Diffraction with increasing temperature: transformation from a-InSe/CuSe to CuInSe ₂	52
3.11	Time-resolved <i>in-situ</i> X-ray Diffraction with increasing temperature: transformation from a-InSe/Cu:Se to CuInSe ₂	53
4.2	Schematic structure of a growing Cu-rich CIS thin film based on the vapor-liquid-solid model.....	71
4.3	SEM images of different regions on the surface showing an apparent difference in grain size in (a) matrix region and (b) droplet region.....	72
4.4	Droplet structures on an as-grown Cu-rich CuInSe ₂ film with annealing: T = 450 °C, [Cu]/[In] =1.03.	72
4.5	Schematics of sample structures: (a) without the CuSe layer, control sample, (b) with the CuSe layer.....	73
4.6	Cross-sectional SEM images of CuInSe ₂ films: (a) annealed without the copper selenide layer on the top of the CuInSe ₂ layer.....	74
4.6	Cross-sectional SEM images of the CuInSe ₂ films: (b) annealed with the copper selenide layer. Both samples were treated with KCN solution to selectively remove the copper selenide layer after annealing.....	75

4.7	Cross-sectional SEM images of CuInSe ₂ films: (a) annealed without the copper selenide layer on the top of the CuInSe ₂ layer.....	76
4.7	Cross-sectional SEM images of the CuInSe ₂ films: (b) annealed with the copper selenide layer. Both samples were treated with KCN solution to selectively remove the copper selenide layer after annealing.....	77
4.8	CIS (112) diffraction peaks: (a) annealed at approximately 450 °C without selenium overpressure. The sample 359-8K was not annealed. The sample 362-3K and 363-3K were annealed with the copper selenide layer, while sample 362-4K and 363-4K were annealed without the copper selenide layer. All the samples were treated by KCN to selectively remove the copper selenide after annealing.....	78
4.8	CIS (112) diffraction peaks: (b) same temperature condition, but with selenium overpressure. The sample 359-8K was not annealed. The sample 362-3K and 363-3K were annealed with the copper selenide layer, while sample 362-4K and 363-4K were annealed without the copper selenide layer. All the samples were treated by KCN to selectively remove the copper selenide after annealing.....	79
4.9	CIS (204)/(220) diffraction peaks: (a) annealed at approximately 450 °C without selenium overpressure. The sample 359-8K was not annealed. The sample 362-3K and 363-3K were annealed with the copper selenide layer, while sample 362-4K and 363-4K were annealed without the copper selenide layer. All the samples were treated by KCN to selectively remove the copper selenide after annealing.....	80
4.9	CIS (204)/(220) diffraction peaks: (b) same temperature condition, but with selenium overpressure. The sample 359-8K was not annealed. The sample 362-3K and 363-3K were annealed with the copper selenide layer, while sample 362-4K and 363-4K were annealed without the copper selenide layer. All the samples were treated by KCN to selectively remove the copper selenide after annealing.....	81
4.10	XRD peak areas: (a) annealed at approximately 450 °C without selenium overpressure. The sample 359-8K was not annealed. The sample 362-3K and 363-3K were annealed with the copper selenide layer, while sample 362-4K and 363-4K were annealed without the copper selenide layer. All the samples were treated by KCN to selectively remove the copper selenide after annealing	82
4.10	XRD peak areas: (b) same temperature condition, but with selenium overpressure. The sample 359-8K was not annealed. The sample 362-3K and 363-3K were annealed with the copper selenide layer, while sample 362-4K and 363-4K were annealed without the copper selenide layer. All the samples were treated by KCN to selectively remove the copper selenide after annealing.....	83

5.1	Multiple temperature growth schedule: nucleation at a lower T_{sub} , enhanced surface migration using a higher T_{sub} , subsequent growth at a lower T_{sub} to grow metastable phase with low dislocation density.....	94
5.2	SEM images of $CuInSe_2$ (CIS 350): atomic ratio, $[Cu]/[In] = 1.16$, (a) grown on (001) GaAs ($\times 3000$), (b) grown on Mo-coated soda lime glass ($\times 3000$).	95
5.3	SEM images of $CuInSe_2$ (CIS 350) grown on (001) GaAs: atomic ratio, $[Cu]/[In] = 1.16$, (a) dark background area of Figure 5.2 (a) ($\times 20000$), (b) bright island area of Figure 5.2 (a) ($\times 20000$).....	96
5.4	AFM images of $CuInSe_2$ (CIS 350) grown on (001) GaAs: atomic ratio, $[Cu]/[In] = 1.16$, (a) $10\mu \times 10\mu$, (b) $5\mu \times 5\mu$	97
5.5	SEM images of $CuGaSe_2$ (CGS 353): atomic ratio, $[Cu]/[In] = 1.29$, (a) grown on (001) GaAs ($\times 3000$), (b) grown on Mo-coated soda lime glass ($\times 3000$).	98
5.6	SEM images of $CuGaSe_2$ (CGS 353) grown on (001) GaAs: atomic ratio, $[Cu]/[In] = 1.29$, (a) plain view ($\times 20000$), (b) side view ($\times 20000$).	99
5.7	XRD θ -2 θ scan diffraction data of $CuInSe_2$ film (CIS 354) grown on (001) GaAs: atomic ratio, $[Cu]/[In] = 0.97$	100
5.8	XRD θ -2 θ scan diffraction data of $CuInSe_2$ film (CIS 350) grown on (001) GaAs: atomic ratio, $[Cu]/[In] = 1.15$	101
5.9	XRD θ -2 θ scan diffraction data of $CuGaSe_2$ film (CGS 353) grown on (001) GaAs: atomic ratio, $[Cu]/[In] = 1.29$	102
5.10	XRD θ -2 θ scan diffraction data of $CuGaSe_2$ film (CGS 355) grown on (001) GaAs: atomic ratio, $[Cu]/[In] = 1.09$	103
5.11	SEM images of $CuInSe_2$ (CIS 350) grown on (001) GaAs after KCN treatment, (a) background area ($\times 20000$), (b) island area ($\times 20000$).	104
5.12	SEM images of $CuGaSe_2$ (CGS 353) grown on (001) GaAs after KCN treatment: atomic ratio, $[Cu]/[In] = 1.29$, (a) plain view ($\times 20000$), (b) side view ($\times 20000$).....	105
6.1	Schematic top view of the migration enhanced epitaxy reactor.....	115
6.2	Schematic structure of the platen and the control thermocouple. (a) Top view of the platen showing two of the 9 substrate-holders and the position of the heater, (b) Cross-sectional view showing the mounting of the heater above the platen, the position of a thermocouple in the open gap, and the position of a glass substrate fitted in a holder that lies in an incision made in the platen.	116

6.3	Time-varying view factors between the main heater and the platen at 20 rpm.....	117
6.4	Time-varying view factors for the main heater at 20 rpm.....	118
6.5	Temperature profile on the platen/substrates: thermocouple reading = 650 °C, rotation speed = 20 rpm with thermal-break region.....	119
6.6	Temperature profile along the angular position: thermocouple reading = 650 °C.....	120
6.7	Temperature profile along the radial position at 140° with and without a thermal- break region: thermocouple reading = 650 °C, rotation speed = 20 rpm.....	121
6.8	The effect of the thermal-break region on the pattern of temperature profile within a substrate at $\theta = 140^\circ$: thermocouple reading = 650 °C, rotation speed = 20 rpm	122
6.9	Comparison of the modeling result to the experiment: thermocouple reading = 650 °C, rotation speed = 20 rpm	123
7.1	Schematic drawing of the precursor film structures: (a) Cu/Se, (b) In/Se, (c) Cu:Se.	125
7.2	Schematic drawing of the precursor film structures: (a) CuInSe ₂ /CuSe, (b) mixture of elemental copper, indium, and selenium.	127
7.3	A typical process for CuInS ₂ absorber layer: Cu-rich CuInS ₂ thin film is grown and the secondary phase on the surface is etched out by KCN solution.	132
7.4	Schematic structure of an as-grown single layer of the In-rich CuInS ₂	132
7.5	Bi-layer process for CuInS ₂ absorber layer deposition to prevent the formation of the In-rich CuInS ₂ secondary phase, CuIn ₃ S ₅	135

Abstract of Dissertation Presented to the Graduate School
of the University of Florida in Partial Fulfillment of the
Requirements for the Degree of Doctor of Philosophy

GROWTH KINETICS AND PROCESSINGS
OF COPPER INDIUM DISELENIDE-BASED THIN FILMS

By

Suku Kim

May, 2003

Chair: Timothy J. Anderson
Major Department: Chemical Engineering

CuInSe₂ (CIS)-based compound semiconductors are increasingly important absorber layer materials for thin film solar cells. A better understanding of the growth kinetics of CuInSe₂ thin films as a function of the process parameters would benefit the development of this technology.

The reaction kinetics for formation of CuInSe₂ from the bilayer structure InSe/CuSe was studied *in-situ* by high-temperature X-ray diffraction. The reaction pathway produces a diffusion barrier layer that can be schematically represented as InSe|CuSe → InSe|CuInSe₂|CuSe. Two different analyses based on the Avrami and the parabolic rate laws suggest that the reaction is one-dimensional diffusion controlled. The estimated apparent activation energy from each model is 66.0 and 65.2 kJ/mol, respectively. The result demonstrates that the time-resolved high temperature X-ray diffraction provides a powerful method for studying the reaction kinetics of CuInSe₂ growth.

The thermodynamic driving force for formation of copper selenide phase and the grain size distribution in CuInSe₂ films was investigated. Large grains (~ a few μm) were observed in the CuInSe₂ films annealed with a CuSe layer while films annealed without this layer exhibited very small grain size (< 0.2 μm). This result suggests a secondary grain growth mechanism driven by the surface-energy anisotropy is responsible for the increased grain size.

Epitaxial growth of CuInSe₂ and CuGaSe₂ on (001) GaAs substrates was attempted. The result shows that the crystalline structure and its quality strongly depends on the film stoichiometry, especially the [Cu]/[III] atomic ratio, with Cu-rich compositions showing higher crystalline quality.

A two-dimensional model of heat transfer in the growth reactor was developed for a rotating platen/substrate in the molecular beam epitaxial reactor that was used for film growth. Time-varying view factors were included in the model to solve the problem dynamically and to account for the fact that the platen rotating at a given angular speed. The modeling results predict the temperature uniformity on the substrate surface is good ($\leq \pm 10$ °C) at a set point temperature in the range 200 to 500 °C and rotation rate of 20 rpm.

CHAPTER 1 INTRODUCTION

This chapter presents an overview of this dissertation, description of the deposition system for processing CuInSe₂ (CIS) thin films, and finally a statement of problems addressed in this dissertation.

The second chapter reviews the key principles associated with CIS thin film photovoltaic technology. In particular, it presents the basic principles of solar cell device operation as well as specific features and recent progress in CuInSe₂-based solar cell applications. The material properties, crystal structure, chemistry, and processing of CuInSe₂ thin films are also discussed. Finally, techniques to characterize CuInSe₂ thin films are summarized.

The third chapter presents the result of a study on the reaction kinetics and pathways of CuInSe₂ film growth. The reaction kinetics for formation of CuInSe₂ from precursor films consisting of stacked binary M-Se layers were studied using high-temperature X-ray diffraction analysis. Different reaction pathways and phase transformations were observed depending on the deposited precursor film structure. For example, the isothermal phase evolution of the InSe|CuSe couple film was observed at different temperatures by *in-situ* time-resolved X-ray diffraction. The pathway produces a diffusion barrier layer that can be schematically represented as InSe|CuSe → InSe|CuInSe₂|CuSe. This product layer also serves as a nucleation barrier. As a result, amorphous and crystalline phases simultaneously grow during the isothermal heating. The rate of reaction exhibits a deceleratory behavior consistent with a diffusion-

controlled reaction mechanism. Two different analyses based on the Avrami and the parabolic rate laws were performed. The Avrami exponent for each isothermal reaction is between 0.5 and 0.8, which indicates that the growth reaction is dominantly one-dimensional, diffusion controlled. The estimated apparent activation energy for this reaction is 66.0 kJ/mol. The result from the parabolic rate law is very consistent with the Avrami analysis and an almost identical apparent activation energy (65.2 kJ/mol) was obtained.

In the fourth chapter, a thermodynamic analysis of the effect of a copper selenide phase on the grain size distribution of CuInSe₂ films is presented. The CuInSe₂ films were deposited onto molybdenum-coated soda lime glass substrates using a molecular beam epitaxy system. In this study, the composition of the as-grown CuInSe₂ films was controlled to be stoichiometric (possibly slightly Cu-rich). The a layer of CuSe was deposited on top of the as-grown CuInSe₂ films. These bi-layer samples, CuInSe₂/CuSe, were annealed under various conditions. The grain size distribution of the annealed films was estimated using SEM images and the full width of half maximum (FWHM) of XRD peaks. Large grains (a few μm) were observed from samples annealed with the copper selenide layer while the samples annealed without this layer showed very small grains (< 0.2 μm). After annealing the CuInSe₂/CuSe films, the peak area of the (112) orientation consistently increased, while that of the (220)/(204) orientations decreased, suggesting a difference in surface energy is important. The results were interpreted by assuming a thermodynamic driving force, surface-energy anisotropy, is responsible for the grain size increase of the CuInSe₂ film.

In the fifth chapter, preliminary results on the epitaxial growth of CuInSe₂ and CuGaSe₂ films on (001) GaAs substrates are discussed. Previous work in our research group on epitaxial growth of CuInSe₂ films on GaAs (001) was reported (Stanbery 2002). Under certain conditions, crystal structure of the CuInSe₂ films was found to be Cu-Au (CA) structure rather than more commonly observed chalcopyrite (CH) structure. The results reported in this chapter show that the crystal structure and its quality depended on the film stoichiometry, especially the [Cu]/[III] atomic ratio. SEM and AFM examination revealed that the Cu-rich CuInSe₂ and CuGaSe₂ films consisted of a highly oriented array of faceted islands on the surface, and that a textured background region lies adjacent or beneath those islands. The specific surface morphology was an indication of the epitaxial growth or textured structure of the film. It is believed that Cu-rich compositions quality of the epitaxially grown films. There was a structural and compositional distinction between the islands and the background regions of Cu-rich films. More extensive study is needed to establish detailed process parameters and improve the quality of the epitaxially grown films.

The final chapter presents a thermal mode of the migration enhanced epitaxial (MEE) deposition system that was used to produce the CuInSe₂-based films. The finite element method was used to model the heat transfer in a MEE reactor. The thermal domain included is a rotating platen that holds nine substrates. Time-varying view factors were employed to solve the problem dynamically, and account for the rotational motion. A two-dimensional temperature profile of the platen and the substrates was obtained. The relationship between the actual substrate temperature and the control thermocouple was also modeled. It is demonstrated that the existence of thermal contact resistance between

the platen and the substrates improves the temperature uniformity of the substrate. The modeling results predict that the temperature distribution of the substrate surface showed good uniformity of the given conditions, a set point temperature in the range 200 to 500 °C and rotation rate of 20 rpm.

1.1 System Description

The photovoltaic research group at the University of Florida developed a plasma-assisted migration enhanced epitaxy (PMEE) deposition system to produce CuInSe₂-based absorber layers for thin film solar cell applications. The system is basically a variant of the molecular beam epitaxy (MBE) system. In addition to the capabilities of a typical MBE, it is capable of processing nine samples situated on a large rotating platen. Square substrates of 2 in.×2 in., 2 in diameter wafers (Si or GaAs) or 1 cm×1 cm of square substrates can be loaded onto the platen. The migration enhanced feature of the system is established by the sequential deposition of each source through a revolution of the platen rather than simultaneous co-deposition of all the sources.

As a modified MBE system, it creates an ultra high vacuum environment and molecular beam fluxes of the elemental sources. The pumping unit consists of three mechanical pumps, one large capacity diffusion pump, a turbo molecular pump (TMP), and a liquid nitrogen cryogenic pump. The base pressure can be maintained as low as 8×10^{-9} Torr with a cryogenic pumping. The pressure during deposition is typically in the range 10^{-8} to 10^{-7} Torr depending on the magnitude of the source fluxes. The pressure can elevate as high as 10^{-5} Torr range when an inert gas is introduced to the system to generate plasma. In standby mode, the system pressure is maintained as low as 5×10^{-7} Torr by the turbo molecular pump and a back-up mechanical pump.

The deposition chamber is divided into four zones, as shown in Figure 1.1. It consists of a heater zone, a metal deposition zone, a load-lock zone, and a chalcogen deposition zone (as reviewed in counter-clockwise direction). As described above, the system adopts a rotating platen that delivers the substrates to all the zones sequentially and periodically. A radiation heater is located in the heater zone; hence, the substrates and the platen are heated while they pass through the heater zone. In other zones, the substrates are slowly cooled since there is no direct heating source. A slight non-uniform temperature distribution on the platen and substrates is expected due to the complex design. Two effusion source cells are located in the metal deposition zone. Impingement of Cu and In fluxes occurs while the heated substrates pass through the metal deposition zone. Rotation of the platen continuously delivers the substrates to the cooling zone (or load-lock zone) where neither deposition nor heating occurs. Finally, the substrates enter the chalcogen deposition zone and deposition of Se or S occurs. The cycle is repeated with the rotational motion of the platen. The above description about the rotational motion and sequential deposition assumes counter-clockwise rotation of the platen. The direction of the rotation, of course, can be either clockwise or counter-clockwise so that the sequence of deposition may be reversed. The selenium deposition zone was isolated from the other zones to minimize selenium deposition in the other parts of the system. Selenium has the highest vapor pressure among all the elemental sources and correspondingly creates the highest background pressure; hence, it can cause serious contamination of other parts, such as the ion gauges. The substrates are loaded into the PMEE system through the load-lock zone. A separate chamber, the load-lock, is

connected to the main chamber, which makes it possible to move the substrates in and out without venting the main chamber.

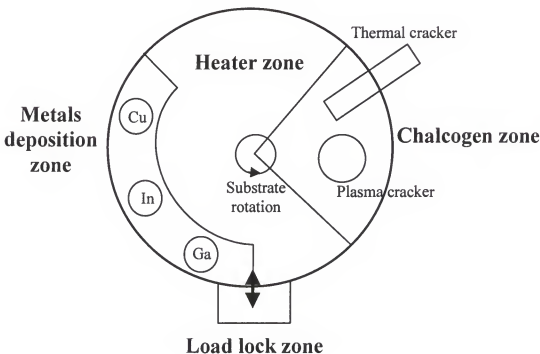


Figure 1.1 Schematic top view of the plasma-assisted migration enhanced epitaxy (PMEE) system

Five effusion source heaters (Cu, In, Ga, Se, and S) are located in the main chamber. Three thermal evaporation sources produce create copper, indium, and gallium fluxes. Due to the high melting temperatures and the high sticking coefficients of copper and gallium, a dual filament system was adopted in these sources to ensure a completely melted surface and prevent condensation on the wall near the exit of the effusion cell.

The source heater for selenium was more complex. It consisted of a cracker and a crucible. It is known that selenium vapor evaporates as a mixture of several molecular phases (e.g., Se, Se_2 , Se_6 , and Se_8). The high molecular weight species do not react as readily as the other species on the substrate even at high temperature.

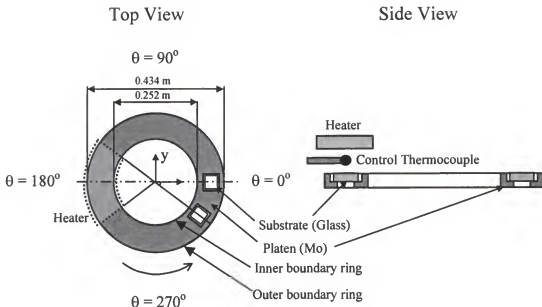


Figure 1.2 Schematic structure of the platen and the control thermocouple. (a) Top view of the platen showing two of the 9 substrate-holders and the position of the heater, (b) Cross-sectional view showing the mounting of the heater above the platen, the position of a control thermocouple in the open gap, and the position of a glass substrate fitted in a holder that lies in an incision made in the platen.

The thermal cracker was designed to reduce the concentration of the high molecular weight species. The temperature condition for the cracker during deposition is usually in the range 350 to 1000 °C. The second selenium source is located in the chalcogen deposition zone. This source was designed for plasma cracking of a selenium molecular flux to yield lower molecular weight Se_x . Electron cyclotron resonance (ECR) plasma is generated and maintained in a sapphire tube that works as a wave-guide and for the passage of selenium molecular flux. This source cell can be used for both selenium and sulfur. Both sequential and simultaneous deposition can be conducted by controlling these effusion cells.

The fluxes from the copper and the indium sources are measured *in-situ* by EIES sensors. A closed loop feed-back control scheme implemented using the EIES sensors

for the Cu and the In sources. The EIES sensors can be calibrated by quartz crystal monitors (QCM) that are located over the source cells. There is no sensor that directly measures the chalcogen (selenium and sulfur) flux rate *in-situ*; hence, the flux rate is calculated by depositing the chalcogens on a substrate at room temperature and measuring the film thickness. For the chalcogen sources, a closed loop feed-back control based on temperature is used.

Along with the unique features of the system described above, the current growth system has both advantages and limitations compared to other deposition techniques. First, it has the advantages of the MBE system, including a clean ultra high vacuum environment and a relatively precise control over the flux. Combined with the shutter operation and the rotational motion of the platen, an operation of atomic layer deposition mode is also possible. In addition, the design has a relatively high sample throughput since nine samples processed in one batch. Adopting the sequential deposition scheme gives more versatile tool, *i.e.*, the rotation speed and the rotation direction can be varied.

There exist some disadvantages of this system as well. Due to the rotational motion of the platen/substrates, direct *in-situ* measurement of the substrate temperature is very difficult. The measurement thermocouple is currently located in the gap between the platen and the heater, and reads a temperature at a fixed position independent of rotation. The localized heater location in a rotation system creates a time-dependent non-uniform temperature distribution on the substrate surface. The growth rate is significantly limited by the chalcogen flux delivery. Even with high chalcogen flux rate ($[\text{Se}]/[\text{Cu}]+[\text{In}] > 5$), it is a challenge to deliver sufficient chalcogen incorporation for growth at high temperature. This is because the chalcogen deposition zone is removed from the metal

deposition zone, and the transit time between the zones allows the high-vapor-pressure material to be easily re-evaporated from the surface. As a result, the maximum flux rates of copper and indium should be also limited, thus making it difficult to grow at high rate.

1.2 Statement of Problems

Cu(In,Se)Se₂ (CIGS)-based compound semiconductors are increasingly important as the absorber layer material of thin film solar cells. The energy conversion efficiency of the CIS-based solar cells has reached that of the best solar cells made of crystalline silicon and gallium arsenide. While there have been many studies of the growth mechanism of the CuInSe₂ film, it is not yet fully understood partly due to complex phase evolution and defect chemistry in that material system. In a Cu-In-Se ternary system, various binary and ternary phases can be present and transformed into many different phases during synthesis of the absorber film. For these reasons, the fundamentals of the growth mechanism for CIGS synthesis are still ambiguous. Such lack of scientific and engineering basis leads to difficulties in scaling up promising laboratory processes.

Among many important issues, the following five problems are addressed in this dissertation.

1. Quantitative investigation of the reaction kinetics of CuInSe₂ thin film growth using *in-situ* time-resolved, high-temperature X-ray diffraction.
2. Study of the grain growth mechanism of CuInSe₂ thin films: influence of the CuSe phase.
3. Epitaxial growth of CuInSe₂ and CuGaSe₂ films on (001) GaAs substrates.
4. Thermal modeling of the PMEE growth system to better understand the relations between the process parameters and the material properties of the grown films.
5. Development of a suitable growth process of CuInSe₂-based absorber layer for material property improvement and process scale-up.

CHAPTER 2

BACKGROUND AND LITERATURE REVIEW OF SOLAR CELL AND CUINSE₂-BASED MATERIALS

This chapter discusses the key principles and technologies in CIS thin film solar cells. In particular, section 2.1 describes basic principles and fundamentals of the solar cell device, and section 2.2 presents specific features and recent progress in CuInSe₂-based solar cell applications. Section 2.3 describes the material properties, crystal structure, chemistry, and processing of CuInSe₂ thin films. Section 2.4 summarizes some of characterization techniques for CuInSe₂ thin films.

2.1 Solar Cell Fundamentals

A photovoltaic device or solar cell converts sunlight (or photon energy) directly into electricity using the photovoltaic properties of suitable materials. The photovoltaic effect was discovered by Becquerel, in 1839. Solar cell technology has developed tremendously during the last three decades (Möller 1993). Silicon was the first commercially used solar cell material and is still the most usually produced by industry. A wide range of semiconductors, such as GaAs, CdTe, InP, CdS, and CuInSe₂-based materials, is currently being explored for their potential use in photovoltaic applications.

The wavelength distribution of the sunlight follows approximately the radiation distribution of a black body at 6000K; however, there are some deviations in the actual spectral distribution due to absorption effects in the atmosphere. The radiation power is usually measured in air mass (AM) units. For example, AM0 corresponds to the spectral distribution measured outside the atmosphere perpendicular to the direction of the sun,

and AM1 corresponds to the one measured on the earth's surface. When the sun is about 42° above the horizon, the path length is 1.5 atmospheres. The corresponding spectral distribution is referred to as AM1.5. In the U.S. photovoltaic program, the spectral distribution for an AM1.5 radiation source with a total power density of 0.855 kW/m^2 has been adopted as a standard spectral distribution (Bube 1998). Those spectral distributions of the radiation are displayed in Figure 2.1.

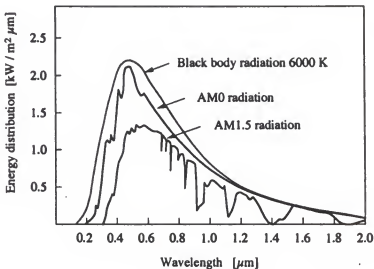


Figure 2.1 Spectral distribution of sunlight. (Figure taken from Möller 1993)

In photovoltaic materials, illumination (photon energy) generates electron-hole pairs, and recombination of the pairs can occur at the same time. Both are non-equilibrium processes and controlled by the device parameters. The photovoltaic device has a built-in electrical field that separates the photo-generated electrons and holes. The internal electric field is built by formation of p-n junction, Schottky barrier, or a MIS (metal-insulator-semiconductor) structure in the device. For most solar cells, the p-n junction formation is used to build the internal electric field. In thermodynamic equilibrium, when no electrical current flows, the separated minority carriers are accelerated by the electric field to the p-type side of the junction (Li 1993). Electrical current should flow

under illumination by this mechanism when those two sides of the p-n junction are connected externally. A band diagram and schematic view of a p-n junction solar cell are depicted in Figures 2.2 and 2.3.

Important solar cell parameters can be determined from the current-voltage curve (Figure 2.4). The short-circuit current, I_{SC} , is the current flow when the voltage drop across the junction is zero. From the equivalent electrical circuit of a p-n junction (Figure 2.5), it is found that I_{SC} is equal to the photo-generated current, I_L , when the series resistance (R_S) is zero, and R_S reduces I_{SC} .

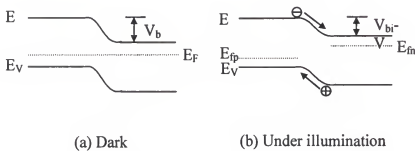


Figure 2.2 Band diagrams of an unbiased p-n junction solar cell: (a) in the dark and (b) under illumination.

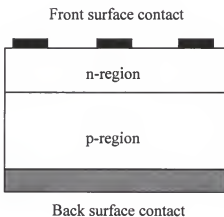


Figure 2.3 Schematic diagram of a p-n junction solar cell.

The open-circuit voltage, V_{OC} , corresponds to the voltage drop when the current flow is zero. The electrical power output is $P = IV$, which is equal to the area of the rectangle in Figure 2.4. The maximum area of the rectangle will be $P_{max} = V_p I_p$ for a given current-voltage curve. The shape of the curve depends on the load resistances, R_s and R_{sh} . The fill factor, FF , is the parameter that determines the shape of the curve. It is defined by

$$FF = \frac{V_p I_p}{V_{OC} I_{SC}} \quad (2.1)$$

A more square-like curve leads to a larger fill factor, FF . The value of FF varies between 0.7 and 0.9 for the cells with acceptable efficiencies.

The energy conversion efficiency, η , is determined by

$$\eta = \frac{V_p I_p}{P_m} = \frac{FF V_{OC} I_{SC}}{P_m} \quad (2.2)$$

where P_m is the total power generated by illumination (photon energy). Therefore, the value of each parameter in equation (2.2) significantly affects the performance of the solar cell. These parameters are not independent, and are controlled by the structural and electrical properties of the solar cell device.

To make solar cells a competitive energy source, several challenges need to be overcome. The challenges include achieving high performance (energy conversion efficiency), low production cost, and high durability to the environment, and long term reliability. Development action should consider these factors.

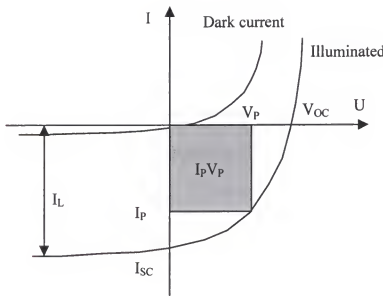


Figure 2.4 Current-voltage characteristics of a p-n junction diode in the dark and when illuminated, defining the basic parameters.

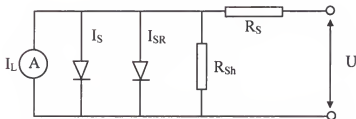


Figure 2.5 Equivalent electrical circuit of a p-n junction for the two-diode model with diffusion I_S and recombination current I_{SR} , series R_S and shunt R_{Sh} resistance, and light-generated current I_L .

2.2 Cu(In,Ga)Se₂-based Thin Film Solar Cells

A wide range of semiconductors, including GaAs, CdTe, InP, CdS, and CIGS-based materials, is being explored for their potential use in photovoltaic applications. Among those candidates, copper indium diselenide, the CIGS-based thin film solar cell, is considered the most promising technology due to its structural and electrical properties, including an extremely high absorption coefficient and stable electro-optical properties.

(Möller 1993, Bube 1998, Li 1993). The absorption coefficient is one of the most important parameters that determine the performance of the solar cell device and production cost. With higher absorption coefficient, absorber films can be thinner, which is directly related to the material cost. The values for CuInSe₂, silicon and other important semiconductors are shown in Figure 2.6.

Other advantages of CIGS-based materials include a band gap energy (1.0 ~ 1.7 eV) that is suitable for either homojunction or heterojunction device types. A lattice structure and an electron affinity that matches well with common n-type window materials are also positives of this material (Möller 1993). A schematic structure of a traditional CuInSe₂-based solar cell is depicted in Figure 2.7.

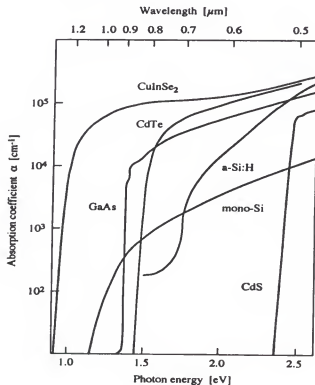


Figure 2.6 Absorption coefficient as a function of the photon energy for selected semiconductor materials (Figure taken from Möller 1993).

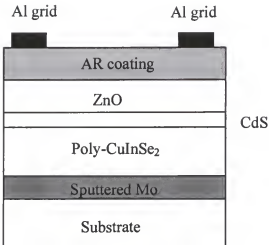


Figure 2.7 Schematic structure for a CuInSe_2 thin film solar cell.

Wagner *et al.* produced an early high-efficiency $\text{CuInSe}_2/\text{CdS}$ solar cell (12.5%) for the first time by evaporating CdS onto a single crystal of CuInSe_2 in 1974 (Birkmire 2001). Numerous efforts have been made to develop processes that improve the device performance, *e.g.*, using the alloys of $\text{Cu}(\text{In},\text{Ga})\text{Se}_2$ and $\text{CuIn}(\text{S},\text{Se})_2$, which are wider energy band gap materials. A graded energy band gap structure was developed to increase the open-circuit voltage while maintaining the short-circuit current.

Recent results show that the cells can be prepared by a variety of methods, while obtaining efficiencies approximately 13% for CuInS_2 and approaching or exceeding the 16% level for $\text{Cu}(\text{In},\text{Ga})\text{Se}_2$ (Nadenau 1995). The most recent efficiency reported by NREL is 18.8% ($\text{Cu}(\text{In},\text{Ga})\text{Se}_2$) for an area of 0.44 cm^2 , which is similar to that of the best multicrystalline silicon devices of 19.8% (Birkmire 2001, Zhao 1998). These results suggest that the CIGS-based solar cell is a very promising alternative to the crystalline-silicon technologies. NREL has also reported a 43.9 cm^2 area device with an efficiency of 13.7%. Furthermore, the high efficiency devices have been produced by several groups, and have shown no evidence of degradation of the CIS layer with time or light

exposure. These results clearly show the high potential of CIS-based thin film solar cells in fabricating high efficiency solar cell modules with low production cost and high stability, the most important factors in commercializing solar cell modules.

In the industrial sector, Shell Solar, Inc. is at the most advanced stage, offering Cu_{(In,Ga)Se₂}-based 12V modules to customers. Global Solar Energy is developing flexible module manufacturing systems using polyimide or stainless steel as substrates. In addition to the companies mentioned above, there are a number of smaller companies that are at early stages of commercialization of CIS-based modules. Unisun and International Solar Electric Technology, Inc. are developing CIS-based photovoltaic technology using non-vacuum deposition processes for the absorber formation. Their technologies involve spraying/printing of precursor powders onto a Mo-coated glass substrate, followed by reactive sintering (Birkmire 2001, Roedern 1999, Norsworthy 2000).

It is still a challenge to produce large-area modules reproducibly at low cost for electric power generation. The lack of understanding of the quantitative correlation between the device performance and the material properties has limited progress towards manufacturing the high efficiency photovoltaic modules at large scale (Rockett 1994).

2.3 Fundamentals of CuInSe₂-based Materials

2.3.1 Crystalline Structure and Solid State Electronics of CIS-based Materials

CuInSe₂ crystallizes in a diamond-like lattice structure with a face-centered tetragonal unit cell that is termed the chalcopyrite structure. The crystal structure is considered as isoelectronic analogs to binary II-VI or III-V semiconductors with the zinc-blende (sphalerite) structure (Fig. 2.8) (Givargizov 1991). Each selenium atom serves as the center of a tetrahedron of two Cu and two In atoms, and each metallic atom is surrounded

by a tetrahedron of selenium atoms. Each anion (selenium) has two A (copper) and two B (indium) cations as nearest neighbors, whereas in the zinc-blende structure, each anion has four cations of the same kind as nearest neighbors (Möller 1993). The lattice parameters of CuInSe₂ crystal structure are $a = 0.5784$ nm and $c = 1.1614$ nm.

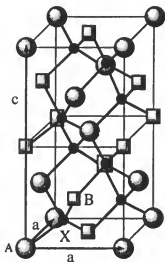


Figure 2.8 Tetragonal unit cell of an ABX_2 chalcopyrite lattice: A = Cu, B = In, and X = Se for CuInSe₂ (Figure taken from Bube 1998)

There are twelve intrinsic point defects that can form in the ABX_2 chalcopyrite lattice. They are three interstitials (A_i , B_i , X_i), three vacancies (V_A , V_B , V_x), and six anti-site defects. Some of these intrinsic defects are shallow-level defects that can be used to dope the crystal. In the CIS-based materials, the electrical properties (carrier type, carrier concentration, and mobility) are determined by the intrinsic defects depending on the crystal composition instead of a doping by shallow level impurities (extrinsic doping). An essential feature of chalcopyrite semiconductors is the high density of point defects that influence not only the optical properties, but also the conductivity and other electrical properties. Numerous efforts have been made to reveal the physics and roles of the intrinsic defects (Chang 1999, Burgelman 1997, Schön 2000, Klais 2000). It is believed

that V_{Se} , V_{Cu} , Cu_{In} , and the defect pair ($2V_{Cu}$ - In_{Cu}) play a dominant role in determining the electrical properties in $CuInSe_2$ (Möller 1993, Givargizov 1991). No conclusive experimental or theoretical results exist, however, that allow the determination of the structural and electronic properties of these defects in $CuInSe_2$ or any other copper ternaries and quaternaries. This issue remains ambiguous.

Both $CuInSe_2$ and $CuInS_2$ can be made n- or p-type by changing the stoichiometry of the crystals, whereas $CuInTe_2$ and $CuGaSe_2$ can so far only be prepared as a p-type material. It makes it difficult to fabricate a solar cell device with these materials. As an effort to improve the controllability on the electrical properties of the chalcopyrite thin films, extrinsic doping technology has been studied. It was aimed at improving the performance of $CuInS_2$ -based solar cells; however, it has not been successfully employed for device fabrication to date.

Typical values for the net hole carrier concentration in the $CuInSe_2$ absorber layer (single- and polycrystalline) are in the range 10^{16} to 10^{18} cm^{-3} . The carrier concentration sensitively changes depending on the stoichiometry of the materials. Variation of carrier concentration as a function of the composition of the films is depicted in Figure 2.9 (Möller 1993). The graph shows that the carrier concentration drops by several orders of magnitude in a narrow range of composition, and the conductivity changes from p- to n-type behavior. For this reason, controllability and reproducibility on the composition are very important issues.

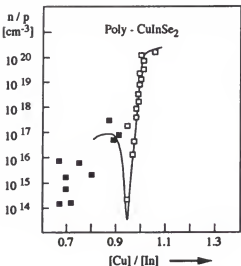


Figure 2.9 Carrier concentration of p- and n-type CuInSe_2 single crystals as a function of the composition ratio, $[\text{Cu}]/[\text{In}]$. Black symbols are n-type and white symbols are p-type. (Figure taken from Möller 1993)

2.3.2 Structure, Chemistry, and Processing of CIS-based Thin Films

2.3.2.1 Structure and chemistry of CIS-based thin films

CIS-based materials exhibit a distinct transition in morphology and phase segregation behavior passing through the stoichiometry ($[\text{Cu}]/[\text{In}] \approx 1$). The distinction between the Cu-rich and the indium-rich films includes the growth mechanism as well as morphology and micro-structure of the films. In accordance with the pseudobinary ($\text{Cu}_2\text{Se}-\text{In}_2\text{Se}_3$) phase diagrams (Nadenau 1995), phase segregation in Cu-rich CIS thin film is attributed to the formation of copper-chalcogenide secondary phases. The secondary phases are degenerate p-type semiconductors, and dominate the optoelectronic and the surface properties of Cu-rich films. Most growth techniques used in depositing thin films, especially physical vapor deposition processes, are generally far from equilibrium, thus, to know when and where the second phases form is critical to fabrication of CIS-based solar cells and development of CIS growth process. In Cu-rich CIS films, the individual grains are significantly larger than those in indium-rich films. These grains prefer to be

(112) oriented in Cu-rich films whereas indium-rich films additionally exhibit strong (220)/(204) orientation.

For Cu-rich CIS system, the secondary phase observed is copper chalcogenide or copper selenide, mostly Cu_{2-x}Se , and CuSe (Rockett 1994, Ramanathan 1998, Niemi 1990). Surface composition analysis revealed that even a minor excess of copper in the bulk leads to very Cu-rich surfaces (Nadenau 1995, Rockett 1994, Ramanathan 1998, Tuttle 1995). It seems to be caused by secondary phase segregation at the film surface. X-ray Diffraction (XRD) also indicated segregation of these phases on the surface. The Cu-rich secondary phases can be selectively removed by etching with KCN solution. The compositional variation of Cu-rich films due to the KCN treatment has been shown to be consistent with removal of the copper selenide and to be extremely rapid, as expected for removal of a near-surface layer (Rockett 1994). CIS-based thin film is often grown through deposition of Cu-rich films and etching the secondary phases. Several models for the growth mechanism of CIS thin films under a Cu-rich composition have been proposed. Klenk *et al.* (Klenk 1993) reported a significant difference in surface and bulk compositions in co-evaporated $\text{Cu}(\text{In},\text{Ga})\text{Se}_2$ (CIGS) polycrystalline films grown under Cu-rich conditions, and proposed a growth model that the grain growth is controlled by the interaction of vapor-liquid-solid phase (VLS model). Wada *et al.* (Wada 1997) suggested that growth of the CIS thin film takes place through the segregated Cu_2Se solid phase by a “topotactic reaction”, after they observed a Cu_2Se phase on the CIS grain surfaces by transmission electron microscopy (TEM). Drastic changes of average molecularities from $m > 1$ to $m = 0.92 \sim 0.93$ ($m = [\text{Cu}]/[\text{In}]$ atomic ratio) and hole concentrations from $p > 10^{19} \text{ cm}^{-3}$ to as low as $p = 7.5 \times 10^{16} \text{ cm}^{-3}$, have been observed from a

epitaxially grown CuInSe₂ by MBE before and after the KCN treatment. High hole concentration and Cu-rich compositions of the as-grown films were attributed to the copper selenide phase. Their result strongly suggests that the stoichiometry of CIS films (the ratio [Cu]/[In]) is slightly below unity and independent of the supplied Cu- and In-flux; the stoichiometry of the CIS films are self-limiting so as not to exceed unity under Cu-rich growth conditions by operating in the 2-phase region of the phase diagram.

For indium-rich thin films, the phase segregation behavior and the growth mechanism are evidently different from those of Cu-rich thin films. Indium-rich crystallites are tetrahedrally shaped, which indicates an anisotropy in the growth velocity of the {112} planes (Nadenau 1995). This anisotropy, ascribed to limitations in chalcogen supply, is not observed in Cu-rich films. For a wide range of indium-rich compositions, the indium chalcogen secondary phase is not observed in the films. The whole region consists of single phase chalcopyrite. At the surface, however, a secondary phase has been observed in the near surface region of indium-rich films. It was originally termed an ordered defect crystal (ODC) phase. The phase (CuIn₃Se₅) is a defect chalcopyrite structure and n-type due to strong compensation of the defects. The lattice constant of this phase nearly matches that of the CuInSe₂ lattice. The ODC was found in most high efficiency CuInSe₂ solar cells and believed to do an important role in determining the electrical properties of the device. Further study is needed to better understand the fundamentals of CuInSe₂-based thin film.

2.3.2.2 Processing of CIS-based solar cells

Co-evaporation is one of the most widely used processes for growth of CIS-based thin films. The technique delivers a flux of each source to the substrate simultaneously. This is often considered as an appropriate way to grow high quality films; however, it also has

limitations for achieving uniform film deposition on a large area substrate. A typical substrate temperature during deposition is in the range 450 to 550°C, which is needed to form the absorber from the elements and to form large grain size. The simplest co-evaporation process design is the 'single-layer process'. In this process, the flux rate of each source is maintained constant. It delivers a film that is homogeneous across the thickness since the elemental evaporation ratios directly determine the final film composition. Better controllability and reproducibility are expected due to its simplicity and directness. It was recognized early, however, that a single-layer does not result in optimum cell performance.

The empirical approach of depositing a bilayer, *i.e.* indium-rich layer onto a Cu-rich layer, was introduced to improve the film quality (Nadenau 1995). The co-evaporation process allows changing the film composition across the film thickness by changing the elemental flux rates with time. As pointed out above, the Cu-rich thin film is known for its large grain size and higher crystallinity. The CIS films are grown under Cu-rich conditions during most of the growth process to achieve the benefits of large grain size and high crystallinity. The desired composition, slightly indium-rich, can be attained through the second layer deposition. By this way, the bilayer process can grow a large grain CIS thin film that has slightly indium-rich composition.

Tuttle *et al.* (Tuttle 1995) proposed a more detailed growth mechanism in their growth model that is based on the VLS model. It consists of (a) initial atomistic accommodation, reaction, and nucleation, (b) CuInSe₂ and Cu_xSe island formation, (c) CuInSe₂ coalescence with vertical phase separation, and (d) Cu_xSe conversion and local epitaxial growth. The phase segregation in (b) is lateral, that is, CuInSe₂ and Cu_xSe co-exist side

by side. According to their model, the lateral phase segregation is transformed to a vertical one where two phases exist as separate layers, layer by layer. Many variants of the bilayer process have been used to grow high quality CIS thin films.

The sequential deposition process has been also widely used and studied. Its advantages are its potential for uniform deposition on a large area substrate and the simplicity of the process. The precursors, elemental layers or binary phase layers (In-Se and Cu-Se) are usually deposited at low temperature. It is followed by selenization and annealing at high temperature. Several research groups have fabricated the CIS-based photovoltaic devices with efficiency over 12% using the sequential process. The precursor layers can be grown by various techniques, such as sputtering, evaporation, electro-deposition, and e-beam evaporation.

Another critical process that significantly affects the device performance is the deposition of the buffer layer. To date, the highest conversion efficiencies of CIS-based solar cells have been achieved using a CdS buffer layer deposited by chemical bath deposition (CBD), followed by deposition of a ZnO window layer. There have been many studies to better understand the roles of the CdS buffer layer in the solar cell operation. The Cd atoms are believed to form Cd_{Cu} interstitial donor defect, providing the required near-interface charge and restoring the positive surface charge. Kronik *et al.* postulates that the donor defect creates significant band-bending at the interface (Kronik, 2000). Several research groups identified the diffusion of Cd into the absorber layer. Nakada *et al.* (Nakada 1999) provided direct evidence of Cd diffusion using high resolution transmission electron microscope (TEM) equipped with energy dispersive x-ray spectroscopy (EDS). CBD grown CdS buffer layer has its own advantages, the

simplicity of the process, good reproducibility, and potential for large area processing. However, there is a great interest in replacing CdS by a cadmium-free buffer layer for environmental reasons and possible gains in efficiency associated with wider band gap energy. For some processes, a vacuum deposition technique would be competitive with other processes. CBD grown $\text{In(OH)}_x\text{S}_y$ shows similar result to the standard CBD grown CdS (Birkmire 2001, Braunger 1996, Hariskos 1996). NREL recently reported 13.5% efficiency $\text{Cu}(\text{In},\text{Ga})\text{Se}_2$ solar cell without any buffer layer (Ramanathan 1998). Deposited films of InSe and InS are also potential candidates since it can eliminate the step of breaking vacuum after the absorber layer growth. It will significantly reduce processing time and contamination problem.

2.4 Characterization Techniques for CIS-based Films

The surface morphology and the cross sectional structure of CIS thin films can be studied using scanning electron microscopy (SEM) (Tuttle 1991, Walter 1996, Rastogi 1999). The instrument uses electrons accelerated by tens to hundreds kilovolts to produce the image, and it can resolve micro-scale objects. It is a versatile instrument for examining the microstructure of solid surfaces, because it combines high spatial resolution with depth of field in the same image, and requires minimal sample preparation (Runyan 1998). Atomic force microscope (AFM) can provide more detailed information on the surface morphology, *e.g.*, microstructures and roughness of the surface.

SEM can be equipped with energy dispersive spectroscopy (EDS) or wavelength dispersive X-ray spectroscopy (WDS) that are compositional analysis instruments. Both techniques have been widely used for measuring the bulk composition of CIS thin films. Reliability of the results significantly depends on the film structure since those

instruments collect the information of local region of the objects. Both techniques, hence, are convenient and reliable for compositional analysis of homogeneous films. Those techniques, however, may not be very reliable for multi-layer structures or sequential precursor layers that have compositional variation with film depth.

Auger electron spectroscopy (AES) has been used for obtaining depth profiles of elemental composition in CIS thin films. Auger electron spectroscopy is a surface sensitive probe and uses an incident electron beam of 3 to 5keV that is somewhat lower than that used for the electron microscope, but like a microprobe, the beam scatters within a small sample volume. To depth profile, sputter etching is used while an Auger spectrum is being collected. As the etch proceeds, Auger electrons from specimen provide a measure of the elemental concentration of a freshly exposed layer. To achieve the best result, the etch rate should be carefully calibrated considering composition, structure, and chemistry of the sample. Different phases along the film depth can be detected by analyzing the compositional variation. Phase segregation on the surface or at the back contact has been observed and analyzed using AES (Rockett 1994, Nakada 1999, Scheer 1994).

X-ray diffraction (XRD) is one of the most commonly used techniques for characterization of crystalline phases, *e.g.*, thin films, single crystals, and powders. It can provide information about crystalline structure, stress, and existence of specific phases in the samples. One of its advantages is that there exists an enormous amount of reference for XRD spectrum on many crystalline phases.

Recently, Raman spectroscopy has been used as another tool to detect various phases in CIS films. Some of the secondary phases in CIS thin films have overlapping XRD

peaks; hence, it is not easy to resolve the phase. Raman spectroscopy can provide additional information to assist in detection of these phases. Micro-Raman technique has been employed to detect secondary phases in a micro-structure on the surface of CIS thin film (Stanberry 1999).

Inductively coupled plasma (ICP) is known as one of the most reliable quantitative analytical techniques for measuring the overall composition of various samples. Sample preparation step is critical to achieving a reliable result. The samples, *e.g.*, thin film, single crystalline, or powder, need to be completely dissolved in an appropriate solvent. The dissolved sample is fed into the instrument and fragmented to the elemental level by ICP. Photons are released from the reaction in the plasma. With a unique wavelengths for each element, the intensity of the peaks is proportional to the absolute amount of the corresponding element in the sample. It is noted that only the overall composition of the samples can be obtained by measuring the peak intensity. Our research group used combination of EDS (or WDS) and ICP to achieve compositional analysis.

CHAPTER 3

REACTION KINETICS AND PATHWAYS OF CUINSE₂ GROWTH FROM BILAYER PRECURSOR FILMS: TIME-RESOLVED HIGH TEMPERATURE X-RAY DIFFRACTION STUDY

3.1 Introduction

Compound semiconductors based on CuInSe₂ are increasingly gaining acceptance as absorber-layer materials for thin film solar cells. The energy conversion efficiency of CuInSe₂-based solar cells has already reached that of the best solar cells made of crystalline silicon and of gallium arsenide. While there have been many studies of the growth mechanism for CuInSe₂ films, (Tuttle 1995, Rockett 1994, Klenk 1993, Nadenau 1995) to date key details remains not fully understood partly due to the complex phase evolution and defect chemistry present in the material system. Various binary and ternary phases can be simultaneously present in a Cu-In-Se ternary system, (Klenk 1993, Nadenau 1995, Change 1999) and furthermore, phase transformations may occur during the growth processes. Given that important transformations occur during the growth process, ex-situ studies may fail to reveal key aspects of the reaction kinetics of CuInSe₂ formation. A more promising approach is to conduct an *in-situ* study of the phenomena using time-resolved high temperature X-ray diffraction analysis. This technique infers kinetic information from changes observed in the XRD data as a function of time as the film is heated. Careful analysis of *in-situ* XRD data with an advanced software JADE 6 (JADE) permits the quantitative investigation on the reaction kinetics.

The process followed to generate a CuInSe₂ film consists of starting with a stack of two binary films serving as a precursor. Examples of stacked binary films are InSe/CuSe

(*i.e.*, CuSe film grown over an InSe film), InSe/Cu:Se (*i.e.*, an elemental mixture of copper and selenium deposited over an InSe film), and CuSe/In:Se. In all cases, the bottom binary films were grown over a thin (0.4 mm) sodium free glass substrate. The films were deposited in a modified molecular beam epitaxy reactor, and the total thickness of the stack was approximately 800 nm. The precursor stack is then heated to initiate a reaction leading to the formation of CuInSe₂ film, and the evolution of the reacting system is observed via *in-situ* high temperature XRD.

This article presents the results of an *in-situ* isothermal time-resolved X-ray diffraction study of CuInSe₂ film growth from the binary precursor stack CuSe/InSe. Quantitative analyses were performed to estimate the reaction order and the apparent activation energy, as well as to elucidate mechanistic details of the film growth pattern.

3.2 Experiments

3.2.1 Preparation of Precursor Films

The deposition method used to grow the precursor films is called migration enhanced epitaxy (MEE), a variant of the classical molecular beam epitaxy (MBE) approach. As in MBE, an ultra high vacuum environment and effusion cells are employed to generate molecular beam fluxes of all the elemental sources. In contrast with a typical MBE system, the MEE reactor used is capable of accommodating multiple substrates (up to nine) positioned on a large rotating platen. Another unique feature of the MEE system is the sequential deposition of each source material through a revolution of the platen, rather than a simultaneous co-deposition from all the sources. A most relevant difference, however, lies on the fact that the rotating platen of the MEE system passes each substrate through a flux-free zone, namely a relaxation zone that enhances the potential for adsorbed atoms to migrate seeking the most thermodynamically favored configurations.

The direction of rotation can be either clockwise or counter-clockwise, so that the sequence of deposition may be reversed. The base pressure of the system can be maintained as low as 8×10^{-9} Torr, and the pressure during deposition is in the range of 10^{-7} - 10^{-8} Torr depending on the operation conditions. Further details of the deposition technique and experimental apparatus are given elsewhere (Stanberry 2002).

For the InSe/CuSe structure, first an indium selenide layer was grown on top of a thin (~0.4 mm) sodium-free thin glass substrate in the MEE system with a substrate temperature of approximately 250 °C. The films were made to have a slightly selenium-rich composition ($[In]/[Se] \sim 0.95$). Second, a copper selenide layer was deposited on the as-grown InSe layer at a lower temperature condition (~150 °C) to minimize any potential reactions between the InSe and CuSe layers. The final stacked binary structure is depicted in Figure 3.1. Room temperature XRD data shows that the InSe phase is amorphous, and that the CuSe phase is polycrystalline. The cross-sectional SEM image in Figure 3.1 (b) also shows that no grain structure is observed in the bottom InSe layer, while the top CuSe layer has a large-grain structure. The composition of the films was measured using the inductively coupled plasma technique.

3.2.2 Time-resolved High Temperature X-ray Diffraction

Time-resolved high-temperature X-ray diffraction data were collected while the precursor InSe/CuSe bilayers were isothermally heated in stagnant air. The experimental temperatures used ranged from 220 to 270 °C. Initially, the samples were mounted on a platinum strip heater, and XRD data was collected at room temperature. Then the samples were heated at rate of 120 °C /min until the temperature reached a point 20 or 30 °C below the desired target temperature. At this point the temperature was allowed to

stabilize, and then the system was again heated again at 120 °C /min until the target temperature was reached. XRD data was collected for a period of time, typically an hour, at the target temperature. Then all substrates were subjected to a final isothermal temperature treatment at 340 °C for 30 minutes in order to ensure the completion of all reactions (*i.e.*, accomplish a total conversion of the reactants into the final product phase). XRD data was also collected during this last isothermal treatment.

The high-temperature X-ray diffractometer used consisted of a Scintag PAD X vertical θ/θ goniometer, a Buehler HDK 2.3 furnace, and an mBraun linear position sensitive detector (LPSD). The LPSD was centered at 28° 20 and covered a 10° range, *i.e.*, from 23° to 33°. In contrast to conventional X-ray point scanning detectors that perform the scanning step-by-step from lower to higher angles, the LPSD collects the XRD data simultaneously over the 10° window, dramatically shortening the data collection time. This permits *in-situ* time-resolved studies of phase transformations, crystallization, and grain growth. The collection time for the 10° 20 window was set to be either 19.5 or 34.5 seconds, depending on the temperature range. Figure 3.2 displays the time-resolved XRD data collected for a sample isothermally heated at 218 °C. To obtain the fractional reaction (α), the areas for the CuSe (006) peak and the CuInSe₂ (112) peak were estimated from the diffraction data using the JADE software. The values were normalized assuming that the reactants are completely transformed to crystalline CuInSe₂ after each run, and that the texture of the CuInSe₂ does not appreciably change through the entire heating process. Figure 3.3 displays the fractional reaction as a function of time for all the temperatures considered.

Non-isothermal heating was used to investigate the phase evolution of the samples, as follows. The InSe/CuSe samples were heated to several target temperatures. The samples were held at isothermal conditions for 15 minutes, and sequential longer-range (20-55° 20) high-temperature X-ray diffraction scans were collected every 85 seconds. After 15 minutes, the temperature was raised to the next target value, and the process was repeated. The longer-range high-temperature X-ray diffraction scans were used to trace all the intermediate phases and their transformations, and they were realized by combining high-temperature X-ray diffraction data from four discrete LPSD positions.

3.2.3 Calibration for Absolute Temperature of Samples

Since the thermocouple used to measure the temperature was welded to the bottom of the strip heater, a temperature calibration procedure was required to estimate the actual film temperature. Accurate measurements of the thin film temperatures were achieved by calibrating to the known thermal expansion of silver, chosen due to its high coefficient of expansion ($19.5 \times 10^{-6} /K$) (Brand 1955). A fine silver powder was carefully dispersed on the surface of a 0.4 mm glass substrate, and was then annealed at a temperature well above the range of the experimental conditions to make a solid thermal contact and minimize any undesired thermal effects during the calibration runs. For each run, a control program was set to heat the samples at 60 °C/min to the target temperatures, and followed by a hold period until the thermocouple reading became constant. The position of the silver (331) peak was measured from room temperature to 440 °C (thermocouple reading) and used to calculate the lattice parameter $L(T)$ from the expression

$$L(T) = d_{hkl} \sqrt{h^2 + l^2 + k^2} \quad (3.1)$$

where $h=3$, $k=3$, and $l=1$, and d_{hkl} is the spacing between atomic planes inferred from the peak position.

The thermal expansion ratio was taken from the correlation reported by Touloukian *et al.* (Touloukian 1977)

$$\frac{L(T) - L_0}{L_0} = -0.515 + 1.647 \times 10^{-3}T + 3.739 \times 10^{-7}T^2 + 6.283 \times 10^{-11}T^3 \quad (3.2)$$

where L_0 is the lattice parameters of specimen at $T_0 = 293$ K, and T is measured in degrees Kelvin. The correlation is valid in the temperature range $200 \text{ K} < T < 1200 \text{ K}$.

Substituting (3.1) into (3.2) yields

$$\frac{d_{hkl} \sqrt{h^2 + l^2 + k^2} - L_0}{L_0} = -0.515 + 1.647 \times 10^{-3}T + 3.739 \times 10^{-7}T^2 + 6.283 \times 10^{-11}T^3 \quad (3.3)$$

The left-hand side of (3.3) contains known quantities. The resulting cubic equation (3.3) can be directly solved for the unknown value T , which represents the surface temperature of the film. Table 3.1 displays the deviation between the thermocouple reading and the temperature of the specimen estimated by the thermal expansion method. The difference between the thermocouple reading and corrected temperatures reported in Table 3.1 ranges from 52~59 °C, and this difference can be most likely attributed to the low thermal conductivity of the glass substrate. The calibration experiments were replicated, and the results were reproducible within ± 2 °C.

3.3 Results and Discussion

3.3.1 Reaction Kinetics of CuInSe₂ Growth from InSe/CuSe Bilayer

According to the room temperature XRD analysis, the top CuSe layer is a homogeneous crystalline phase with an atomic ratio 1:1, and the bottom InSe layer is

either an amorphous or a nanocrystalline phase with an atomic ratio 1:1.05. The expected interfacial reaction is



Time-resolved high-temperature X-ray diffraction scans showed that the transformations produce a crystalline CuInSe_2 phase product, as expected from reaction (3.4), and that there is no evidence of other intermediate phases.

It is well known that in multilayer thin film systems, the product layer grown at the initial interface of the reactants acts as a nucleation barrier as well as a diffusion barrier. The nucleation barrier often forces a meta-stable amorphous phase to form prior to any crystalline phase (Ma 1991, Johnson 1986). Amorphous and crystalline phases may grow simultaneously during subsequent reaction (Clevenger 1990). Additional heating may cause a further transformation of the amorphous phase to crystalline phase and may also induce additional nucleation reactions.

Analysis on the changes in time of the XRD peaks shows that both the product phase (CuInSe_2) formation and crystalline reactant-phase (CuSe) consumption follow the same deceleratory reaction trend (Figure 3.3 and 3.4), which can be attributed to diffusion-controlled reaction kinetics. Figure 3.5 demonstrates that the sum of the mole fractions of the CuSe reactant and of the product quickly falls below unity during the early stage of the isothermal heating process, because the rate of the CuSe consumption is faster than that of the CuInSe_2 formation. This implies that there is an intermediate phase present before the final product is fully formed. As the long-range high-temperature X-ray diffraction scans showed no evidence of intermediate crystalline phases, the hidden intermediate phase is most likely amorphous CuInSe_2 . Under this perspective, during the

initial stage of the heating process the sum of the mole fractions falls significantly below unity, an effect that can be explained by the formation of the amorphous CuInSe₂ phase, which is initially prevented from evolving into a crystalline phase due to the nucleation-barrier effect. As the heating energy progressively overcomes the nucleation barrier, the CuInSe₂ material also progressively crystallizes, and the sum of mole fractions starts to rise towards unity. The combined amorphous and crystalline CuInSe₂ interfacial layer also acts as a diffusion barrier, opposing the one-dimensional diffusion of the reactants shown on the left-hand side of reaction (3.4). In summary, the InSe|CuInSe₂|CuSe structure introduces both a nucleation and a diffusion barrier. As the isothermal heating continues further, the sum of the mole fractions now rapidly increases towards to unity (Figure 3.5). This indicates that the amorphous phase fully transforms into a crystalline phase. The XRD data of Figure 3.5 shows that for all cases the amorphous phase is completely consumed during the final heating step at 340°. Another plausible explanation for the mole sum to be lower than unity is that the CuSe phase becomes a solid-solution before the crystalline CuInSe₂ phase forms. Further study, perhaps including detailed microscopic analysis, will be needed to better understand the initial stage of the growth mechanism.

The analysis proposed above is consistent with the prevailing perspectives on the growth mechanism documented in the literature. It has been claimed that during the initial steps of solid-solid reaction, the formation of product is rapidly accomplished on the attainment of reaction temperature (Bamford 1980). The initial nucleation reactions at the original interface of the bilayer structure may occur even before the temperature reaches the target values likely via a fast two-dimensional growth mode, rapidly evolving

to impingement. This gives rise to a nucleation barrier that would dramatically reduce the nucleation rate, so that the nucleation reaction is expected to be rapidly deceleratory.

The growth of the CuInSe₂ phase is governed by the planar nature of the precursor film structure. During the early stage of the reaction, heterogeneous nucleation and fast saturation is expected to occur at the original interface. The in-plane material transport is likely to be sustained by rapid interface diffusion, so that at the initial instants the growth at the original interface plane may not be limited by diffusion. The nucleated CuInSe₂ phase grows and coalesces into a continuous layer. After the initial transient stage, the product layer thickens by a diffusion-limited process that is likely to be one-dimensional and perpendicular to the original interface (Ma 1991, Clevenger 1990). The subsequent growth of the product phase, the main reaction stage, is now controlled by the diffusion of one or more species through the product layer.

The kinetics of the growth reactions in terms of activation energy and reaction order have been investigated using two solid-state reaction models, namely, an Avrami model and a parabolic rate model. Avrami analysis is a widely used method for the preliminary identification of the growth rate law. It has been shown that the method yields satisfactory fits to relevant experimental data (Bamford 1980). The transformation kinetics under isothermal heating is described by

$$\alpha = 1 - \exp(-(kt)^n) \quad (3.5)$$

or equivalently, by

$$\ln(-\ln(1-\alpha)) = n \ln t + n \ln k \quad (3.6)$$

where the fractional reaction α represents the volume fraction transformed, k is kinetic rate constant, and n is the Avrami exponent. This analysis has been advocated by Hulbert

(Hulbert 1969), who showed that the Avrami exponent can vary between 0.5 and 1.5 in the case of one-dimensional diffusion-controlled reactions. The value of n is close to 0.5 if the nucleation is instantaneous, and close to 1.5 if the nucleation rate is constant throughout the reaction. It is well known that thickening of thin planar structures after complete edge impingement is realized through one-dimensional growth mode (Christian 1975).

Figure 3.6 displays the Avrami plots for the isothermal heating of the precursor films at different temperatures. Data were taken only for $0.1 < \alpha < 0.95$ to minimize the experimental error. Clearly, the data are fit well by the Avrami model (3.6). Table 3.2 shows the kinetic rate constant and Avrami exponent estimated from the plot. The value of the Avrami exponent is between 0.5 and 0.8, and consistently increases with temperature. This indicates that the growth mechanism is through one-dimensional thickening of the product layer, and that it is also diffusion-controlled. The increase of the n value with temperature is believed to be caused by the enhancement of the nucleation processes with temperature. Higher temperature conditions can overcome the nucleation barrier, so that the nucleation rate during the subsequent growth of the product phase increases with temperature. The temperature effect on the Avrami exponent has been previously reported via simulation studies (Pascual 1996).

The Avrami parameters and the Arrhenius equation

$$k = A \exp\left(-E_a/RT\right) \quad (3.7)$$

were used to estimate the apparent activation energy E_a for the CuInSe_2 formation reaction from the bilayer precursor films. Figure 3.7 shows the high linearity of the

logarithmic Arrhenius plot for $\ln k$. The slope of the line yields the estimate $E_a = 66.0$ kJ/mol.

A second study was performed based on a diffusion-controlled rate law. The simple parabolic kinetic model

$$\alpha = (kt)^{\frac{1}{2}} \quad (3.8)$$

describes well a process where the interface area is constant and the diminution of reaction rate is a consequence of increasing thickness of the diffusion barrier. The above equation can be written in the equivalent logarithmic form

$$\ln \alpha = \frac{1}{2} \ln t + \frac{1}{2} \ln k \quad (3.9)$$

This expression (3.9) has been shown to be obeyed by one-dimensional diffusion process, such as oxidation of metals, where the reactant is in the form of a thin sheet. Figure 3.8 shows the plot of $\ln \alpha$ vs. $\ln t$ for the same XRD data used in the Avrami analysis. Table 3.3 gives the slope of each curve and the resulting kinetic rate constants extracted from the slopes of the plot. The slope is approximately equal to 0.5 for all the runs throughout most of the reaction period, which strongly indicates that the reaction is one-dimensional diffusion controlled. This result is consistent with the conclusions drawn from the Avrami analysis. The Arrhenius equation and the parabolic law parameters were used to produce another estimate of the apparent activation energy (Figure 3.9). The result yielded the apparent activation energy $E_a = 65.2$ kJ/mol, which is consistent with the value $E_a = 66.0$ kJ/mol obtained from the Avrami analysis. Hence, the results from two different analyses are consistent and lead to an identical conclusion, namely that the reaction is one-dimensional diffusion controlled.

3.3.2 Engineering of Reaction Pathways

As described above, non-isothermal heating was used to investigate phase evolution and reaction pathways of the samples as follows. Different precursor samples, InSe/CuSe, and InSe/Cu:Se, were heated to several set points. The top layer of the second sample, Cu:Se means mixture of elemental copper and indium that was prepared depositing copper and indium simultaneously at room temperature. At each set point, the samples were held for 15 minutes during which sequential longer-range (20-55° 2theta) HTXRD scans were collected every 85 seconds. After 15 minutes, the temperature was raised to the next set point at a ramp rate of 60 °C/min, and the process was repeated. The longer-range XRD scan was selected to trace all the intermediate phases and their transformations, and was accomplished by combining HTXRD data from four discrete LPSD positions. It was observed that the precursor films go through different reaction pathways depending on the precursor film structure. This indicates that the reaction pathway can be controlled designing the precursor film structure.

Figure 3.10 displays the high temperature X-ray diffractions for InSe/CuSe precursor films heated under vacuum conditions. It depicts well the phase evolution with time through the reaction. The CuInSe₂ phase forms directly from the reactants and no intermediate phase is detected. During the entire reaction, CuInSe₂ is the only crystalline phase to form according to the HTXRD data. The apparent reaction pathway is CuSe + InSe → CuInSe₂. With an identical heating process under air and helium atmosphere, the reaction was not completed at the end of the run while the reactants were completely transformed to CuInSe₂ phase under vacuum well before the run ends. Higher pressure conditions seems to slow down the reaction. It was previously reported that the low

pressure leaded to completion of the reaction at lower temperature (Lakshmikumar 1995, Lakshmikumar 1996), which is consistent with our result. Further study is needed to understand the mechanism.

Another precursor film, InSe/Cu:Se, went through different reaction pathway. The top layer of this precursor film consists of elemental copper and selenium instead of a binary phase. Figure 3.11 demonstrates that Cu_7Se_4 phase forms first from the top layer. It is then transformed to CuSe phase. Main reaction of CuInSe_2 formation begins after CuSe phase forms probably because temperature did not reach high enough to trigger the CuInSe_2 formation until that point. It appears that formation Cu_7Se_4 and CuSe are sensitively affected by temperature conditions. These results demonstrate that the reaction pathway can be engineered using various precursor film structures. The precursor film structure and the process parameters can be optimized through the HYXRD study.

3.4 Conclusions

Time-resolved high temperature X-ray diffraction analysis has been successfully employed to conduct quantitative analyses of the reaction kinetics of the CuInSe_2 phase formation from bilayer InSe/CuSe precursor films. Transformation from the precursor films into the final phase was clearly observed by *in-situ* X-ray diffraction scanning during isothermal heating. The analysis results based on the Avrami and the parabolic rate law models support the conclusion that the reaction mode is one-dimensional diffusion controlled. The estimated apparent activation energies from these analyses are 66.0 kJ/mol, and 65.2 kJ/mol, respectively.

Careful analysis of XRD data showed that there was a non-crystalline intermediate phase, most likely amorphous CuInSe_2 , during the initial stage of the isothermal heating

process. The combined amorphous and crystalline CuInSe₂ interfacial layer functions as a diffusion barrier as well as a nucleation barrier. Further research should perhaps focus on resolving the exact nature of the non-crystalline intermediate phases, so that a more fundamental understanding of the initial growth kinetics can be achieved.

The reaction pathway for CuInSe₂ formation could be altered using various precursor film structures, which was confirmed using the high temperature XRD. These results demonstrate that the time-resolved high temperature X-ray diffraction provides a powerful method for studying the reaction kinetics of CuInSe₂ growth from the precursor films.

Table 3.1 Thermocouple reading and corrected temperature of the specimen measured by the thermal expansion method.

Thermocouple reading (°C)	Absolute temperature of the specimen (°C)		
	Air	Vacuum	He
270	218	218	211
290	236	234	227
310	253	251	244
330	271	268	261

Table 3.2 Estimated rate constants and Avrami exponents for CuInSe₂ formation from bilayer precursor films.

Temperature (°C)	k (s ⁻¹)	Avrami exponent (n)
218	0.000298	0.573
236	0.000562	0.649
253	0.000945	0.722
271	0.00148	0.760

Table 3.3 Estimated rate constants and the exponents based on the parabolic rate law for CuInSe₂ formation from bilayer precursor films.

Temperature (°C)	k (s ⁻¹)	Exponent (n)
218	0.000116	0.446
236	0.000190	0.450
253	0.000347	0.502
271	0.00539	0.514

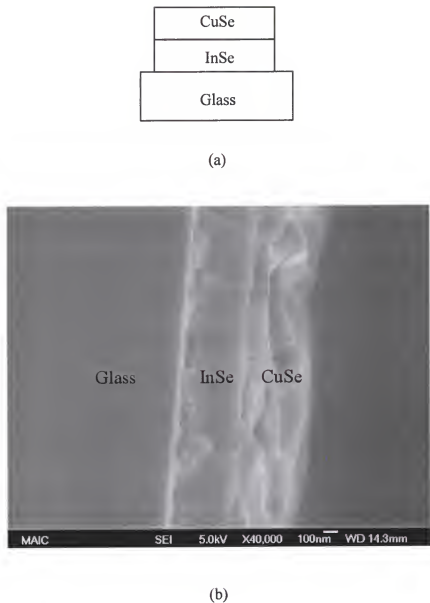


Figure 3.1 Structure of the precursor film, InSe/CuSe: (a) schematic drawing of the precursor film structures, (b) cross-sectional SEM image of the precursor film ($\times 40,000$).

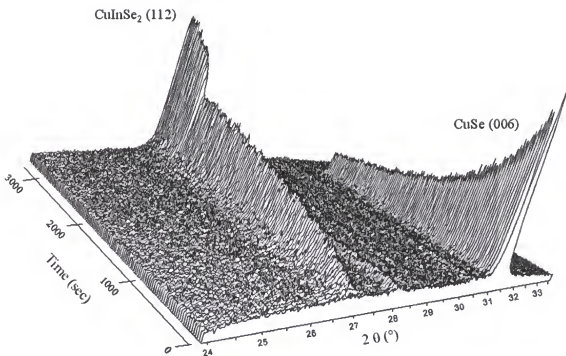


Figure 3.2 Time-resolved *in-situ* X-ray Diffraction for isothermal heating at 218 °C. The last 20 data were collected while heating at 340 °C for 30 minutes.

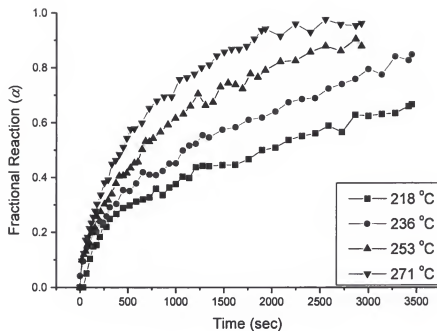


Figure 3.3 Fractional reaction of CuInSe₂ formation during the isothermal runs as a function of time and temperature.

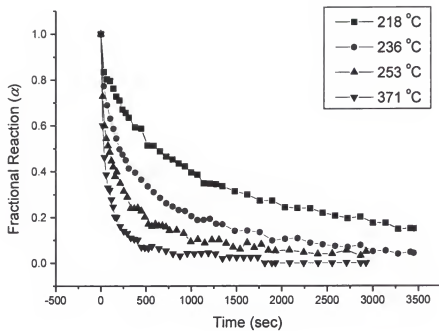


Figure 3.4 Fractional reaction of CuSe transformation during the isothermal runs as a function of time and temperature.

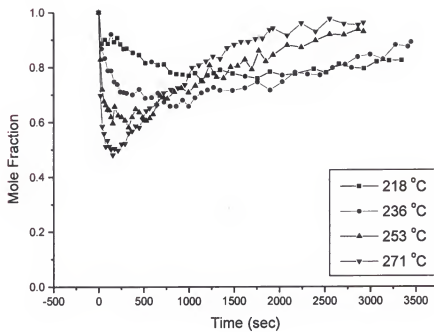


Figure 3.5 Sum of the mole fractions of the reactant (CuSe) and the product (CuInSe_2) through isothermal heating.

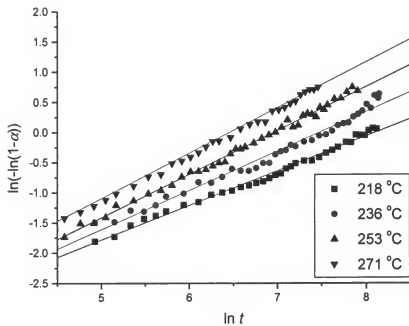


Figure 3.6 Avrami plots for the isothermal reactions at different temperatures.

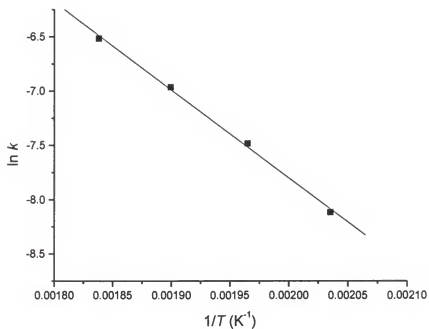


Figure 3.7 Arrhenius plot for the isothermal reactions based on the Avrami analysis: apparent activation energy for CuInSe_2 growth reaction, $E_a = 66.0 \text{ kJ/mol}$.

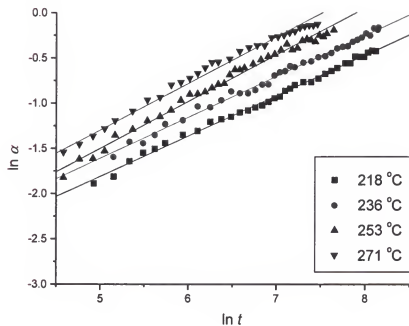


Figure 3.8 Plots based on the parabolic rate law for the isothermal reactions at different temperatures.

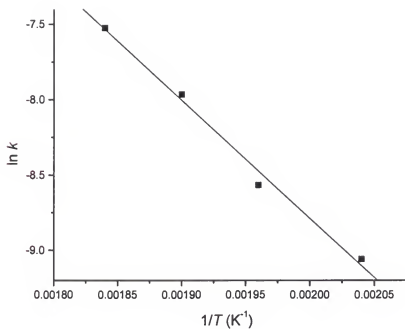


Figure 3.9 Arrhenius plot for the isothermal reactions based on the parabolic rate law: apparent activation energy for CuInSe_2 growth reaction, $E_a = 65.2 \text{ kJ/mol}$.

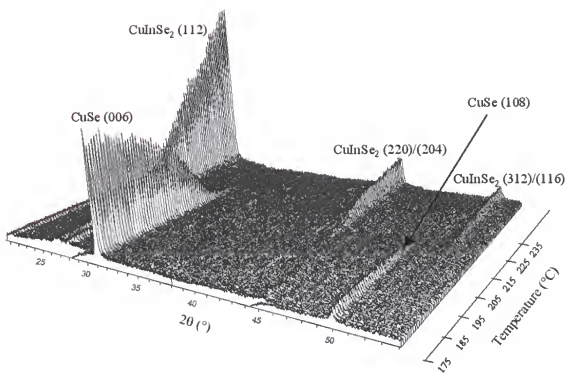


Figure 3.10 Time-resolved *in-situ* X-ray Diffraction with increasing temperature: transformation from a-InSe/CuSe to CuInSe₂.

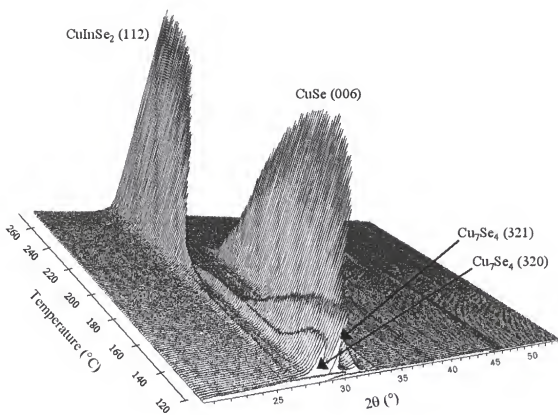


Figure 3.11 Time-resolved *in-situ* X-ray Diffraction with increasing temperature: transformation from a-InSe/Cu:Se to CuInSe₂.

CHAPTER 4
SECONDARY GRAIN GROWTH OF CUNSE₂ IN THE PRESENCE OF CU_XSE
DRIVEN BY INTERFACIAL FORCES

4.1 Introduction

It is well known that the secondary phase, copper selenide, plays an important role in grain growth of CIS-based materials (Rockett 1994, Klenk 1993). The existence of copper selenide during CIS film growth is connected to increases in the grain size and improvements in the electrical properties of the film. Some researchers hypothesized that the secondary phase exists as a liquid-like phase during the process and enhance transport of the reactants from vapor phase into the surface of growing CIS phase (Klenk 1993, Tuttle 1995). This is often called vapor-liquid-solid (V-L-S) growth model, and it emphasizes the kinetic factor during film growth. The kinetic growth models seem to explain acceptably the dramatic grain size change related with composition range, however, there has not been any direct evidence that the kinetic factor is the only driving force for grain growth. Furthermore, the kinetic growth models are valid only when there is supply of reactants from vapor phase.

For other thin film systems, it is well established that the driving force for grain growth is often the reduction of the interfacial free energy that accompanies reduction in total grain boundary area (Atkinson 1988, Hillert 1965, Thompson 1985, Srolovitz 1983). It is hence quite plausible to assume that the grain growth mechanism in the CIS-based material is also related to a reduction of interfacial free energy. In particular, the dramatic increase of the grain size in the presence of the copper selenide phase during

growth shows some similarities to the so called, “secondary grain growth” or “abnormal grain growth” phenomenon for other film growth processes (Wong 1986, Palmer 1987, Thompson 1984, Thompson 1988). In this mechanism, the secondary grain growth is induced by the selectivity in driving force provided by surface-energy anisotropy. That is, to minimize the total energy of the system, the grains with the orientations that have minimum surface energy grow and become prevalent by consuming the grains with other orientations that have higher surface energy (Cahn 1970, Thompson 1985).

If the copper selenide phase enhances the surface-energy anisotropy of the CuInSe₂ phase, in other words, if the copper selenide appreciably lowers the interface free energy of a specific orientation, it will lead to large grains with a specific crystallographic texture. The other feature of the secondary grain growth, such as reduction of some orientation phase and development of bimodal grain size distribution, will be observed. In this chapter, it is reported that existence of the copper selenide phase dramatically increases the average grain size of the CuInSe₂ film during an annealing process, and it is suggested that a thermodynamic driving force, surface-energy anisotropy drives the process.

4.2 Kinetic Aspect of Growth Mechanism of CuInSe₂-based Thin Films

4.2.1 Vapor-Liquid-Solid Growth Model for CIS-based Thin Films

The quality of CIS-based thin films strongly depends on the process parameters, especially the metal atomic ratio, [Cu]/[In], and the growth temperature. Many research groups have incorporated the Cu-rich growth steps to produce larger grain size. It is well known that the surface of even slightly Cu-rich CIS thin film is covered with Cu_xSe phase (Rockett 1994, Niemi 1990, Tuttle 1991). Many researchers suggested that a copper selenide phase, Cu_xSe, exists as liquid phase during a high temperature growth

process, and it enhances the grain growth due to its superior transport mechanism (Birkmire 2001, Nadenau 1995). There has not been, however, any direct proof for the existence of the liquid phase during the growth process.

Droplet structures have been reproducibly observed (Figure 4.1) on the surface of as-grown Cu-rich CIS thin films when certain conditions are fulfilled, namely Cu-rich composition during growth stage and sufficient Se flux during the growth and cooling stages. Other features of the as-grown samples and the process strongly suggest that the droplet structure is closely related to the Cu_xSe liquid phase. The droplet structure seems to be significantly affected by the substrate type, temperature, final thickness of the film as well as the composition. This study should help to better understand the fundamental growth mechanism of CIS-based thin films.

It is well known that growing thin films with different stoichiometries ($[\text{Cu}]/[\text{In}] > 1$ and < 1) grow by entirely different mechanisms and result in distinguished crystalline structure from each other. Klenk *et al.* (Klenk 1993) proposed a model for the characteristic growth mechanism, ‘vapor-liquid-solid model’. It explains the role of the secondary copper-chalcogenide phases in CIS-based thin-film growth, and several researchers refined the model (Tuttle 1991, Tuttle 1995).

It has been shown that some properties of Cu-III-VI₂ materials undergo a sudden change as soon as even a small amount of excess copper ($[\text{Cu}]/[\text{III}] > 1$) is present in the film. Early in the development of CIS photovoltaic device, the so-called ‘Boeing recipe’ was employed to grow CIS thin films with large grain size. The process was first growing Cu-rich thin film and turning it into an overall Cu-poor thin film by reducing the $[\text{Cu}]/[\text{In}]$ during latter part of the process. The enhanced grain size was attributed to the

superior grain growth mechanism of the bottom layer, Cu-rich CIS. As-grown Cu-rich thin films showed much larger grain size (2 to 10 μm) than that of as-grown Cu-poor samples ($<1 \mu\text{m}$) (Tuttle 1994, Klenk 1993). The shape of the grains also changed depending on the composition ratio. The grain structure of Cu-rich samples was more round-shaped while that of Cu-poor samples is very faceted. This anisotropy, attributed to limitations in chalcogen supply, is not observed in Cu-rich films. It suggests that the Cu-rich and the In-rich films go through entirely different growth mechanism. Many researchers believe that the growth mechanism of the CIS thin films is strongly affected by the presence of the secondary phase, Cu_xSe .

The primary assumptions of the V-L-S model are: (1) the presence of liquid phase on the surface during growth, and (2) the grain growth is enhanced by the liquid phase to give superior transport. According to the phase diagram of the Cu-In-Se ternary system, the existence of a liquid phase of Cu_xSe is possible and very likely at high temperature ($\geq 530^\circ\text{C}$) (Nadenau 1995), although it is realized that the growth process is not at equilibrium. This reasoning coincides with several experimental results that display high crystalline structure and large grain size above this high temperature (Tuttle 1995, Stolt 1993). The absorber layers of the best efficiency solar cells have been grown at these conditions.

It is also well known that Cu_xSe phase exists primarily at grain boundaries and surface; hence, it is plausible that vapor, liquid, and solid phases coexist, and the ternary chalcopyrite grains grow by way of the vapor-liquid-solid growth mechanism. Figure 4.2 depicts schematic structure of a growing Cu-rich CIS thin film in view of the V-L-S growth model. The solid bottom layer phase is a growing CuInSe_2 . The vapor species

impinge and condense on the surface of the binary liquid phase. They are then transported to the liquid/solid interface and incorporated in the film. The excess Cu and Se remain in the liquid phase, so the solid ternary phase will be nearly stoichiometric CuInSe₂. If the vapor is deficient in Cu, then the Cu-Se phase will be consumed to form the solid ternary phase, and its amount is reduced. If the Cu deficiency in the vapor phase is maintained, the liquid Cu_xSe phase will finally disappear, and an In-rich surface is formed (Ramanathan 1993). It is believed that the key role of the liquid phase is to enhance transport of the adsorbed species into the growing surfaces.

Tuttle *et al.* (Tuttle 1995) proposed that a growing CIS thin film goes through two different phase segregations in sequence depending on the thickness of the film. According to their model, phase separation between Cu_xSe(l) and CuInSe₂(s) phases exists lateral to the growth plane during initial stage of the growth process. The liquid secondary phase enhances mobility of the adatom on surface and mass transport of the adsorbed species, which result in enhanced grain growth. As the CuInSe₂ solid coalesces, the surface energy between the liquid and the solid phases increases and reaches a critical value, at which time the phase separation converts to an orientation normal to the growth plane. This mechanism reflects the result and reasoning of Adams (Adams 1992) applied for phase separation of Al-Ge thin films during co-deposition. The result clearly shows that Al-Ge phase separation was lateral and transformed to transverse as the film grows. This phenomena can be explained in view of relative thermodynamic stability of the co-existing phases in the thin film structure. Tuttle *et al.* also proposed that the presence of a liquid phase is possible even at low temperature condition (< melting point of CuSe; 523°C). It has been observed in other thin film material systems (Givargizov 1991). The

thermodynamic driving forces and rates on surface of thin films are quite different from those of bulk material. As a rule of thumb, thin films can be condensed in the liquid state above temperature of approximately $2/3 T_m$ (the melting point of the bulk material) (Givargizov 1991). These results support the hypothesis that the presence of liquid phase at the surface region is quite plausible during CIS thin film growth at even less than 523°C . Another research group also proposed the possibility of the liquid phase at low temperature condition (Nadenau 1995).

Although experimental results and theoretical evidence exists for the presence of a secondary liquid phase during growth process, there has not been any direct proof that the liquid phase actually exists and enhances grain growth mechanism. Recently, a unique film surface morphology was observed in the CIS films deposited by MEE. It may provide a more direct evidence for the presence of liquid phase during film growth. The result, however, are likely to be attributed to the unique feature of MEE growth system.

4.2.2 Experimental Evidence of the Liquid Phase during Growth Process

In this work, a unique experimental result was obtained. It may be related to the vapor-liquid-solid growth mechanism. To the best of our knowledge, no such result has been reported to date. It may be a strong and direct evidence of the V-L-S growth model according to what the analysis results indicate.

Cu-rich CIS thin films were grown at various temperature and elemental flux ratios. A reproducible surface morphology is obtained when both conditions of Cu-rich metal flux and sufficient selenium flux are supplied to the growth of CIS films. Droplet-shaped islands formed on the surface of Cu-rich CIS thin films (Figure 4.2). According to the AES and EDS composition measurements, the islands (droplet region) have different composition than the rest of the region (matrix region). The composition of the droplet

region is much more Cu-rich than that of the plane region. When the overall composition of the film is slightly Cu-rich, it seems that only the droplet region has Cu-rich composition while the matrix region is slightly Cu-poor or almost stoichiometric ($\text{Cu/In} \leq 1$). This suggests that there is a phase segregation lateral to the growth plane during the growth process.

Careful observation by SEM revealed that the grain size of the droplet region is larger than that of the matrix region. It suggests that the superior grain growth mechanism occurred in the droplet region. XRD analysis shows that the thin films with the droplet structures have Cu-rich secondary phase, Cu_xSe . It is very likely that only the droplet region has this secondary Cu_xSe phase since the composition of that region is Cu-rich and the composition of the plane region is slightly Cu-poor. The droplet structure remains even after etching the secondary phase with KCN solution, which means that the larger grains are CuInSe_2 as well as the Cu-rich secondary phase.

It is our hypothesis that the droplet structure is caused by the presence of a liquid phase and its superior grain growth mechanism. The shape of the structure is very similar to that of liquid droplets (Figure 4.2). The Cu-rich composition in the droplet region indicates that the region was covered by a low melting temperature Cu-rich secondary phase. The difference of the grain size between the droplet region and the matrix region becomes larger when an annealing step is introduced at the end of the deposition probably because the annealing step enhances surface migration (Figure 4.3).

The droplet structure did not appear when the selenium composition (the $[\text{Se}]/([\text{Cu}]+[\text{In}]+[\text{Se}])$ ratio) was below 48%, even though the film is very Cu-rich. Cu-Se phase such as Cu_2Se has a very high melting temperature compared to the selenium-

rich eutectic at, 523°C. It is thus possible that a deficiency in selenium prevented formation of the low melting eutectic liquid. The shape of the droplet increasingly resembles that of a liquid droplet as the growth temperature is increased or annealing process is introduced (Figure 4.4).

For the hypothesis described above, however, there are still some questions that need to be answered. Firstly, the growth temperature ($400\pm30^\circ\text{C}$) seems to be too low to sustain a liquid phase. The answer may come from the example of a different material system. Givargizov introduced a result that is somewhat commonly observed in thin film structure (Givargizov 1991). The thermodynamics and kinetics on the surface can be quite different from that of bulk state. It is possible that some species is condensed as a liquid or semi-liquid phase above approximately 2/3 of the melting temperature (K). If it can be applied to CIS thin films, 2/3 of the CuSe melting point, 236°C, is lower than the growth temperature.

Another important question is why the specific result is only found when deposition occurs by MEE system. To answer this question, the unique features of the MEE system need to be understood.

The differences from typical co-deposition systems are discussed in the system description section (Chapter 1). The MEE system adopts a rotating platen that sequentially delivers the metal and the chalcogen elements, therefore, each source impinges on the substrate in an intermittent and periodic fashion. There is also certain time period (load lock zone) that the substrate is not exposed to a flux. The system was designed to enhance the surface migration of species so that a lower growth temperature or potentially better material quality could be achieved.

A liquid in contact with a solid will either completely wet the surface or form a spherical droplet depending on the surface free energies, γ_{SL} , γ_{SV} , and γ_{LV} . It has been observed that the appearance of the droplet surface morphology depends on the substrate used. The structure clearly formed on Mo-coated substrates while it did not appear on bare soda lime glass substrates. A hint about what is occurring can be found from the experiment of Adams on phase segregation during Al-Ge deposition (Adams 1992). The phase segregation is lateral during initial stages of growth, and then becomes transverse as the film continues to grow. It is argued in this work that the transformation occurs to make the system thermodynamically more stable.

4.3 Experiments

The migration enhanced epitaxy (MEE) growth system was used to grow CIS films, and the equipment is discussed in Chapter 1.

Approximately 0.6 μm of CuInSe₂ was grown on molybdenum-coated soda lime glasses in the MEE system. The substrate temperature was 450 °C. The films were grown very slightly Cu-rich ($[\text{Cu}]/[\text{In}] = 1.02$). Thin layer of CuSe (~0.1 μm) was then deposited on the as-grown CIS film at a low temperature (~150 °C) in the MEE system. This temperature is sufficiently low to prevent reaction between CuSe layer and the underlying CIS layer. The final sample structure before the annealing step is glass/Mo/CIS/CuSe as depicted in Figure 4.5. The films with and without the CuSe layer were annealed in the MEE system under the conditions given in Table 4.1. The composition of the films was measured using ICP. The SEM analysis was performed with a JEOL JSM-6335F field emission scanning electron microscope. XRD data were analyzed using the software JADE, a program for powder diffraction data analysis.

4.4 Results and Discussion

Composition of the as-grown CuInSe₂ films was intended to be very slightly copper rich ($[Cu]/[In] = 1.02$) to prevent Cu incorporation into the CuInSe₂ phase leading to additional formation of CuInSe₂ during the annealing step. The phases that exist in CIS strongly depend on the film composition (Klenk 1993, Tuttle 1995, Rockett 1994). When the composition is slightly indium-rich, the phase diagram indicates that the material is single phase, CuInSe₂. The two-phase Cu_xSe-CuInSe₂ boundary lies very close to the $[Cu]/[In] = 1$ composition. Addition of Cu or other element will form CIS within the limit of the single phase region. Two phases, CuInSe₂ and Cu_xSe, co-exist when the film composition is stoichiometric or Cu-rich. It is important to know that the excess copper is not incorporated into the CuInSe₂ phase but consumed to form the secondary phase, copper selenide.

The Cu_xSe phase in the film can be selectively etched by a potassium cyanide (KCN) solution. When the as-grown CuInSe₂ films were treated with 10 % KCN aqueous solution, the film composition changed from slightly Cu-rich ($[Cu]/[In] \sim 1.02$) to slightly indium-rich ($[Cu]/[In] \sim 0.99$: Table 4.2). X-ray diffraction spectra show small peaks of the CuSe phase before the etching, and those peaks disappear after the KCN treatment. The ICP and XRD results indicate that the as grown CIS samples have a small amount of the Cu_xSe phase.

The sample groups with and without the additional copper selenide layer were annealed at the same time in the MEE system. The exact annealing conditions are described in Table 4.1. Selenium flux with source maintained at 250 °C was maintained to prevent selenium loss by evaporation from the samples, which keeps the composition

of both CIS and CuSe constant throughout the annealing process. After the annealing process, both the samples with and without the CuSe layer were treated by the KCN solution to remove the Cu_xSe phase and the composition of the sample was determined by ICP. The results shows that the film composition after annealing and the KCN treatment (sample group C-KCN) is very close to that of the KCN-treated CIS samples that was not annealed (sample group A-KCN). This result indicates that there was not incorporation of any element into the CuInSe_2 phase during the annealing step. As mentioned earlier, it is important to know that the excess copper is not incorporated into the CuInSe_2 (*i.e.*, this phase is saturated with reagent of Cu) but remains in a secondary phase (Cu_xSe). Overpressure of the selenium was maintained during the CuInSe_2 film growth and for selected samples during the annealing process, hence; it can be reasonably assumed that there was not significant addition or loss of selenium during the process. The compositional analyses and the phase diagram strongly suggest that there is negligible or no CIS phase formation through incorporation of new elements during the annealing process. This minimizes the possibility that the grain growth occurred by the mass transport between the CIS and the Cu_xSe phases (*i.e.*, a kinetic effect) during the annealing step.

Figures 4.5 and 4.7 display SEM images of the samples that were annealed with (b) and without (a) the CuSe layer, and with a Se overpressure during annealing. These images clearly show that grain growth results from the annealing in the presence of CuSe layer, compared to annealing process without the CuSe layer. Some of the grains in the samples annealed with the CuSe layer (362-3K and 363-3K) are larger than the film thickness.

Full width at half maximum (FWHM) of the (112) x-ray diffraction peak was measured to better quantify crystallinity and grain size of the samples comparing samples of group C (annealed in the presence of CuSe layer) and group D (annealed without CuSe layer). Table 4.2 shows that the FWHM values decreased by ~ 30% by annealing in the presence of CuSe layer. The samples annealed with the CuSe (sample group C) show remarkably greater peak intensity and smaller FWHM values of (112) peak compared to the sample groups that did not have the CuSe layer during annealing (Table 4.2 and Figure 4.8). These results strongly suggest that existence of the CuSe layer during the annealing process enhanced the (112) oriented grain growth. The XRD result is consistent with the SEM images (Figures 4.6 and 4.7) that show an increase in the grain size.

The samples that did not have the CuSe layer during annealing also shown an increase of the (112) peak area, but much less compared to the samples with the CuSe layer (Figure 4.8). It is likely because those samples without the CuSe layer had small amount of CuSe phase due to the slightly Cu-rich composition of the as-grown CuInSe₂ films. The small amount CuSe phase is likely to cover the film surface in part and exist at the grain boundaries. This hypothesis specifically explains the difference between samples 362 and samples 363. Figure 4.8 clearly shows that 363-4K acquired more increase of the (112) peak area compared to 362-4K. Those two samples did not have the CuSe layer during the annealing process. The only difference is that the samples 363's had overpressure of selenium during the annealing process while the samples 362's did not. It is likely that absence of the selenium supply during the annealing process caused selenium evaporation from the CuSe phase of the samples 362's and resulted in phase

transition from CuSe to the selenium poor Cu_xSe phase. It could reduce the effect of the CuSe phase in the sample 362-4K. The difference in the peak area between the sample 362-3K and the 363-3K is negligible. Both samples had a CuSe layer during annealing.

Figure 4.9 displays the (220)/(204) reflections of CIS samples that were annealed with and without the CuSe layer. Interestingly, it is observed that peak area of the (220)/(204) orientated grains decreased more when the CuSe layer was deposited prior to annealing (Table 4.2 and Figure 4.9). This indicates that large portion of the (220)/(204) oriented grains were consumed to contribute to (112) oriented grain growth. This tendency is clearly demonstrated in Figure 4.10. From the shape of the curves, extent of the increase of the (112) peak area is consistent with the decrease of the (204)/(220) peak area. Specific peak area is proportional to the amount of the corresponding crystalline phase assuming other effects (*e.g.*, stress or strain effects) are the same. This is a strong evidence for secondary grain growth. It is also observed that the FWHM decreases after annealing so that (204) and (220) peaks are split in the samples 362-3K and the 363-3K. Those two peaks could not be clearly distinguished before annealing since they closely overlapped and the crystallinity was poor.

As pointed out earlier, secondary grain growth can be induced by a selectivity in driving force provided through a surface-energy anisotropy. To minimize the total free energy of the system, grains with orientations that minimize the surface energy grow to consume the grains with other orientations (Cahn 1970, Thompson 1985). The surface-energy anisotropy can play a dominant role in determining which grains become secondary grains in thin films. As a result, a specific orientation may grow and

sometimes become dominant while other orientations diminish or disappear. Existence of secondary phase and defect can affect the status of the surface energy anisotropy.

In the chalcopyrite structure material systems such as CuInSe_2 , the (112) plane is likely to have the lowest surface energy for free surfaces (Zhang 2001, Liao 2002). As a result, XRD spectra of CIS films often show that the CIS films are textured along the (112) plane parallel to the substrate. The second strongest peak is usually the (204)/(220). It is possible that presence of the Cu_xSe increases the surface-energy anisotropy by selectively lowering the surface free energy of the (112) orientation phase.

From the XRD results, all the samples annealed with the CuSe layer showed an increase of the (112) orientated phase and a decrease of the (220)/(204) phase compared to the as-grown CuInSe_2 films. The extent of the increase of the (112) peak area is consistent with that of a decrease in the (220)/(204) peak area. The SEM images show that annealing with the CuSe layer increased the grain size of the CIS films. These results are consistent with a secondary grain growth mechanism assisted by the CuSe phase.

It is proposed that the CuSe phase enhances the surface-energy anisotropy of the CuInSe_2 films and consequently induces the secondary grain growth of the (112) orientated phase. This is likely to occur during many other growth processes of the CuInSe_2 -based materials when the overall composition is Cu-rich. The thermodynamic factor (the surface-energy anisotropy) as well as the kinetic factor (mobility enhancement) is believed to be primary driving forces for the enhanced grain growth to result in the large grain size of CuInSe_2 phase.

4.5 Conclusions

The effect of a secondary CuSe phase on the grain growth of CuInSe₂ films was investigated. CuInSe₂ films were deposited onto molybdenum-coated soda lime glass using a molecular beam epitaxy system. The composition of the as-grown CuInSe₂ films were intended to be stoichiometric or slightly Cu-rich. On selected films, thin layer of the CuSe was deposited on the as-grown CuInSe₂ films. These bi-layer samples, CuInSe₂/CuSe, were then annealed at two different temperatures and with and without Se overpressure. The grain size was observed to increase (up to a few μm) in samples annealed with the CuSe layer as compared to samples annealed without the CuSe layer. After annealing the CuInSe₂/CuSe films, the peak area of the (112) reflections increased while that of the (220)/(204) reflections decreased, consistent with (112) oriented grain growth at the expense of the (220)/(204) grains. It is proposed that there is a thermodynamic driving force for the grain size increase, known as "secondary grain growth", assisted by the surface-energy anisotropy.

Table 4.1 Summary annealing conditions

Sample group	Sample number	Structure before annealing	Annealing conditions		KCN treatment	Remarks
			Temperature	Se overpressure		
A	359-8	CuInSe ₂	No annealing		No	As grown CIS, No annealing
A-KCN	359-8K ^a	CuInSe ₂	No annealing		Yes	No annealing, KCN treatment
B	360-2	CuInSe ₂ /CuSe	No annealing		No	Deposition of CuSe layer
B-KCN	360-2K	CuInSe ₂	No annealing		Yes	KCN treatment of group B
C-KCN	362-3K	CuInSe ₂ /CuSe	~450 °C	No	Yes	Annealing with CuSe layer
D-KCN	362-4K	CuInSe ₂	~450 °C	No	Yes	Control sample I
C-KCN	363-3K	CuInSe ₂ /CuSe	~450 °C	Yes	Yes	Annealing with CuSe layer
D-KCN	363-4K	CuInSe ₂	~450 °C	Yes	Yes	Control sample II
C-KCN	364-3K	CuInSe ₂ /CuSe	~370 °C	Yes	Yes	Annealing with CuSe layer

a: K indicates that the sample was treated with KCN to remove Cu_xSe phase.

Table 4.2 Composition (ICP) and X-ray diffraction analysis results

Sample group	Sample number	Atom (%)				FWHM of (112)	Peak area of (112)	Peak area of (204)/(220)
		Cu	In	Se	Cu/In			
A	359-8	25.7	25.1	49.2	1.02	-	-	-
A-KCN	359-8K	25.2	25.5	49.3	0.99	0.134	3.40×10^5	1.36×10^5
B	360-2	28.3	22.5	49.2	1.25	-	-	-
B-KCN	360-2K	25.2	25.4	49.4	0.99	0.130	3.53×10^5	1.40×10^5
C-KCN	362-3K	25.3	25.3	49.4	1.00	0.085	1.01×10^6	4.65×10^4
D-KCN	362-4K	25.3	25.4	49.3	1.00	0.126	4.63×10^5	1.24×10^5
C-KCN	363-3K	25.3	25.5	49.2	0.99	0.084	9.10×10^5	5.77×10^4
D-KCN	363-4K	25.4	25.5	49.1	1.00	0.115	6.80×10^5	9.89×10^4
C-KCN	364-3K	25.2	25.6	49.2	0.98	0.089	1.06×10^6	4.91×10^4

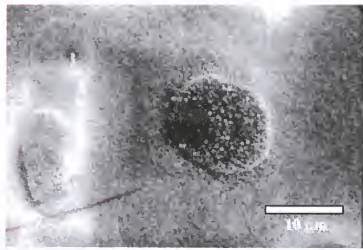


Figure 4.1 Droplet structures on an as-grown Cu-rich CuInSe₂ film: T = 350 °C, [Cu]/[In] = 1.03.

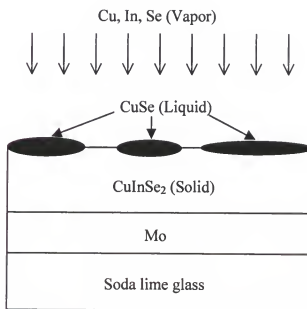


Figure 4.2 Schematic structure of a growing Cu-rich CIS thin film based on the vapor-liquid-solid model.

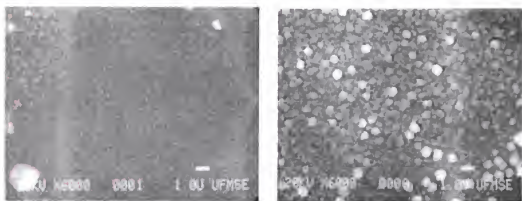


Figure 4.3 SEM images of different regions on the surface showing an apparent difference in grain size in (a) matrix region and (b) droplet region.

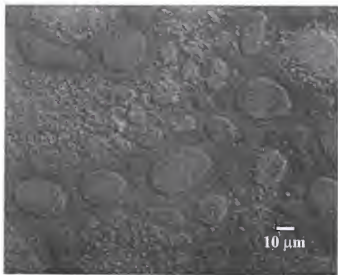


Figure 4.4 Droplet structures on an as-grown Cu-rich CuInSe₂ film with annealing: T = 450 °C, [Cu]/[In] = 1.03.

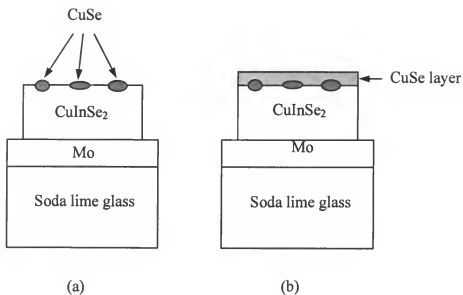
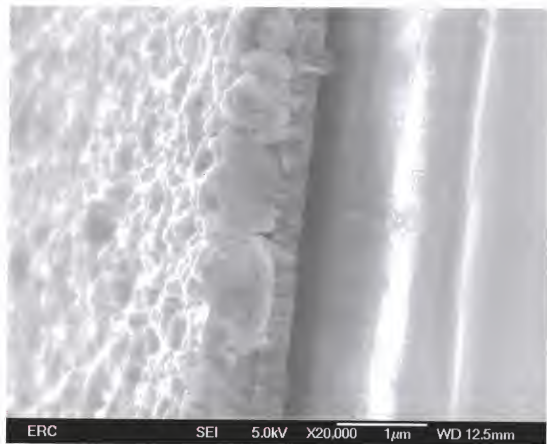


Figure 4.5 Schematics of sample structures: (a) without the CuSe layer; control sample, (b) with the CuSe layer.



(a) Sample 362-4K

Figure 4.6 Cross-sectional SEM images of CuInSe₂ films: (a) annealed without the copper selenide layer on the top of the CuInSe₂ layer.



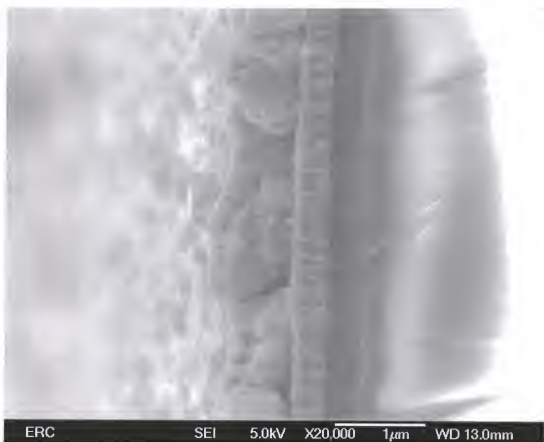
(b) Sample 362-3K

Figure 4.6 Cross-sectional SEM images of the CuInSe₂ films: (b) annealed with the copper selenide layer. Both samples were treated with KCN solution to selectively remove the copper selenide layer after annealing.



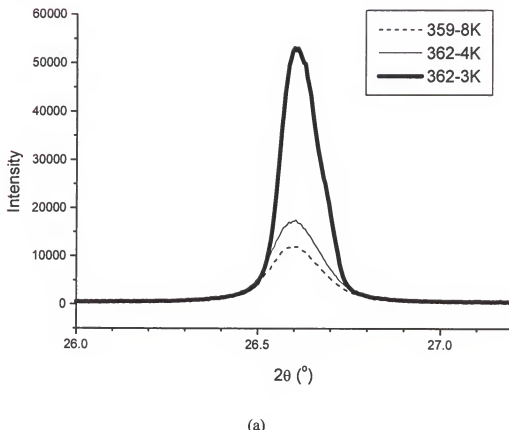
(a) Sample 363-4K

Figure 4.7 Cross-sectional SEM images of CuInSe₂ films: (a) annealed without the copper selenide layer on the top of the CuInSe₂ layer.



(b) Sample 363-3K

Figure 4.7 Cross-sectional SEM images of the CuInSe_2 films: (b) annealed with the copper selenide layer. Both samples were treated with KCN solution to selectively remove the copper selenide layer after annealing.



(a)

Figure 4.8 CIS (112) diffraction peaks: (a) annealed at approximately 450 °C without selenium overpressure. The sample 359-8K was not annealed. The sample 362-3K and 363-3K were annealed with the copper selenide layer, while sample 362-4K and 363-4K were annealed without the copper selenide layer. All the samples were treated by KCN to selectively remove the copper selenide after annealing.

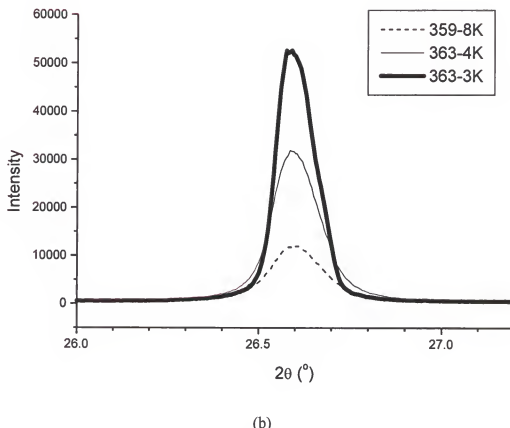
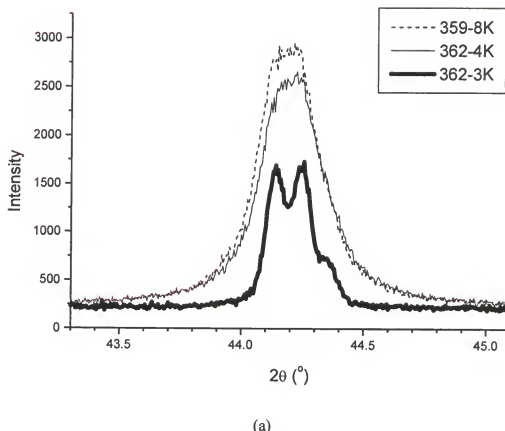


Figure 4.8 CIS (112) diffraction peaks: (b) same temperature condition, but with selenium overpressure. The sample 359-8K was not annealed. The sample 362-3K and 363-3K were annealed with the copper selenide layer, while sample 362-4K and 363-4K were annealed without the copper selenide layer. All the samples were treated by KCN to selectively remove the copper selenide after annealing.



(a)

Figure 4.9 CIS (204)/(220) diffraction peaks: (a) annealed at approximately 450 $^{\circ}$ C without selenium overpressure. The sample 359-8K was not annealed. The sample 362-3K and 363-3K were annealed with the copper selenide layer, while sample 362-4K and 363-4K were annealed without the copper selenide layer. All the samples were treated by KCN to selectively remove the copper selenide after annealing.

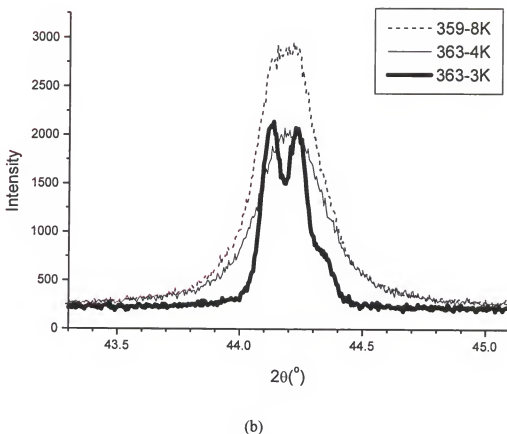
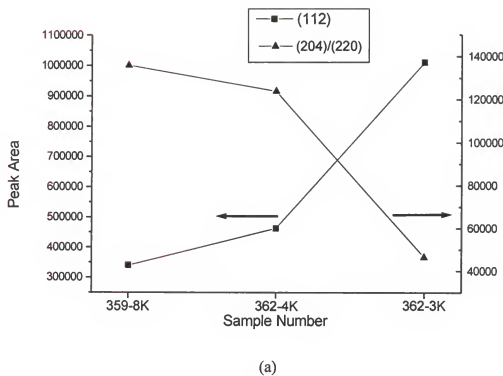
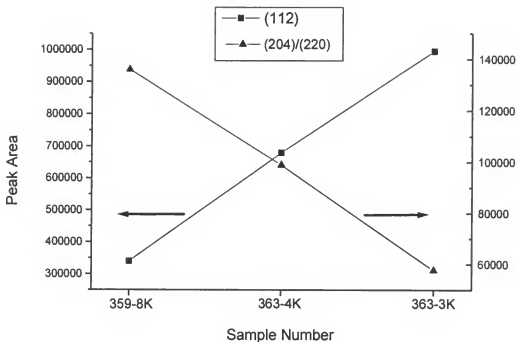


Figure 4.9 CIS (204)/(220) diffraction peaks: (b) same temperature condition, but with selenium overpressure. The sample 359-8K was not annealed. The sample 362-3K and 363-3K were annealed with the copper selenide layer, while sample 362-4K and 363-4K were annealed without the copper selenide layer. All the samples were treated by KCN to selectively remove the copper selenide after annealing.



(a)

Figure 4.10 XRD peak areas: (a) annealed at approximately 450 °C without selenium overpressure. The sample 359-8K was not annealed. The sample 362-3K and 363-3K were annealed with the copper selenide layer, while sample 362-4K and 363-4K were annealed without the copper selenide layer. All the samples were treated by KCN to selectively remove the copper selenide after annealing.



(b)

Figure 4.10 XRD peak areas: (b) same temperature condition, but with selenium overpressure. The sample 359-8K was not annealed. The sample 362-3K and 363-3K were annealed with the copper selenide layer, while sample 362-4K and 363-4K were annealed without the copper selenide layer. All the samples were treated by KCN to selectively remove the copper selenide after annealing.

CHAPTER 5
EPITAXIAL GROWTH OF CUINSE₂ AND CUGASE₂ FILMS ON SINGLE CRYSTALLINE GAAS SUBSTRATE USING A MIGRATION ENHANCED EPITAXY REACTOR

5.1 Introduction

This chapter presents preliminary results on the epitaxial growth of CuInSe₂ (CIS) and CuGaSe₂ (CGS) films. While there have been several studies of the growth mechanism of CuInSe₂ films, it is still not fully understood in part due to complex phase evolution and defect chemistry in that material system. The Cu(In,Ga)Se₂ (CIGS)-based solar cells are known to produce high efficiency when grown by a number of techniques (Devaney 1990, Bodegard 1995, Cahen 1989). The mechanism responsible for the improvements, however, are not fully understood. It has been difficult to produce samples in a completely reproducible way. To accurately identify the effects of process parameters and defect chemistry on the device performance, one must first grow high quality films reproducibly. For example, the inconsistent effect from grain boundaries needs to be eliminated or at least minimized to investigate the relationship between the electrical properties and the process parameters. The best approach of preparing such high quality CIS and CGS films is to grow the films epitaxially on a single crystalline substrate, such as a GaAs wafer.

In addition to the above reasons, the need for single crystalline CIGS-based solar cells are growing due to its potential for a tandem solar cell structure. The concept of the tandem solar cell has been explored during the last decade. The structure consists of double junctions that have different energy band gaps. The single crystalline CGS film is

considered as a suitable candidate for the absorber layer of the top junction, and the single crystalline CIS film is for the bottom junction. The double junction structure will improve the overall energy conversion efficiency over single junction structure solar cells. CGS-based solar cell with its higher band gap (1.68 eV) would be advantageous for module performance because of the reduced current densities (Nadenu 2001). Along with the super-high energy conversion efficiency, the stable and radiation-resistant characteristics of the CIGS-based solar cells is attractive for space applications. The rationale of developing a process for the single crystalline CGS and CIS recently is compelling.

Focus of this dissertation is on growing epitaxial films of CIS and CGS on (001) GaAs wafers. The preliminary results are promising, and are presented in this chapter.

Previous work (Stanbery 1999, Stanbery 2002) showed that the migration enhanced epitaxy (MEE) reactor could be used to grow epitaxial films of the ternary compound CuInSe₂ on (001) GaAs. The films were ordered in a CuAu crystallographic structure rather than more commonly observed equilibrium chalcopyrite structure. The film growth mode was believed to be a 3-D Stranski-Krastanov. Various characterization methods such as XRD, TEM-TED, and Raman scattering were used to support this conclusion. The results of this study are consistent with the previous work and show that the film composition and the growth temperature are the most important factors for determination of the film structure and quality.

5.2 Experiments

The migration enhanced epitaxy (MEE) described in Chapter 1 was used in this study. The substrates were polished semi-insulating GaAs wafers oriented 2° off the (001) plane

toward the nearest [110] axis. The GaAs substrates were etched with a 5:1:1 mixed solution of H_2SO_4 : H_2O_2 : H_2O at room temperature for 2 minutes. De-ionized water and methanol were then used to rinse the etched GaAs substrates. The substrates were immediately put in the load lock after the cleaning step, and the load lock was pumped to 1×10^{-5} Torr by a turbo-molecular pump to minimize oxidation of the cleaned substrates. The substrates were then transferred into the main MEE chamber and placed on substrate holders. The pressure of the main chamber was maintained using a diffusion pump. Heating and rotation of the platen/substrates began at the same time, just after the sample transfer step. When the temperature reached a stable set point, the rotation of the platen stopped to locate the GaAs substrate beneath the radiation heater for annealing. The substrate stays in that position for 10 minutes, which heats the substrate to just over 700 °C. The rotation of the platen is resumed to give a uniform heat distribution through a revolution cycle. According to a thermal model of the MEE system (Chapter 6), maximum temperature change during a cycle is less than 10 °C, and the temperature uniformity within a substrate region is < 5 °C. This result fulfills the temperature uniformity requirement for the substrate region during the deposition process.

The steady-periodic temperature of the substrate during the deposition process was varied during different stages of growth. A multiple temperature growth process was employed to optimize the epitaxial growth conditions (Figure 1). To enhance the initial nucleation reaction, a rather low growth temperature ($\sim 450 \pm 30$ °C) was used for the first ten monolayers of the CIS and CGS films. The temperature was then ramped up to 500 ± 30 °C and maintained at that temperature until the film thickness reaches 50 nm to improve the surface migration of the adsorbed atoms. Finally, the substrate temperature

was lowered to 450 ± 30 °C to grow a meta-stable phase of the film with a low density of dislocation. The growth rate was maintained at a low value, around 0.5 \AA/s , to maximize the surface migration and epitaxial growth. This was also required because of the metal flux limited by Se evaporation as discussed in Chapter 1. Final film thickness is approximately $0.45 \mu\text{m}$. Absolute total flux calibration was employed to set the average Se/(Cu+(In or Ga)) molar flux ratio to an approximate value of 5, of course this ratio varied between 0 and 5 during growth. The rotation rate of the substrate on the platen was set to be 20 rpm or 3 sec/cycle through the entire process. Overall composition of the films was measured using inductively coupled plasma (ICP) technique. Table 5.1 shows exact process conditions.

5.3 Results and Discussion

Previous work of our research group (Stanberry 1999, 2002) reported an epitaxial growth of CuInSe₂ films on (001) GaAs. The film structure exhibited distinct coexisting domains of both a non-equilibrium crystallographic structure characterized by CuAu (CA) cation ordering, and the compound's equilibrium chalcopyrite (CH) structure. The films of the chalcopyrite phase of CuInSe₂ deposited by MEE onto (001)-oriented GaAs substrates were found to continue the (001) orientation of the substrate, consistent with other reports of growth by conventional MBE (Niki 1993). Under certain growth conditions, however, the films were also found to contain domains of the CA-ordered structure. Evidence for this film structure was provided using XRD, TEM-TED, and Raman scattering data. The film growth mode was believed to be a 3-D Stranski-Krastanov. It was also reported that strongly oriented ordering of the island arrays occurs only in the case of nonstoichiometric Cu-rich composition.

Epixially grown films on (001) GaAs from this study shows very consistent features with the previous work. It was observed that Cu-rich CuInSe₂ and CuGaSe₂ samples grown on (001) GaAs have 3-D island arrays that are highly oriented and textured in [110] direction. The SEM and AFM images in Figure 5.2 to 5.6 depict the surface morphology of Cu-rich CuInSe₂ and CuGaSe₂ films grown on (001) GaAs. The same films grown on molybdenum-coated glass (Figure 5.2 (b) and 5.5 (b)) do not show any texture or specific growth direction on its surface. AFM images (Figure 5.4) more clearly show a textured structure of the surface morphology.

It is well known that a Cu-rich composition results in the formation of a secondary phase, Cu_xSe, on the surface of the film and at the grain boundaries. The Cu_xSe plays an important role in grain growth mechanism of the CIGS-based materials (Rockett 1994, Klenk 1993). The existence of copper selenide during the CIS film growth process increases the grain size and consequently improves the electrical properties of the film and the final device (see Chapter 4). Some researchers hypothesized that the Cu_xSe exists as a liquid-like phase at growth temperature and enhances transport of the reactants from vapor phase into the surface of growing CIS phase (Klenk 1993, Tuttle 1995). The existence of the Cu_xSe phase was reported to lead to higher crystalline quality (Niki 2002). Chapter 4 of this dissertation also demonstrates the positive effect of CuSe on grain size and crystalline quality of polycrystalline CuInSe₂ films. It is plausible that the Cu_xSe plays a similar role in epitaxially grown films.

From the previous work, a morphological distinction was found between the Cu-rich and indium-rich samples. The CuInSe₂ samples grown on (001) GaAs exhibited the film + island structure characteristic of Stranski-Krastanov mode growth. The Cu-rich islands

were highly faceted with their longer axis oriented parallel to the ripples that form on the epilayer along the [110] direction. This specific surface morphology of the Cu-rich films was considered a strong indication of textured structure or epitaxial growth of the films. The result of this study shows that the oriented and faceted surface morphology is found from both Cu-rich CuInSe₂ and Cu-rich CuGaSe₂ films grown on (001) GaAs. Figures 5.2, 5.5, and 5.6 clearly show that the islands on the surface are oriented with [110] direction and are highly faceted.

A series of diffraction peaks at $2\theta \approx \{15.45^\circ, 30.93^\circ, 47.19^\circ, 64.17^\circ\}$ were tentatively assigned to the (001), (002), (003), and (004) reflections of the Cu-Au (CA) in structure in the previous study (Stanbery 1999). These peaks have been repeatedly detected on Cu-rich CuInSe₂ films in this study. The sample CIS 350 showed prominent peaks at 31.01° and 64.20° , which are tentatively assigned to (002) and (004) reflections of the CA structure (Figure 5.8). Slightly Cu-rich ($[\text{Cu}]/[\text{In}] \sim 1.1$) samples tend to prominently show the characteristics of the CA structure. In contrast, the indium-rich films do not show any indication of epilayer or textured structure. From XRD study on the indium-rich sample (see Figure 5.7), all the peaks detected are assigned to those of polycrystalline chalcopyrite structure. These results indicate that the $[\text{Cu}]/[\text{In}]$ atomic ratio is an important factor in determining the structure of the films grown on (001) GaAs substrate.

As pointed out above, the Cu-rich CuInSe₂ and CuGaSe₂ films grown on (001) GaAs are characterized with a surface morphology of 3-D Stranski-Krastanov growth mode. A mixture of very uniform background region and faceted islands were observed from the SEM and AFM images. From EPMA results, it was found that there is a compositional

distinction between the islands and the background region of the films. Table 5.2 shows the detailed compositional variation for samples CIS 350 and CGS 353. For as-grown CIS 350 and CGS 353, the atomic ratio $[\text{Cu}]/[\text{III}]$ of the background was almost unity. The $[\text{Cu}]/[\text{In}]$ atomic ratio of the island region was much larger than unity, consistent with a phase segregation during the growth process. The composition of each region was measured again after KCN treatment for the films. KCN solution is known to selectively remove Cu_xSe phase. The composition of the island region dramatically changed to stoichiometric or slightly indium-rich, while the composition of the background region is essentially unchanged. This result obviously indicates that the Cu_xSe segregated at the islands during the growth. SEM images of CIS 350 before and after the KCN treatment (see Figures 5.3 and 5.11) show that the grains at the island deformed and their size became smaller, while no change is observed for the background region. Change in CGS 353 (Figure 5.6 and 5.12) is even more noticeable. Besides the compositional distinction, it is believed that there is a structural difference between the background region and the island region. This was partly revealed from the previous study (Stanberry 1999). Further study is needed to investigate the structural distinction between those different regions and a related mechanisms of epitaxial growth.

A theoretical calculation for the crystallographic structure of the epitaxially grown CuGaSe_2 is being conducted to investigate its film structure and to assign the detected XRD peaks. A more extensive study is being continued to establish detailed process parameters and analysis methods as well as to improve the quality of the epitaxially grown films.

5.4 Conclusions

In this chapter, preliminary results of epitaxial growth of CuInSe₂ and CuGaSe₂ on (001) GaAs substrate are presented. From previous work of our research group, it was possible to grow epitaxial CuInSe₂ films on GaAs (001). Under certain conditions, the crystalline structure of the films was found to be Cu-Au (CA) structure rather than the more commonly observed chalcopyrite (CH) structure for CuInSe₂ phase. In this study, results show that the crystalline structure and quality strongly depends on the film composition (*i.e.*, [Cu]/[III] atomic ratio). X-ray diffraction spectra show that CA peaks are present for the Cu-rich CuInSe₂ films. The Cu-rich films are also characterized with the surface morphology of 3-D Stranski-Krastanov growth mode. A uniform background region co-exists with a faceted island region. SEM and AFM results revealed that the Cu-rich CuInSe₂ films have highly oriented array of islands on their surface and those islands are faceted, and with a textured background region lies with or beneath those islands. This specific surface morphology seems to be an indication of epitaxial growth or textured structure of the films, from both the previous and the new study. It is believed that Cu-rich composition has positive effect on the crystalline structure and quality of the epitaxially grown films. In contrast, indium-rich CuInSe₂ films showed characteristics of polycrystalline structure rather than epitaxial or textured structure. It was found that there is a structural and compositional distinction between the islands and the background region of the Cu-rich films. More extensive study is being performed to establish detailed process parameters and analysis methods as well as to improve the quality of the epitaxially grown films.

Table 5.1 Process conditions for CIS and CGS film growth.

Sample ID	CIS 350	CIS 352	CGS 353	CIS 354	CGS 355	CIS 367
Film	CuInSe ₂	CuInSe ₂	CuGaSe ₂	CuInSe ₂	CuGaSe ₂	CuInSe ₂
Temperature (°C)	⁽¹⁾ 400±30	⁽²⁾ 450±30	450±30	450±30	450±30	⁽²⁾ 450±30
Pressure (Torr)	$\sim 5 \times 10^{-8}$					
Rotation rate	12 rpm					
Rotation direction	⁽³⁾ CCW	CCW	CCW	CCW	CCW	CCW
Growth rate (Å/s)	0.62	0.61	0.45	0.55	0.42	0.45
[Cu]/[III] (ICP)	1.15	1.15	1.29	0.97	1.09	1.09

⁽¹⁾Multiple temperature setting: 400 °C → 450 °C (at 10 monolayers of film) → 400 °C (at 50 nm of CIS or CGS)

⁽²⁾Multiple temperature setting: 450 °C → 500 °C (at 10 monolayers of film) → 450 °C (at 50 nm of CIS or CGS)

⁽³⁾CCW : Counter-clockwise

Table 5.2 Compositional variation of samples CIS 350 and CGS 353 as determined by EPMA.

Before KCN treatment					
	Cu (%)	In (%)	Ga (%)	Se (%)	[Cu]/[III]
CIS 350 Background	24.51	24.36	0	50.13	1.05
CIS 350 Island	44.92	9.88	0	44.79	4.55
CGS 353 Background	22.43	0	25.59	51.98	0.88
CGS 353 Island	57.86	0	1.48	40.65	39.1
After KCN treatment					
	Cu (%)	In (%)	Ga (%)	Se (%)	[Cu]/[III]
CIS 350 Background	25.12	25.14	0	49.73	1.00
CIS 350 Island	24.65	25.27	0	50.08	0.98
CGS 353 Background	20.3	0	27.34	52.36	0.74
CGS 353 Island	25.56	0	23.38	51.06	1.09

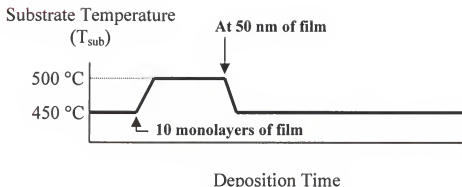
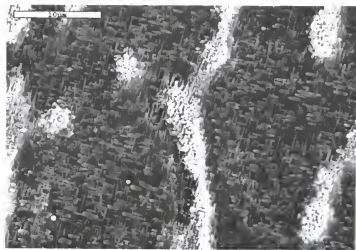
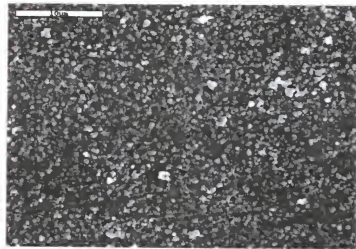


Figure 5.1 Multiple temperature growth schedule: nucleation at a lower T_{sub} , enhanced surface migration using a higher T_{sub} , subsequent growth at a lower T_{sub} to grow metastable phase with low dislocation density.

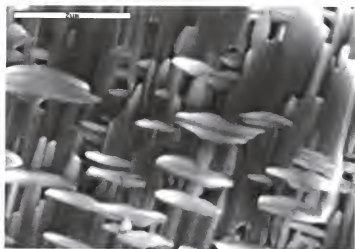


(a)

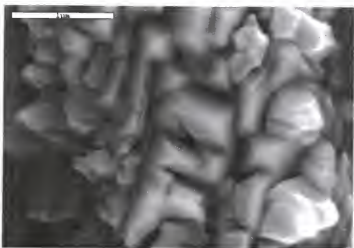


(b)

Figure 5.2 SEM images of CuInSe₂ (CIS 350): atomic ratio, [Cu]/[In] = 1.16, (a) grown on (001) GaAs ($\times 3000$), (b) grown on Mo-coated soda lime glass ($\times 3000$).

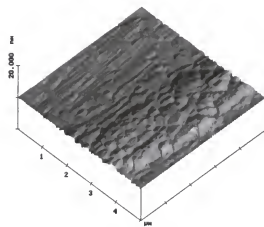


(a)

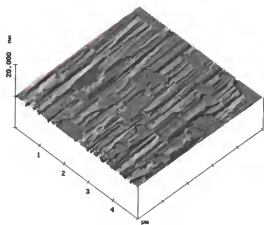


(b)

Figure 5.3 SEM images of CuInSe_2 (CIS 350) grown on (001) GaAs: atomic ratio, $[\text{Cu}]/[\text{In}] = 1.16$, (a) dark background area of Figure 5.2 (a) ($\times 20000$), (b) bright island area of Figure 5.2 (a) ($\times 20000$).



(a)



(b)

Figure 5.4 AFM images of CuInSe_2 (CIS 350) grown on (001) GaAs: atomic ratio, $[\text{Cu}]/[\text{In}] = 1.16$, (a) $10\mu\text{m} \times 10\mu\text{m}$, (b) $5\mu\text{m} \times 5\mu\text{m}$.

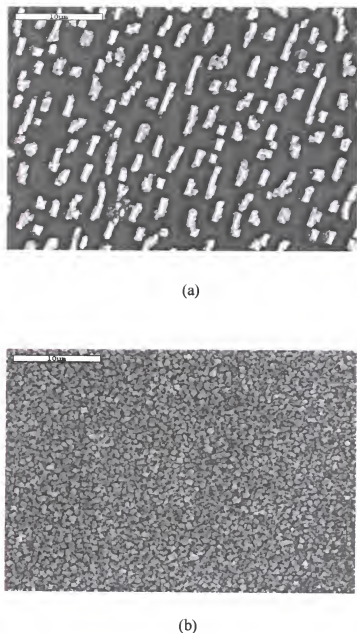
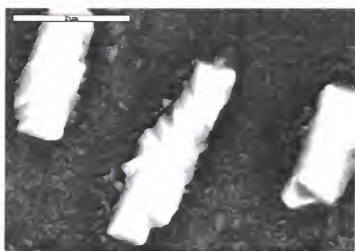
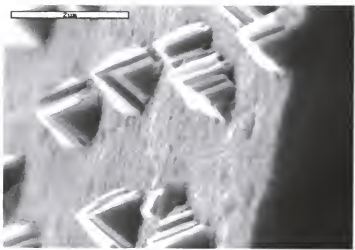


Figure 5.5 SEM images of CuGaSe₂ (CGS 353): atomic ratio, [Cu]/[In] = 1.29, (a) grown on (001) GaAs ($\times 3000$), (b) grown on Mo-coated soda lime glass ($\times 3000$).



(a)



(b)

Figure 5.6 SEM images of CuGaSe₂ (CGS 353) grown on (001) GaAs: atomic ratio, [Cu]/[In] = 1.29, (a) plain view ($\times 20000$), (b) side view ($\times 20000$).

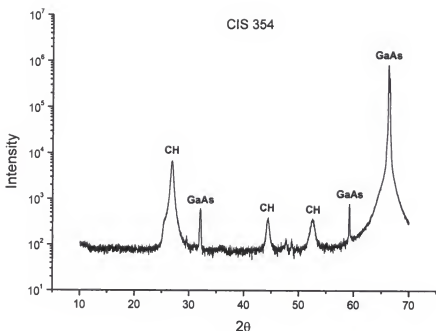


Figure 5.7 XRD θ - 2θ scan diffraction data of CuInSe_2 film (CIS 354) grown on (001) GaAs: atomic ratio, $[\text{Cu}]/[\text{In}] = 0.97$.

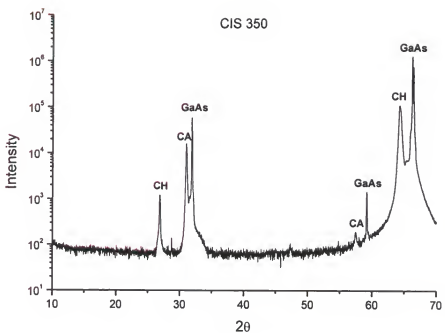


Figure 5.8 XRD $0-2\theta$ scan diffraction data of CuInSe_2 film (CIS 350) grown on (001) GaAs: atomic ratio, $[\text{Cu}]/[\text{In}] = 1.15$.

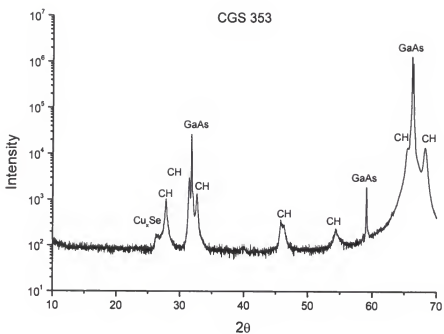


Figure 5.9 XRD $0-2\theta$ scan diffraction data of CuGaSe_2 film (CGS 353) grown on (001) GaAs: atomic ratio, $[\text{Cu}]/[\text{In}] = 1.29$.

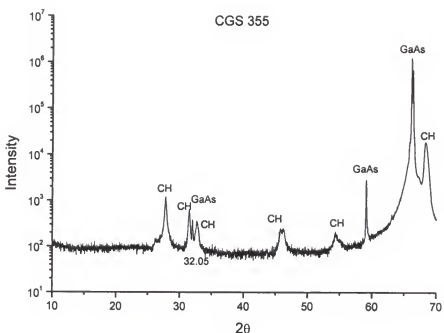
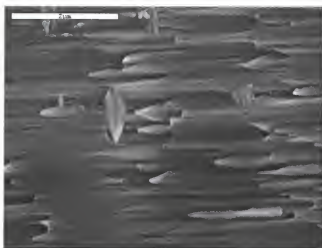
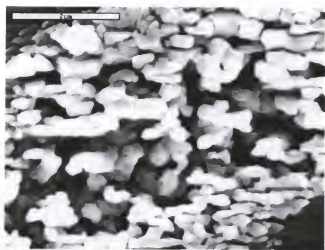


Figure 5.10 XRD θ - 2θ scan diffraction data of CuGaSe₂ film (CGS 355) grown on (001) GaAs: atomic ratio, $[\text{Cu}]/[\text{In}] = 1.09$.



(a)

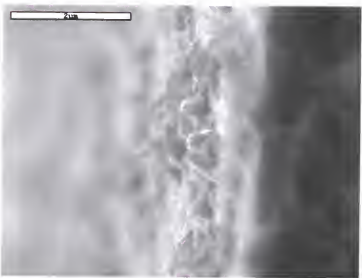


(b)

Figure 5.11 SEM images of CuInSe_2 (CIS 350) grown on (001) GaAs after KCN treatment, (a) background area ($\times 20000$), (b) island area ($\times 20000$).



(a)



(b)

Figure 5.12 SEM images of CuGaSe₂ (CGS 353) grown on (001) GaAs after KCN treatment: atomic ratio, [Cu]/[In] = 1.29, (a) plain view ($\times 20000$), (b) side view ($\times 20000$).

CHAPTER 6

THERMAL MODELING OF A ROTATING PLATEN AND SUBSTRATE IN A MIGRATION ENHANCED EPITAXY REACTOR

6.1 Introduction

The uniformity of the temperature distribution in a deposition reactors is crucial to the successful growth of thin films, especially when the heat flux is not constant through time and position. The temperature is typically measured at a few locations, and it is difficult to obtain the entire temperature profile over a large area. Achieving a direct temperature measurement is particularly challenging when dealing with moving substrates. As an effort to resolve this issue, numerical modeling can often be an alternative approach.

In this work, a modified molecular beam epitaxy reactor was used for depositing CuInSe₂ thin films used as an absorber layer for thin film solar cells (Stanbery 2002). The system is equipped with a rotating tungsten platen on which nine substrates can be loaded. The rotational motion of the platen delivers each substrate to the deposition zones and to a heating zone sequentially and periodically. As a result, the platen and the substrates are locally heated and cooled with a given periodicity. The rotational motion of the platen and the various heat sources define a significant temperature gradient on the platen and the substrate regions. This problem needs to be dynamically treated due to the periodical change of all conditions with respect to time. Moreover, direct temperature measurement during deposition runs is virtually impossible due to the rotational motion of the platen and the complex structures inside the reactor. These specific limitations

create significant complexities in the problem. A two-dimensional model of the heat transfer on the platen and the substrate regions is developed to investigate the nature and extent of the temperature profiles developed on the platen and substrates.

6.2 Experiments

The photovoltaics research group at the University of Florida has developed a migration-enhanced epitaxial growth (MEE) system for growing CuInSe₂-based absorber layers for solar cell applications (Stanberry 2002). It is a variant of the classical molecular beam epitaxy (MBE) system where an ultra high vacuum (UHV) environment and effusion cells are employed to generate the molecular beam fluxes of all the elemental sources (Cu, In, Ga, Se, and S). In the contrast with a typical MBE system, the MEE system is capable of accommodating up to nine substrates positioned on a large rotating platen. Another unique feature of the system is the sequential deposition of each source through a revolution of the platen, rather than simultaneous co-deposition from all the sources onto a substrate.

The MEE system is divided into four different zones as shown in Figure 6.1, namely, a heater zone, a metal deposition zone, a cooling zone, and a chalcogen deposition zone, which are encountered by any given substrate as the platen turns in the counter clockwise direction. The system features a rotating platen that delivers the substrates to all the zones sequentially and periodically. An electric heater is located in the heater zone; hence, the substrates and the platen are radiatively heated when they pass through that zone. In the other zones, the substrates cool slightly. In addition to the electric heater, the Cu, In, and the Ga effusion cells produce a radiative heat flux. The Se source operates at a low temperature, hence its contribution to the heat flux is negligible.

The MEE system creates an ultra high vacuum environment and generates molecular beam fluxes of the elemental sources. The base pressure can be maintained as low as 8×10^{-9} Torr. The pressure during deposition is in the range of 10^{-7} to 10^{-8} Torr depending on the operating conditions. Heat transfer from convection can be ignored since the pressure inside the reactor is very low.

Cu and In effusion cells are located in the metal deposition zone. Deposition of these metals occurs while the heated substrates pass through the zone. The rotation of the platen periodically delivers the substrates to the cooling zone (or load-lock zone) where neither deposition nor heating occurs. Finally, the substrates enter the chalcogen deposition zone where deposition of selenium or sulfur occurs. The sequential metal deposition, cooling, chalcogen deposition and heating steps are repeated by the rotation of the platen. A cryogenic shroud located below the platen is kept at a very low temperature (~ -196 °C) using liquid nitrogen. The direction of the rotation can be either clockwise or counter-clockwise so that the sequence of deposition may be reversed.

Note that the thermocouple is located in the gap between the electric heater and the platen (Figure 6.2). Due to the rotational motion of the platen and the substrates, the thermocouple cannot be attached to the platen or the substrates.

The actual temperature of the substrates was measured using a remote temperature logger, which is powered by a battery, and measures the substrate temperature and stores the temperature measurement in its own memory. This device was installed on the rotating platen, and the thermocouple contact was attached to the center of a substrate so that it rotates together with the platen and the substrates. The measurement area is limited to the center spot of a substrate. The logger and its stored data are retrieved after

a growth run is complete. Details of the device design and the experiment procedure are described in (Kincal 2002).

6.3 Modeling Equations and Strategy

Under low pressure conditions of the reactor ($\sim 10^{-8}$ Torr), all convection effects can be neglected; hence, the energy balance equations for the domain (platen and substrates) are

$$(x, y) \text{ Platen: } \rho_{Mo} \hat{C}_{pMo} \frac{\partial T}{\partial t} = k_{Mo} \left(\frac{\partial^2 T}{\partial x^2} + \frac{\partial^2 T}{\partial y^2} \right) + q_{rad}(x, y) \quad (6.1)$$

$$(x, y) \text{ Glass substrate: } \rho_g \hat{C}_{pg} \frac{\partial T}{\partial t} = k_g \left(\frac{\partial^2 T}{\partial x^2} + \frac{\partial^2 T}{\partial y^2} \right) + q_{rad}(x, y) \quad (6.2)$$

$$(x, y) \text{ Thermal-break: } \rho_{th} \hat{C}_{pth} \frac{\partial T}{\partial t} = k_{th} \left(\frac{\partial^2 T}{\partial x^2} + \frac{\partial^2 T}{\partial y^2} \right) \quad (6.3)$$

$$\text{Boundary conditions: } \left(\frac{\partial T}{\partial x} + \frac{\partial T}{\partial y} \right) = 0 \text{ at thermal domain boundaries} \quad (6.4)$$

Radiation heat flux to the thermal domain:

$$\text{from the main heater: } q_{rad}(x, y) = F^H \sigma (T_H^4 - T^4) \quad (6.5)$$

$$\text{from the Cu effusion cell: } q_{rad}(x, y) = F^{Cu} \sigma (T_{Cu}^4 - T^4) \quad (6.6)$$

$$\text{from the In effusion cell: } q_{rad}(x, y) = F^{In} \sigma (T_{In}^4 - T^4) \quad (6.7)$$

$$\text{from the cryo-shroud: } q_{rad}(x, y) = F^{Cr} \sigma (T_{Cr}^4 - T^4) \quad (6.8)$$

where q_{rad} is the net heat flux by radiation, T is the absolute temperature, ρ is the density, \hat{C}_p is the specific heat, k is the thermal conductivity, σ is Stefan-Boltzmann constant, and F is the view factor. The entire domain is initially at room temperature, and there is zero temperature gradient at the inner and the outer edge of the platen (6.4).

The problem requires a dynamic solution that considers the periodic effects on the heat distribution coming from the rotation of the platen. A convenient approach is to adopt time-varying view factors with respect of the heat sources. This makes it possible to keep the domain fixed. In other words, all the heating and the cooling sources are considered to be rotating while the platen is considered to be fixed in one location. For each heating or cooling source, the dimensionless view factors between a pair of surface elements dA_1 and dA_2 that face each other can be calculated from the equation,

$$F_{12} = \frac{1}{\pi A_1} \iint \frac{\cos \theta_1 \cos \theta_2}{d_{12}^2} dA_1 dA_2 \quad (6.9)$$

and the surface elements dA_1 and dA_2 are joined by a straight line of length d_{12} (Bird, 1960). The line makes an angle θ_1 with the normal vector to dA_1 , and an angle θ_2 with the normal vector to dA_2 . If the domain 1 (platen and substrates) is divided into small regions, the view factor (the fraction of radiation leaving a heat source that is directly intercepted by each divided region), can be also calculated for each small region by the same equation. When the divided region approaches to an infinitesimally small size, Equation (9) becomes

$$F_{12} = \frac{1}{\pi} \int \frac{\cos \theta_1 \cos \theta_2}{d_{12}^2} dA_2 \quad (6.10)$$

since the integrated values are kept constant within the infinitesimally small area. The view factors are calculated over the entire region and stored in tabular form in a file as a function of the position coordinates (x, y). Therefore, there are four different table files for the heat sources. In the simulation study, the dimensionless view factor on a specific position is obtained by interpolating the values in the corresponding table file. When the simulation program reads the data, the values periodically vary with time. The time

variable is converted to the corresponding position parameters. Figures 6.3 and 6.4 depict some of the view factors on the platen and their variation with respect to time.

The fact that the measurement of temperature is indirect and only at a single point prevents the acquisition of information on the temperature uniformity. A single thermocouple C-type is located in the middle of the gap, between the heater and the moving platen; hence, it reads some average temperature of the heater and the platen. It does not give full information about the temperature distribution on the substrates, which makes the experimental validation of the simulation result difficult. The view factors on the thermocouple are calculated by the same scheme used for the platen, and another heat balance equation is embedded for the thermocouple. Those two heat balance equations are simultaneously solved with the time-varying view factors in the simulation so that the correlation between the thermocouple reading and the actual temperature on the substrate surface can be obtained.

The substrates are positioned on the platen and held in place by gravity during the operation, *i.e.* the thermal contact between the substrates and the platen is poor; hence, a thin thermal-break region of very low thermal conductivity is introduced to simulate the contact resistance. The effect of the thermal-break region on the temperature uniformity is discussed in an ensuing section.

Significant simplification is obtained by assuming black-body radiation, an assumption that is not likely to produce significant errors since the distance between the simulated objects is much smaller than the objects' dimensions. A finite element solver is used for solving the differential equations.

6.4 Results and Discussion

Figure 6.5 depicts the final temperature profile as it changes periodically at each revolution. The calculation result demonstrates that the hottest position on the entire region is formed when the substrate exits the heating zone, *i.e.* right after the heating zone, and the coldest spot is formed when the substrate enters the heating zone, right after the cooling period. Figure 6.6 plots the temperature along the centerline of the substrate/platen region. It clearly demonstrates that there is a temperature gradient on the domain with respect to the angular position. The average temperature of the substrate region is considerably higher than that of the tungsten platen region because the position of the substrates is closer to the center line of the platen. In addition, a sharp change of temperature appears at the boundary between those regions, which is caused by the poor thermal contact. Figure 6.7 shows the temperature profiles on a substrate with and without the thermal break-region. The thermal contact resistance at the substrates-platen boundaries clearly improves the temperature uniformity on the substrate region since its existence reduces the heat transfer between those regions, and consequently flattens the temperature gradient around the edge of the substrate. The imaginary thermal-break region is made to have lower thermal diffusivity ($k/\rho\hat{C}_p$) than that of the glass substrate. It is demonstrated in Figure 6.7 that the lower thermal diffusivity results in more uniform temperature profile in the substrate region.

The thermal-break region also affects the pattern of the temperature profile in the substrate region. Figure 6.8 shows that the temperature profile on the substrate region has a somewhat parallel pattern to the direction of the rotation when the thermal-break region exists. Due to the design of the heater and the platen (Figure 6.2), the view factor

change with radial direction is larger than that with angular direction (Figure 6.3(a)). The thermal-break region forces that effect to remain dominant through the rotation by reducing the heat conduction between the substrate and the platen regions. Without the thermal-break region, the heat conduction becomes significant so that the temperature pattern of the substrate region becomes almost symmetrical (Figure 6.8 (c)).

A lower rotation speed of 12 rpm creates a higher temperature gradient through a revolution and higher temperature non-uniformity on the substrate region. In other words, the difference between the maximum and the minimum temperature within a substrate region is larger in case of the lower rotation speed. Consequently, the highest temperature on the substrates increases when the rotation speed decreases. The rotation speed should be kept above a certain value to obtain an acceptably uniform temperature distribution.

The rotation direction does not make any noticeable difference except that the temperature profile is now symmetrically reversed with respect to the radial direction since the effect of the main heater is dominant in the heat transfer, compared to the other heat sources.

The model predicts that the maximum temperature difference within the substrate region is at most 10 °C, and that the temperature variation experienced by any single substrate throughout a complete revolution is no greater than 10 °C when the peak temperature on the entire domain region is approximately 436 °C and the corresponding thermocouple reading is 650 °C. Such temperature variations are relatively small with respect to the peak temperature; therefore, the substrate temperature can be considered to

be fairly uniform with the thermal break-region. The uniformity is also maintained under lower control temperature.

The thermal modeling results were validated first by comparison to the temperatures measured using selected eutectic films that melt at specific temperatures. However, the eutectic-film technique is not a very precise method to calibrate the temperature and can estimate only the highest temperature point on the platen; hence, another experimental validation was conducted using the temperature logger. The electronic device that measures temperature and stores the data was installed onto a substrate. The logger and the stored data are retrieved after measurements. Figure 6.9 displays the results, showing that fairly good agreement is obtained considering that the finite-element model includes no model-fitting parameters.

6.5 Conclusions

A two-dimensional model of the heat transfer is developed for a rotating platen/substrates in a molecular beam epitaxy reactor. Time-varying view factors are calculated to solve the problem dynamically and to account for the fact that the platen rotates at a given angular speed. The relationship between actual temperature on the substrates and the thermocouple reading was also modeled. The poor thermal contact between the platen and the substrates is simulated by embedding a thin thermal break-region. The modeling study shows that the existence of the contact resistance thermally isolates the substrates from the platen to improve the temperature uniformity in the substrate region. The effects of rotation speed and rotation direction were also investigated. The modeling results predict the temperature distribution in the substrate regions to be fairly uniform under certain conditions. Good agreement with experimental validation result is obtained without using any model-fitting parameters.

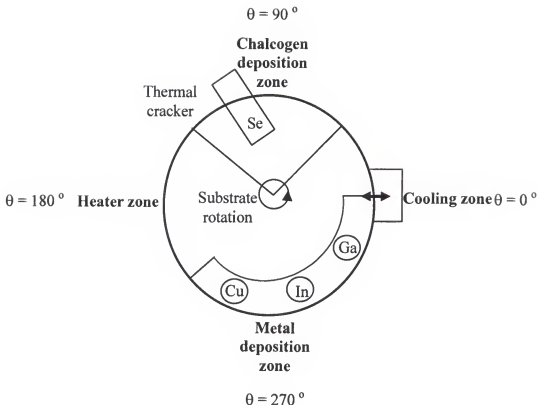


Figure 6.1 Schematic top view of the migration enhanced epitaxy reactor.

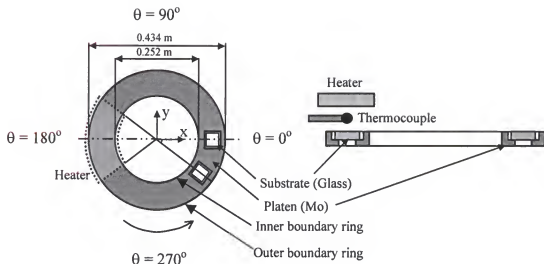


Figure 6.2 Schematic structure of the platen and the control thermocouple. (a) Top view of the platen showing two of the 9 substrate-holders and the position of the heater, (b) Cross-sectional view showing the mounting of the heater above the platen, the position of a thermocouple in the open gap, and the position of a glass substrate fitted in a holder that lies in an incision made in the platen.

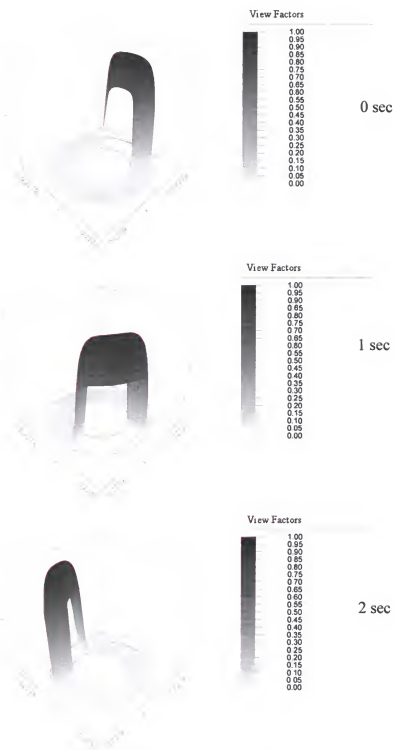


Figure 6.3 Time-varying view factors between the main heater and the platen at 20 rpm.

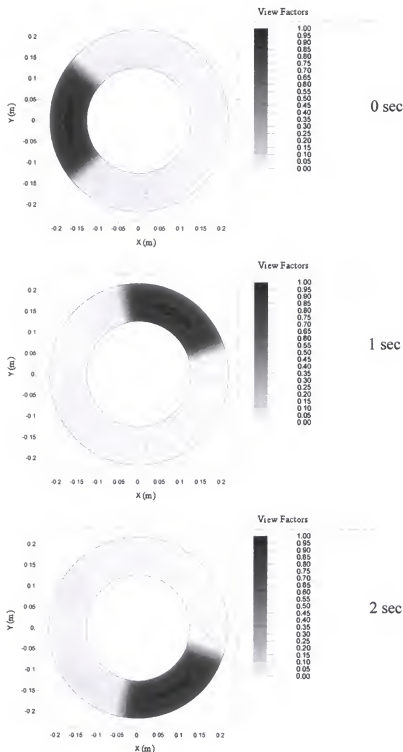


Figure 6.4 Time-varying view factors for the main heater at 20 rpm.

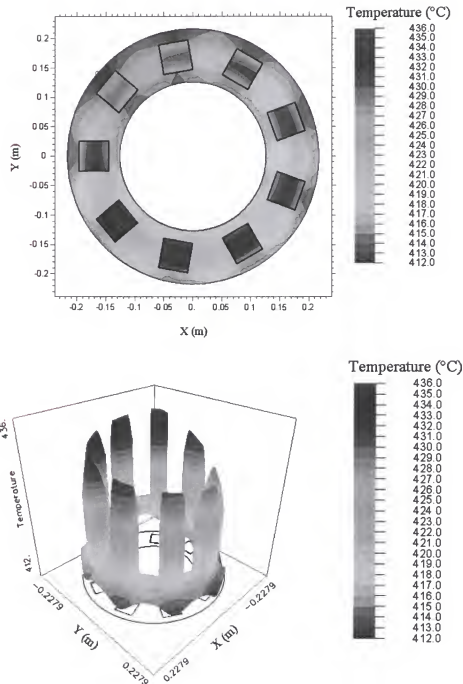


Figure 6.5 Temperature profile on the platen/substrates: thermocouple reading = 650 °C, rotation speed = 20 rpm with thermal-break region.

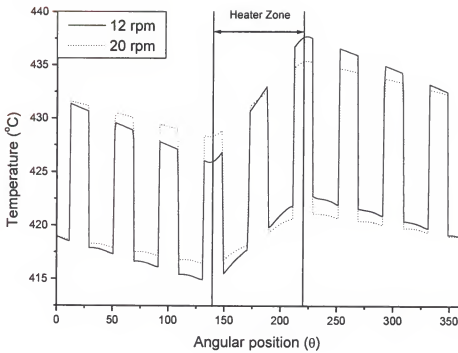


Figure 6.6 Temperature profile along the angular position: thermocouple reading = 650 °C.

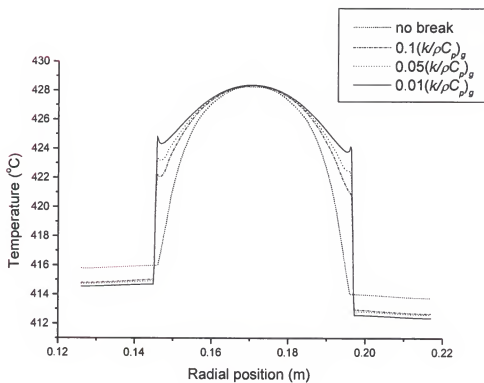
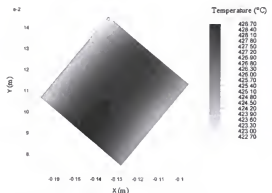
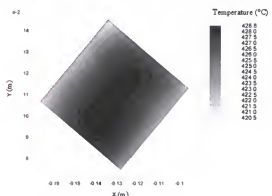
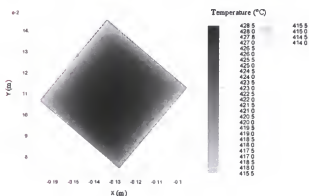


Figure 6.7 Temperature profile along the radial position at 140° with and without a thermal-break region: thermocouple reading = 650 °C, rotation speed = 20 rpm

(a) With a thermal-break region: $0.01(k/\rho C_p)g$ (b) With a thermal-break region: $0.05(k/\rho C_p)g$ 

(c) Without a thermal-break region

Figure 6.8 The effect of the thermal-break region on the pattern of temperature profile within a substrate at $\theta = 140^{\circ}$: thermocouple reading = 650°C , rotation speed = 20 rpm

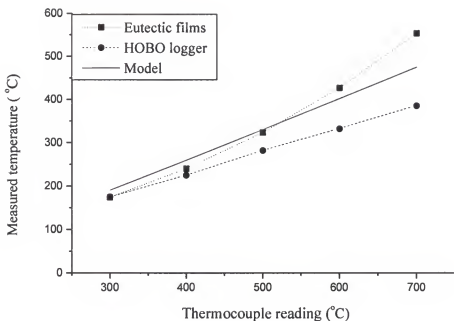


Figure 6.9 Comparison of the modeling result to the experiment: thermocouple reading = 650 °C, rotation speed = 20 rpm

CHAPTER 7 FUTURE WORK

7.1 High Temperature X-ray Diffraction

In Chapter 3 of this dissertation, it was demonstrated that the time-resolved high temperature X-ray diffraction provides a powerful method for studying the reaction kinetics and pathways of CuInSe₂ growth. It is thus suggested to further study the growth kinetics of Cu(In,Ga)Se₂-based films in details using the same technique. Several categories are suggested in the following sections.

7.1.1 Study of Reaction Kinetics of Binary Phases Formation

In a Cu-(In,Ga)-Se ternary or quaternary system, various binary and ternary phases can be present and transformed into many different phases during growth processes. It is believed that growth of Cu(In,Ga)Se₂ phase is controlled by reaction of multiple binary phases, such as CuSe, Cu_xSe, InSe, and In₂Se₃. Revealing the reaction kinetics of formation of those binary phases will be useful for the entire Cu(In,Ga)Se₂-based research area. High temperature XRD can be effectively used to investigate such phenomena in detail as demonstrated in Chapter 3. For example, the effects from the environment (vacuum, inert, oxidizing, and deoxidizing) and the temperature conditions can be investigated. Reaction pathways of formation of each binary phase can also be studied. Apparent activation energy and kinetic parameters of each reaction can be estimated using the HTXRD technique.

The precursor films need to be carefully designed to investigate specific reaction kinetics. The diffusion length of each elemental source and dimension of multiple

precursor layers should be considered in the design. Isothermal analysis can be used to conduct a quantitative study on reaction kinetics. Non-isothermal approach can give useful information for revealing the reaction pathways. The process parameters and the film structures can be optimized to grow a specific phase as a result of this study. Likewise, this study can be used to produce the phase diagrams for the binary and ternary systems. Figure 7.1 shows some possible precursor film structures considered for the study.

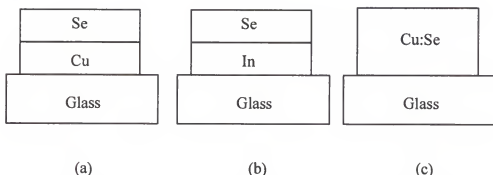


Figure 7.1 Schematic drawing of the precursor film structures: (a) Cu/Se, (b) In/Se, (c) Cu:Se.

7.1.2 Reaction kinetics of Cu(In,Ga)Se₂ Formation from Precursor Films

The study outlined in Chapter 3 can be continued for the gallium-containing Cu(In,Ga)Se₂ material system. The HTXRD system can provide various environments for the samples, such as vacuum, air, inert (He), oxidizing (O₂), and reducing (H₂). The effect of such environments can be studied in detail through the HTXRD study. This HTXRD study preliminarily demonstrated the positive effect of low pressure conditions on the growth of CuInSe₂ phase. It was also shown that the reaction pathways of CuInSe₂ formation could be engineered using various precursor film structures. Many different precursor films, such as, Cu/In/Se, CuSe/InSe, CuSe/In:Se, InSe/Cu:Se, Cu:In:Se, and In₂Se₃/Cu₂Se, can be examined. Replacing the indium with gallium will

produce another series of experiment. Sodium effect on the phase evolution and the growth mechanism leading to a final phase can be also explored through the HTXRD study.

For some studies, it is recommended to use In_2Se_3 and Cu_2Se phases rather than InSe and CuSe . In_2Se_3 and Cu_2Se phases are more stable so that they can be grown more reproducibly and homogeneity of the films may be superior.

7.1.3 *In-situ* Investigation of Grain Growth and Epitaxy

The grain growth mechanism of $\text{Cu}(\text{In},\text{Ga})\text{Se}_2$ -based thin films has been a focus of many studies since the grain size distribution is an important factor to the solar cell performance. Most of the studies provided only ex-situ analyses results; however, an ex-situ study may not replicate the detailed grain growth mechanism in these thin films. One of the best approaches may be *in-situ* study of the phenomena using time-resolved high temperature X-ray diffraction analysis, where direct kinetic measurements from the changes in the XRD data with time during heating of the films can be observed. Careful analysis of the *in-situ* XRD data with an analysis software (*e.g.*, JADE) may permit a quantitative investigation on the grain growth kinetics.

Chapter 4 of this dissertation provided insight on the role of secondary phases on the grain growth mechanism of CuInSe_2 films. Combined with the HTXRD technique, the phenomena can be *in-situ* studied to give more detailed results. A few of the possible precursor structures are given in Figure 7.2.

The first structure has the bottom layer of a nanocrystalline CuInSe_2 film that can be grown under low temperature and indium-rich conditions. The top layer is a copper selenide (CuSe) phase. While the precursor structure is being heated isothermally or non-isothermally, the HTXRD data can be simultaneously collected. Time-resolved phase

evolution and grain growth mechanism can be detected and analyzed through the HTXRD. The second structure (Figure 7.2 (b)) is a simple mixture of elemental copper, indium, and selenium. This structure can be grown using co-deposition process under very low or room temperature condition. The atomic $[Cu]/[In]$ ratio should be carefully designed to investigate its effect on the grain growth mechanism for both precursor structures.

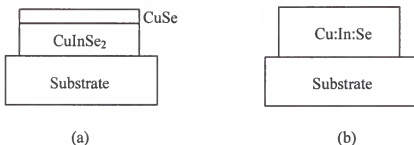


Figure 7.2 Schematic drawing of the precursor film structures: (a) CuInSe₂/CuSe, (b) mixture of elemental copper, indium, and selenium.

It is plausible to conduct an *in-situ* study of epitaxial growth of Cu(In,Ga)Se₂-based thin films with the same technique. Very thin precursor films (<200 nm) can be grown on a single crystalline substrate, such as GaAs, Si, ZnTe, and SrF, using the MEE reactor. The HTXRD scanning during heating the samples may capture the rearrangement of the film structure and the transition to epitaxial growth. Specially, it may be possible to detect and analyze the initial nucleation step of the epitaxial growth process. This study may give us valuable information of important factors, *e.g.*, process parameters and role of specific phase for the epitaxial growth process. The precursor structures on the single crystalline substrate should be grown under high vacuum and well preserved until the HTXRD experiment to prevent any undesired contamination. The growth reactor of our research group, MEE, and the HTXRD is an ideal combination for the above research topics.

7.2 Study of the Relationship between Electrical Properties and Surface Phase of CuIn(S, Se)₂ Thin Films: Engineering of Bandgap and Surface Phase

7.2.1 Background

The chalcopyrite CuInSe₂ is a promising material for the absorber layer in solar cells due to its direct band gap energy of 1.04 eV; however, a wider band gap is desired to enhance the cell voltage since it is advantageous for the series integration of connected modules. Another reason for the preference of a wider band gap material is that 1.4 eV is theoretically optimal value for a single junction solar cells (Möller 1993). The ideal band gap can be achieved by substituting S in CuInSe₂ for Se.

It is still a challenging topic to fabricate a sulfur-based I-III-VI₂ compound absorber layer due to its very low carrier (hole) concentration, despite its almost perfect match of the band gap to the ideal value (~1.4 eV). The origin of the related disadvantageous electrical properties and the fundamental physics are not well understood. Many experimental results show that the activation energies of the acceptor levels shift to higher values, and the acceptor carriers are more strongly compensated when selenium is substituted by sulfur. It seems that the low carrier concentration is caused by the higher activation energy for formation of the p-type intrinsic dopant (hole) and strong compensation in the sulfur-based material. Whether this is related to preparation technology or intrinsic material properties, however, is not yet clear.

From related studies it is well known that as-grown single layer of indium-rich CuInS₂ has a very low carrier concentration. It seems that an acceptable carrier concentration can be achieved only by growing Cu-rich film followed by etching out the Cu-rich secondary phases with KCN (Scheer 1993). However, the etching process is not

appropriate in commercial applications due to its high toxicity. The etching also leaves deep hole at the surface region, and it may be detrimental to device performance.

From many experimental results, it has been found that the surface region of In-rich chalcopyrite films is covered by strongly In-rich secondary phase that is called an ordered defect crystal (ODC). This surface phase very likely plays an important role in determining the electrical properties, *e.g.*, hole concentration in the junction area. A challenge is how to control the surface phase formation. It is possible that engineering the surface phases will improve the electronic properties of CuInS₂ thin films, and make it possible to eliminate using the KCN etching process in fabricating CuInS₂-based solar cells. Improvement of the surface morphology is expected as well.

A bi-layer structure is proposed for resolving the problem, beginning with Cu-rich CuInS₂ film and completing the deposition with In-rich CuInSe₂. In that case, a selenium-based surface phase will form instead of sulfur-based surface phase while maintaining the stoichiometric composition of CuInS₂ in the bulk region. The selenium-based surface phase is much less compensating of hole carriers. This should result in higher carrier concentration in the absorber layer. This research will help to produce a wide band gap thin film (~1.4eV) with acceptable hole concentration.

7.2.2 Electronic and Structural Properties of CuInS₂ Thin Films

With the ideal band gap energy, CuInS₂ can be applied for both single junction thin-film solar cell as well as top junction of a tandem device (Alt 1997). For this reason, many researchers have been trying to fabricate the sulfur-based chalcopyrite thin film solar cells; however, its performance considerably falls behind the values achieved with CuInSe₂ absorbers to date (Nakabayashi 1997, Negami 1997). It is believed that one of the main reasons for the poor efficiency comes from the intrinsic material properties of

the In-rich CuInS₂ absorber layer. It somehow leads to very low carrier concentration in In-rich CuInS₂ films. Although numerous efforts have been made to improve the electrical property (mostly carrier concentration) of the material, the result has not been successful to date.

Various deposition techniques have been used to grow thin film CuInS₂. Reasonable efficiencies (10 to 12%) could be achieved by a three source co-evaporation (Scheer 1993, Brauner 1996) and a two-step process using H₂S (Ogawa 1994, Nakada 1997) or elemental sulfur vapor (Klenk 1997). The CuInS₂-based material studied are ternary, quaternary, and pentanary species such as CuInS₂, CuIn(S,Se)₂ (Eisener 2000, Zeaiter 2000, Adurojija 1999) and Cu(In,Ga)(S,Se)₂ (Nakada 1997).

The structural and electronic properties of CuInS₂ thin films strongly depend on the composition ratio between Cu and In, [Cu]/[In], as other chalcopyrite materials (Scheer 1994). It shows very similar behavior to the other CuInSe₂-based thin films in many aspects. For example, it has been found that Cu-rich CuInS₂ films exhibit a considerably larger grain size and the surface is covered with CuS phase that represents a semi-metallic phase (Scheer 1994, Scheer 1995). This secondary phase is a degenerate p-type and detrimental to the photovoltaic devices similarly as the Cu-Se secondary phases in the CuInSe₂. Cu-S phases can be selectively removed by etching process using KCN solution. Most of the CuInS₂-based solar cells were fabricated growing the Cu-rich thin film and etching out the Cu-S phases (Figure 7.3).

For In-rich films, it was found that even slightly In-rich composition in the bulk leads to drastic indium enrichment on the surface ($In/(In+Cu) \sim 0.75$) (Scheer 1994). The respective surface composition for the In-rich film corresponds to the stoichiometry of

CuIn_3S_5 . It is well known that CuIn_3Se_5 is a dominant surface phase in In-rich CuInSe_2 thin films and a strongly compensated n-type material. The CuIn_3S_5 is even more strongly compensated phase (stronger n-type) due to its intrinsic material property. It can be inferred that the existence and amount of the indium-rich secondary phase in CuInS_2 thin film may significantly affect the electrical properties of the absorber layer.

A single layer of as-grown In-rich CuInS_2 contains a large portion of the indium-rich secondary phases, CuIn_3S_5 (Figure 7.4). The single layers are known for having extremely low concentration of hole carriers so that it cannot be applied for the solar cells as mentioned above. Most of the CuInS_2 solar cells that attained reasonable efficiency were fabricated growing Cu-rich thin film and etching out the Cu-rich secondary phases (Figure 7.3). It is pointed out that formation of the In-rich secondary phase can be possibly prevented or minimized by that technique. The reason of such a low carrier concentration in the In-rich CuInS_2 may be the large portion of the In-rich secondary phases that strongly compensates the p-type carriers. The etching process is a drawback due to its toxicity; hence, it should be avoided after all for commercial applications.

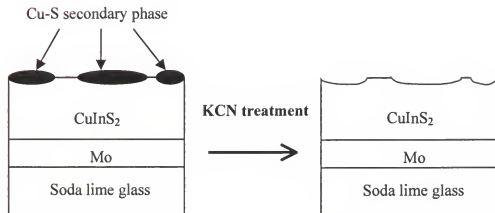


Figure 7.3 A typical process for CuInS_2 absorber layer: Cu-rich CuInS_2 thin film is grown and the secondary phase on the surface is etched out by KCN solution.

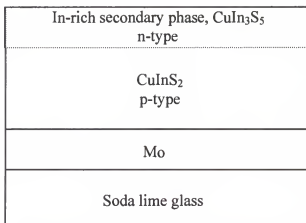


Figure 7.4 Schematic structure of an as-grown single layer of the In-rich CuInS_2 .

As for CuInSe_2 thin films, high crystalline CuInSe_2 thin film can be grown without the KCN treatment by adopting the bi-layer growth process. Cu-rich CuInSe_2 thin film is first grown and followed by deposition of In-rich CuInSe_2 . The latter step converts the overall composition from Cu-rich to slightly In-rich. The same technique has been tried for growing CuInS_2 of high carrier concentration; however, the results have not been successful to date. One possible explanation is that the In-rich secondary phase, *e.g.*,

CuIn_3S_5 can still form on the surface region. Co-deposition of sulfur and selenium has been also conducted (Eisener 2000, Zeaiter 2000); however, the reproducibility of controlling the composition of each material is a challenge. In addition, added selenium will reduce the energy band gap from the ideal value.

As for Cu-rich films, the Fermi level was found approximately at the valence band maximum, $E_F-E_V = 0.0$ eV, which refers to a degenerate p-type character of these films (Scheer 1994). The Fermi level at the surface of the base material is found at $E_F-E_V = 0.5$ eV, after removing the CuS phase at the surface. The removal of CuS is indicated by the complete recovery of the CuInS_2 valence band structure. The Fermi level in In-rich films was found to be approximately 1.3 eV from the valence band maximum indicating n-type conductivity of the surface phase.

From the discussion above, it can be concluded that the surface properties (structural and electronic) are highly sensitive for alterations in the CuInS_2 bulk stoichiometry. In addition, the surface phases very likely play an important role in determining the overall electronic properties (conductivity, built-in electric field and carrier concentration) and forming a homogeneous p-n junction, as in the case of CuInSe_2 . Therefore, controlling the surface phase and its properties will bring a break-through in improving the performance of CuInS_2 -based solar cells.

Extensive study on the issue, correlation between the electronic properties and the experimental parameters, need to be conducted to better understand the fundamentals and jump to the next level of the wide band gap application in solar cells. The University of Florida facility has a unique capability of depositing selenium and sulfur sources sequentially or simultaneously. It is appropriate for engineering of band gap and other

parameters. The effect of adding certain species, *e.g.*, sodium on the structural and electronic properties can be investigated as well.

7.2.3 Bi-layer Structure for CuInS₂-based Absorber Layer

A new growth process is being considered for CuInS₂ thin film growth to improve the electrical properties and avoid the KCN treatment at the same time. The first and most important goal in this research is to increase the carrier concentration of CuInS₂ thin films without any wet etching process. As mentioned above, even slightly In-rich film shows extremely low carrier concentration since the indium-rich phase is very strongly compensated. To date, the only method of achieving the reasonable level of carrier concentration in CuInS₂ thin film is growing a Cu-rich film and etching the secondary Cu-S phase afterwards. This method seems to minimize the In-rich phase and more importantly prevents formation of the indium-rich secondary phase *i.e.* CuIn₃S₅ on the surface region. It is believed that these are the key factors in determining the electrical properties of the entire absorber layer. However, the wet etching process needs to be avoided the toxicity of the etching solution (KCN) and the wet process are not appropriate for a commercial application.

As a summary, to deposit a wide band gap absorber layer, the following conditions should be fulfilled: (1) Most of the film is the wide band gap material (CuInS₂), (2) Certain level of hole concentration should be achieved (10^{16} to 10^{17} cm⁻³), and (3) Wet etching should not be used.

The composition of bulk material need to be maintained close to stoichiometry to obtain high carrier concentration, while the overall composition should be slightly In-rich so not to introduce the detrimental secondary phases, Cu-S. To satisfy both restrictions, a double- or bi- layer structure is an appropriate approach.

A proposed bi-layer structure that is sequentially deposited, to fulfill both goals is shown in Figure 7.5. First, Cu-rich CuInS₂ film will be grown during the initial growth stage. Then, sulfur flux will be changed to selenium. Simultaneously, the vapor phase from the source fluxes will be converted into In-rich environment by increasing the flux ratio, [In]/[Cu]. As a result, most of the bulk region is expected to be stoichiometric or slightly In-rich CuInS₂, while the surface phase is the In-rich secondary phase that is based on selenium instead of sulfur. The selenium-based surface phase, *e.g.*, CuIn₃Se₅ will be much less compensating the hole carriers. This may result in a higher carrier concentration in the absorber layer. This process will produce a wide band gap thin film ($\sim 1.4\text{ eV}$) with acceptable hole concentration. We think that formation of the sulfur-based indium-rich surface phases that strongly compensate the hole carriers (p-type carrier), can be controlled or prevented by the process proposed here.

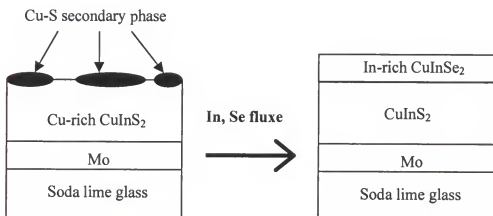


Figure 7.5 Bi-layer process for CuInS₂ absorber layer deposition to prevent the formation of the In-rich CuInS₂ secondary phase, CuIn₃S₅.

7.3 Continuous Deposition of Cd-free Buffer Layers without Breaking Vacuum

7.3.1 Background

The buffer layer is an important factor for overall performance (efficiency) of CIS-based solar cells, especially for the high efficiency solar cells. It is believed that the buffer layer is related to the p-n junction formation and acts as a carriers trap; hence, significantly affects the electrical property of the device. To date, CdS growth by chemical bath deposition (CBD) shows the best result. However, the CBD CdS process is considered an obstacle for commercial application of the CIS solar cell due to its detrimental effect on the environment, and potentially has a contamination problem during the process. A new buffer layer process that is clean and compatible with vacuum growth process can be very advantageous for commercial application.

Some reports show the possibility of using a InS or InSe thin layer as the alternative for the CBD-grown CdS (Barreau 2000, Yousfi 2000). Unique capabilities of our system, atomic layer deposition and being equipped with both of selenium and sulfur sources, give us great opportunity of exploring this topic. To minimize the buffer layer thickness, in my opinion, RTP can be used as a post deposition process. After deposition of the InS or InSe thin layers (<50nm) under low temperature conditions, RTP will be used for crystallization and chemical bonding of the deposited films. The superior temperature controllability and more sophisticated control capability of the combined process will be advantageous in the thickness control over the typical CBD process.

7.3.2 Alternative Buffer Layers

To date, the best solar cell performance has been achieved by involving CBD-grown CdS buffer layers. CBD-grown CdS has its own advantages, such as the simplicity of the process, good reproducibility, and fitting with large area processing. However, there is a

considerable interest in replacing CdS by a cadmium-free buffer layer, for environmental reason and possible gains in efficiency associated with larger band gap energy. In a NREL report, they mentioned the importance of replacing CdS buffer layer by a cadmium-free layer to give the technology a “green” (environmentally friendly) appearance. There is a great deal of research under way in Japan, Germany, and the United States to replace the CBD CdS by other candidates, such as In(OH)_2 , In_xS_y , In_xSe_y , SnO_2 , ZnO , ZnSe or ZnS (Barreau 2000, Yousfi 2000, Yousfi 1997, Bayón 1999).

Among these materials, it is suggested that In_xS_y and In_xSe_y are good candidates in that our system has capability of depositing both materials and their growth is compatible with vacuum process. Deposition of the buffer layer without breaking vacuum after the absorber layer growth has a big advantage since it will significantly reduce not only the processing time but also the possibility of contamination problem.

7.3.3 Growth Process and Properties of Indium Sulfide and Indium Selenide

Several different processes have been adopted to grow the binary phase films, InS and InSe . Thin films of $\beta\text{-In}_2\text{S}_3$ were obtained by physical vapor deposition process followed by a post-annealing (Barreau 2000). The deposition of the film was carried out by vacuum thermal evaporation at a gas pressure of 5×10^{-4} Pa using crucibles for each source. According to their result, some oxygen is substituted for sulfur during the crystallization of the films. The atomic percentage of oxygen was 3 to 5%, and the band gap of the film changed from 2.1 eV for pure In_2S_3 to 2.9 eV with oxygen incorporation. This result attracts additional interest in the material and the corresponding process since the band gap is one of the primary parameters that determine the quality of buffer layers. Higher band gap value results in less absorption of the sun light through the buffer layer;

hence, it usually leads to higher efficiency of the solar cell device. Compared to the band gap of CdS, 2.4eV, indium sulfide can be made to have a higher band gap. The fact that the band gap of indium can be engineered by additional process, such as adding oxygen during growth, is additional potential benefit from the indium sulfide films. They also reported a high transmission, covering efficiency and n-type conductivity that are necessarily required as a candidate for buffer layers.

Some solar cell devices have been fabricated using indium sulfide buffer layer (Yousfi 2000). Their best result was an efficiency of 13.5% that is similar to that from using CBD-grown CdS buffer layer. Atomic layer epitaxy process was used for deposition of the buffer layer and the ZnO window layer in their experiments to minimize the sputtering damage and employ a high controllability of the process. The University of Florida growth system has a similar feature to the ALE process (see the system description, Chapter 1.5).

A research group obtained InSe polycrystalline films from indium selenide by thermal evaporation onto glass substrates (Parlak 1995). The composition and the phase of the films varied from $\text{In}_{48.13}\text{Se}_{51.87}$ to $\text{In}_{46.66}\text{Se}_{53.44}$ depending on a post-annealing process. Indium selenide thin films can be also grown from other methods, such as molecular beam epitaxy and flash evaporation (Julien 1990, Ohtake 1997). It seems to be hard to prepare high quality InSe films due to the coexistence of several indium selenide phases (Segura 1983). It has been also considered as a suitable absorber layer because of its energy band gap (1.3eV) and its optical and transport properties (Sánchez-Royo 1997, Segura 1983); however, the band gap does not seem to be high enough for buffer layer application. Therefore, we think that engineering the surface phase of absorber layers

with this material is more appropriate approach rather than using it directly as a buffer layer at this point.

LIST OF REFERENCES

Adams C.D., M. Atzmon, Y.T. Cheng, and D.J. Srolovitz, "Phase separation during co-deposition of Al-Ge thin films", *J. Mater. Res.* **vol. 7**, 653 (1992).

Adurojija F.O., J. Song, I.O. Asia, and K.H. Yoon, "Formation of CuIn(S,Se)₂ thin film by thermal diffusion of sulfur and selenium vapours into Cu-In alloy within a closed graphite container", *Solar Energy Materials and Solar Cells* **vol. 58**, 287 (1999).

Alt M., H.J. Lewerenz, and R. Scheer, "CuInS₂ thin film growth monitoring by in situ electric conductivity measurements", *J. Appl. Phys.* **vol. 81**, 956 (1997).

Atkinson H.V., "Theories of normal grain growth in pure single phase systems", *Acta Metallurgica* **vol. 36**, 469 (1988).

Bamford C.H. and C.F.H. Tipper, *Reactions in the solid state*, Elsevier Scientific Publishing Company, Amsterdam, New York, (1980).

Barreau N., S. Marsillac, J.C. Bernède, and A. Barreau, "Investigation of β -In₂S₃ growth on different transparent conductive oxides", *Applied Surface Science* **vol. 161**, 20 (2000).

Bayón R., C. Maffiotte, and J. Herrero, "Chemical bath deposition of indium hydroxy sulphide thin films: process and XPS characterization", *Thin Solid Films* **vol. 353**, 100 (1999).

Bird R.B., W.E. Stewart, and E.N. Lightfoot, *Transport phenomena*, John Wiley & Sons, New York (1960).

Birkmire R.W., "Compound polycrystalline solar cells: Recent progress and Y2K perspective", *Solar Energy Materials & Solar Cells* **vol. 65**, 17 (2001).

Bodegard M., J. Hedstrom, K. Granath, A. Rockett, and L. Stolt, "ZnO/CdS/Cu(In,Ga)Se₂ thin film solar cells with improved performance", *Proceedings of the 13th European Photovoltaic Solar Energy Conference*, 2080 (1995).

Brand J.A. and H.J. Goldschmidt, "The problem of temperature calibration in a high temperature X-ray diffraction camera", B.S.A. Group Research Center Sheffield, GRC/G 1109, (1955).

Braunger D., D. Hariskos, T. Walter, and H.W. Schock, "11.4% efficient polycrystalline thin film solar cell based on CuInS₂ with a Cd-free buffer layer", *Solar Energy Mater. Solar Cells* **vol. 40**, 97 (1996).

Braunger D., Th. Duerr, D. Hariskos, Th. Walter, N. Wieser, and H.W. Schock, "Improved open circuit voltage in CuInS₂-based solar cells", Proceedings of the 25th IEEE PVSC, 1001(1996).

Bube R.H., *Photovoltaic materials*, Imperial College Press, London (1998).

Burgelman M., F. Engelhardt, J.F. Guillemoles, R. Herberholz, M. Igelson, R. Klenk, M. Lampert, T. Meyer, V. Nadenau, A. Niemegeers, J. Parisi, U. Rau, H.W. Schock, M. Schmitt, and O. Seifert, "Defect in Cu(In,Ga)Se₂ semiconductors and their role in the device performance of thin-film solar cells", *Progress in Photovoltaics: Research and Applications* **vol. 5**, 121 (1997).

Cahn R.W., *Physical metallurgy*, Chapter 19, edited by R.W. Cahn, Amsterdam, (1970).

Cahen D. and R. Noufi, "Defect chemical explanation for the effect of air anneal on CdS/CuInSe₂ solar cell performance", *Appl. Phys. Lett.* **vol. 54**, 558 (1989).

Chang C.H., "Processing and characterization of copper indium selenide for photovoltaic applications", Ph.D. Dissertation, University of Florida (1999).

Christian J.W., *The theory of transformations in metals and alloys, part I*, Pergamon press, New York, **vol. 542** (1975).

Clevenger L.A. and C.V. Thompson, "Nucleation-limited phase selection during reactions in nickel/amorphous-silicon multiplayer thin films", *J. Appl. Phys.* **vol. 63**, 1325 (1990).

Devaney W.E., W.S. Chen, J.M. Stewart, and R.A. Mickelsen, "Structure and properties of high efficiency ZnO/CdZnS/CuInGaSe₂ solar cells", *IEEE Trans. Electron. Devices* **vol. 37**, 428 (1990).

Eisener B., D. Wolf and G. Müller, "Influence of sulphur on the electrical and optical properties of p-type CuIn(S_xSe_{1-x})₂ single crystals", *Thin Solid Films* **vol. 361-362**, 126 (2000).

Givargizov E.I., *Oriented Crystallization on amorphous substrates*, Plenum Publishing Corp., New York, (1991).

Hariskos D., M. Ruckh, U. Ruehle, T. Walter, H.W. Schock, J. Hedstroem, and L. Stolt, "Novel cadmium free buffer layer for Cu(In,Ga)Se₂ based solar cells", *Solar Energy Mater. Solar Cells* **vol. 41-42**, 345 (1996).

Hillert M., "On the theory of normal and abnormal grain growth", *Acta Metallurgica* vol. 13, 227 (1965).

Hulbert F., "Models for solid-state reactions in powdered compacts: a review", *J. Br. Ceram. Soc.*, vol. 6, 11 (1969).

JADE, a program for powder diffraction data analysis, Materials Design Inc., Livermore, CA, USA.

Johnson W.L., "Thermodynamic and kinetic aspects of the crystal to glass transformation in metallic materials", *Prog. Mater. Sci.* vol. 30, 81 (1986).

Julien C., N. Benramdane, and J.P. Guesdon, "Transformation steps of structure in flash-deposited films of a-InSe", *Semicond. Sci. Technol.* Vol. 5, 905 (1990).

Kincal S., "Modeling and Control of Multiple Thermal Effusion Sources and Substrate Temperature in Molecular Beam Epitaxy Reactors", Ph.D. Dissertation, University of Florida (2002).

Klenk R., T. Walter, H.W. Schock, and David Cahen, "A model for the successful growth of polycrystalline films of CuInSe₂ by multisource physical vacuum evaporation", *Advanced Materials* vol. 5, 114 (1993).

Klenk R., U. Blieske, V. Dieterle, K. Ellmer, S. Fiechter, I. Hengel, A. Jäger-Waldau, T. Kampschulte, Ch. Kaufmann, J. Klaer, M.Ch. Lux-Steiner, D. Braunger, D. Hariskos, M. Ruckh, and H.W. Schock, "Properties of CuInS₂ thin films grown by a two-step process without H₂S", *Solar Energy Materials and Solar Cells* vol. 49, 349 (1997).

Klais J., H.J. Möller, and D. Cahen, "Calculation and experimental characterization of the defect physics in CuInSe₂", *Thin Solid Films* vol. 361-362, 446 (2000).

Kronik L., U. Rau, J.F. Guillemoles, D. Braunger, H.W. Schock, and D. Cahen, "Interface redox engineering of Cu(In,Ga)Se₂-based solar cells: oxygen, sodium, and chemical bath effects", *Thin Solid Films* vol. 361-362, 353 (2000).

Lakshmikumar S.T. and A.C. Rastogi, "Critical influence of reactant pressure on the evolution of single phase CuInSe₂ selenization at low temperatures", *Appl. Phys. Lett.* vol. 66, 3128 (1995).

Lakshmikumar S.T. and A.C. Rastogi, "Phase evolution in low-pressure Se vapor selenization of evaporated Cu/In bilayer precursors", *J. Appl. Phys.* vol. 79, 3585 (1996).

Li S.S., *Semiconductor physical electronics*, Plenum Press, New York (1993).

Liao D. and A. Rockett, "Epitaxial growth of Cu(In,Ga)Se₂ on GaAs(110)", *J. Appl. Phys.* vol. 91, 1978 (2002).

Lind C., A.p. Wilkinson, C.J. Rawn, and E.A. Payzant, "Kinetics of the cubic to trigonal transformation in $ZrMo_2O_8$ and their dependence on precursor chemistry", *J. Mater. Chem.* **vol. 12**, 990 (2002).

Ma E., C.V. Thompson and L.A. Clevenger, "Nucleation of an intermetallic at thin-film interfaces: VS_2 contrasted with Al_3Ni ", *J. Appl. Phys.* **vol. 69**, 2211 (1991).

Möller H.J., *Semiconductors for solar cells*, Artech House, Boston (1993).

Nadenau V., D. Braunger, D. Hariskos, M. Kaiser, Ch. Köble, A. Oberacker, M. Ruckh, U. Ruhle, D. Schmid, T. Walter, S. Zweigart, and H.W. Schock, "Solar cells based on $CuInSe_2$ and Related compounds: Material and Device properties and processing", *Progress in Photovoltaics: Research and Applications* **vol. 3**, 363 (1995).

Nadenau V., G. Lippold, U. Rau, and H.W. Schock, "Sodium induced secondary phase segregations in $CuGaSe_2$ thin films", *J. Crystal Growth* **vol. 233**, 13 (2001).

Nakabayashi T., T. Miyazawa, Y. Hashimoto, and K. Ito, "Over 10% efficient $CuInS_2$ solar cell by sulfurization", *Solar Energy Materials and Solar Cells* **vol. 49**, 375 (1997).

Nakada T., H. Ohbo, T. Watanabe, H. Nakazawa, M. Matsui, and Akio Kunioka, "Improved $Cu(In,Ga)(S,Se)_2$ thin film solar cells by surface sulfurization", *Solar Energy Materials and Solar Cells* **vol. 49**, 285 (1997).

Nakada T. and A. Kunioka, "Direct evidence of Cd diffusion into $Cu(In,Ga)Se_2$ thin films during chemical-bath deposition process of CdS films", *Applied Physics Letters* **vol. 74**, 2444 (1999).

Negami T., Y. Hashimoto, M. Nishitani, and T. Wada, " $CuInS_2$ thin-films solar cells fabricated by sulfurization of oxide precursors", *Solar Energy Materials and Solar Cells* **vol. 49**, 343 (1997).

Niemi E. and L. Stolt, "Characterization of $CuInSe_2$ thin films by XPS", *Surface and Interface Analysis* **vol. 15**, 1989 (1990).

Niki S., Y. Makita, A. Yamada, A. Obara, S. Misawa, O. Igarashi, K. Aoki, and N. Kutsuwada, *Jpn. J. Appl. Phys. Part I* **vol. 23**, 161 (1993).

Niki S., P.J. Fons, A. Yamada, Y. Lacroix, H. Shibata, H. Oyanagi, M. Nishitani, T. Negami, and T. Wada, "Effects of the surface phase $Cu_{2-x}Se$ phase on the growth and properties of $CuInSe_2$ films", *Appl. Phys. Lett.* **vol. 74**, 1630 (1999).

Nomura S., J. Ishikawa, F. Iinuma, and T. Takizawa, "Chemical reaction processes in synthesizing $CuInSe_2$ from the elements by the melting method", *Jpn. J. Appl. Phys.* **vol. 30**, 2040 (1991).

Norsworthy G., C.R. Leidholm, A. Halani, V.K. Kapur, R. Roe, B.M. Basol, and R. Matson, "CIS film growth by metallic ink coating and selenization", *Solar Energy Materials and Solar Cells* **vol. 60**, 127 (2000).

Ogawa Y., A. Jager-Waldau, Y. Hashimoto, and K. Ito, "In₂O/CdS/CuInS₂ thin-film solar cell with 9.7% efficiency", *Jpn. J. Appl. Phys.* **vol. 33**, 114 (1994).

Ohtake Y., T. Okamoto, A. Yamada, M. Konagai, and K. Saito, "Improved performance of Cu(InGa)Se₂ thin-film solar cells using evaporated Cd-free buffer layers", *Sol. En. Mater. Solar Cells* **vol. 49**, 269 (1997).

Palmer J.E., C.V. Thompson, and H.I. Smith, "Grain growth and grain size distributions in thin germanium films", *J. Appl. Phys.* **vol. 62**, 2492 (1987).

Parlak M., C. Ercelebi, I. Gunal, Z. Salaeva, and K. Allakhverdiev, "Growth and characterization of polycrystalline InSe thin films", *Thin Solid Films* **vol. 258**, 86 (1995).

Partain L.D., *Solar cells and their applications*, John Wiley & Sons, New York (1995).

Pascual R., M. Sayer, A. Lo, S. Herbert, L.C. Rolim, and N. Townley, "Simulation of the crystallization of thin films by rapid thermal processing", *J. Appl. Phys.* **vol. 79**, 493 (1996).

Ramanathan K., R. Noufi, J. Granata, J. Webb, and J. Keane, "Prospects for in situ junction formation in CuInSe₂ based solar cells", *Solar Energy Materials and Solar Cells* **vol. 55**, 15 (1998).

Rastogi A.C., K.S. Balakrishnan, R.K. Sharma, and K. Jain, "Growth phases during electrochemical selenization of vacuum deposited Culn metal layers for the formation of semiconducting CuInSe₂ films", *Thin Solid Films* **vol. 357**, 179 (1999).

Rockett A., F. Abou-Elfotouh, D. Albin, M. Bode, J. Ermer, R. Klenk, T. Lommasson, T.W.F. Russell, R.D. Tomlinson, J. Tuttle, L. Stolt, T. Walter, and T.M. Peterson, "Structure and chemistry of CulnSe₂ for solar cell technology: current understanding and recommendations", *Thin Solid Films* **vol. 237**, 1 (1994).

Roedern B., "Advances in Phovoltaics at NREL", Denver, National Renewable Energy Laboratory report (1999).

Runyan W.R. and T.J. Shaffner, *Semiconductor measurements and instrumentation*, McGraw-Hill, New York, (1998).

Sánchez-Royo J.F., A. Segura, O. Lang, C. Pettenkofer, W. Jaegermann, A. Chevy, and L. Roa, "Photovoltaic properties of indium selenide thin films prepared by van der Waals epitaxy", *Thin Solid Films* **vol. 307**, 283 (1997).

Scheer R., T. Walter, H.W. Schock, M.L. Fearheiley, and H.J. Lewerenz, "CuInS₂ based thin films solar cell with 10.2% efficiency", *Appl. Phys. Lett.* **63**, 3294 (1993).

Scheer R. and H.J. Lewerenz, "Photoemission study of evaporated CuInS₂ thin films. I. Surface stoichiometry and phase segregation", *J. Vac. Sci. Technol. A* **12**, 51 (1994).

Scheer R. and H.J. Lewerenz, "Photoemission study of evaporated CuInSe₂ thin films. II. Electronic surface structure", *J. Vac. Sci. Technol. A* **12**, 56 (1994).

Scheer R., K. Diesner, and H.J. Lewerenz, "Experiments on the microstructure of evaporated CuInS₂ thin films", *Thin Solid Films* **268**, 130 (1995).

Scheer R. and H.J. Lewerenz, "Formation of secondary phases in evaporated CuInS₂ thin films: A surface analytical study", *J. Vac. Sci. Technol. A* **13**, 1924 (1995).

Schön J.H., Ch. Kloc, and E. Bucher, "Effect of the Ga-content on the defect properties of CuIn_{1-x}Ga_xSe₂ single crystals", *Thin Solid Films* **361-362**, 411 (2000).

Segura A., J.P. Guesdon, J.M. Besson, and A. Chevy, "Photoconductivity and photovoltaic effect in indium selenide", *J. Appl. Phys.* **62**, 876 (1983).

Srolovitz D.J., M.P. Anderson, G.S. Grest, and P.S. Sahni, "Grain growth in two dimensions", *Scripta Metallurgica* **17**, 241 (1983).

Stanberry B.J., C.H. Chang, S. Kim, S. Kincaid, G. Lippold, S.P. Ahrenkiel, S. Li, T.J. Anderson, and M.M. Al-Jassim, "Epitaxial growth of CuAu-ordered CuInSe₂ structural polytypes by migration enhanced epitaxy" *Mater. Res. Soc. Symp. Proc.* **583**, 195 (1999).

Stanberry B.J., S. Kincaid, S. Kim, C.H. Chang, S.P. Ahrenkiel, G. Lippold, H. Neumann, T.J. Anderson, and O.D. Crisalle, "Epitaxial growth and characterization of CuInSe₂ crystallographic polytypes", *J. Appl. Phys.* **91**, 3598 (2002).

Stolt L., J. Hedström, J. Kessler, M. Ruckh, K.O. Velthaus, and H.W. Schock, "ZnO/CdS/CuInSe₂ thin-film solar cells with improved performance", *Appl. Phys. Lett.* **62**, 597 (1993).

Thompson C.V. and H.I. Smith, "Surface-energy-driven grain growth in ultrathin (<100 nm) films of Si", *Appl. Phys. Lett.* **44**, 603 (1984).

Thompson C.V., "Secondary grain growth in thin films of semiconductors: Theoretical aspects", *J. Appl. Phys.* **58**, 763 (1985).

Thompson C.V., "Coarsening of particles on a planar substrate: interface energy anisotropy and application to grain growth in thin films", *Acta Metallurgica* **vol. 36**, 2929 (1988).

Touloukian Y.S., R.K. Kirby, R.E. Taylor, and P.D. Desai, "Thermal expansion: metallic elements and alloys", *Thermophysical properties of matter* **vol. 12**, 298 (1977).

Tuttle J.R., D.S. Albin, and R. Noufi, "Thoughts on the microstructure of polycrystalline thin film CuInSe_2 and its impact on material and device performance", *Solar Cells* **vol. 30**, 21 (1991).

Tuttle J.R., M. Contreras, M.H. Bode, D. Niles, D.S. Albin, R. Matson, A.M. Gabor, A. Tennant, A. Duda, and R. Noufi, "Structure, chemistry and growth mechanisms of photovoltaic quality thin-film $\text{Cu}(\text{In},\text{Ga})\text{Se}_2$ grown from a mixed-phase precursor", *J. Appl. Phys.* **vol. 77**, 153 (1995).

Wada T, N. Kohara, T. Negami, M. Nishitani, "Growth of CuInSe_2 crystals in Cu-rich Cu-In-Se thin films", *Journal of Materials Research* **vol. 12**, 1456 (1997).

Walter T., D. Braunger, H. Dittrich, Ch. Köble, R. Herberholz, and H.W. Schock, "Sequential processes for the deposition of polycrystalline $\text{Cu}(\text{In},\text{Ga})(\text{S},\text{Se})_2$ thin films: Growth mechanism and devices", *Solar Energy Materials and Solar Cells* **vol. 41-42**, 355 (1996).

Wong C.C., H.I. Smith, and C.V. Thompson, "Surface-energy-driven secondary grain growth in thin Au films", *Appl. Phys. Lett.* **vol. 48**, 335 (1986).

Yousfi E.B., T. Asikainen, V. Pietu, P. Cowache, M. Powalla, and D. Lincot, "Cadmium-free buffer layers deposited by atomic layer epitaxy for copper indium diselenide solar cells", *Thin Solid Films* **vol. 361-362**, 183 (2000).

Zeaiter K., Y. Llinares, and C. Llinares, "Structural and photoluminescence study of the quaternary alloys system $\text{CuIn}(\text{S}_x\text{Se}_{1-x})_2$ ", *Solar Energy Materials and Solar Cells* **vol. 61**, 313 (2000).

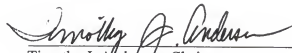
Zhang S.B. and S.-H. Wei, "Reconstruction and energetics of the polar (112) and (112) versus the non-polar (220) surfaces of CuInSe_2 ", NCPV program review meeting manuscripts, Lakewood, Colorado (2001).

Zhao J., A. Wang and M.A. Green, "19.8% efficient "honeycomb" textured multicrystalline and 24. 4% monocrystalline silicon solar cells", *Appl. Phys. Lett.* **vol. 73**, 1991 (1998).

BIOGRAPHICAL SKETCH

Suku Kim was born in Jinhae, South Korea on July 30, 1970. He received his B.S. degree in chemical engineering from Pohang University of Science and Technology in 1993. He attended Seoul National University and graduated with his M.S. degree in chemical engineering in 1995. He entered a Ph.D. program in chemical engineering at the University of Florida in 1996. He joined Dr. Anderson's research group as a graduate research assistant in the same year. His research topics during Ph.D. study are semiconductor process and CuInSe₂-based compound photovoltaics. He has acquired broad knowledge and research experiences on semiconductor materials and processings during his study. His dissertation encompasses the fields of chemical engineering, electrical engineering, and material science.

I certify that I have read this study and that in my opinion it conforms to acceptable standards of scholarly presentation and is fully adequate, in scope and quality, as a dissertation for the degree of Doctor of Philosophy.



Timothy J. Anderson, Chairman
Professor of Chemical Engineering

I certify that I have read this study and that in my opinion it conforms to acceptable standards of scholarly presentation and is fully adequate, in scope and quality, as a dissertation for the degree of Doctor of Philosophy.



Oscar D. Crisalle
Associate Professor of
Chemical Engineering

I certify that I have read this study and that in my opinion it conforms to acceptable standards of scholarly presentation and is fully adequate, in scope and quality, as a dissertation for the degree of Doctor of Philosophy.



Sheng S. Li
Professor of Electrical and
Computer Engineering

I certify that I have read this study and that in my opinion it conforms to acceptable standards of scholarly presentation and is fully adequate, in scope and quality, as a dissertation for the degree of Doctor of Philosophy.



Paul H. Holloway
Distinguished Professor of Materials
Science and Engineering

I certify that I have read this study and that in my opinion it conforms to acceptable standards of scholarly presentation and is fully adequate, in scope and quality, as a dissertation for the degree of Doctor of Philosophy.

Fan Ren
Fan Ren
Professor of Chemical Engineering

This dissertation was submitted to the Graduate Faculty of the College of Engineering and to the Graduate School and was accepted as partial fulfillment of the requirements for the degree of Doctor of Philosophy.

May 2003

Pramod Khargonekar
Pramod P. Khargonekar
Dean, College of Engineering

Winfred M. Philips
Dean, Graduate School



, K494